UNDERSTANDING THE EFFECT OF INTERFACE CHEMISTRY IN BIOMINERALIZATION – DEVELOPMENT OF AN *IN VITRO* MODEL FOR CALCIUM PHOSPHATE MINERALIZATION

A Dissertation

Presented to the Faculty of the Graduate School

of Cornell University

In Partial Fulfillment of the Requirements for the Degree of

Doctor of Philosophy

by

Amy Marie Blakeley

January 2013

UNDERSTANDING THE EFFECT OF INTERFACE CHEMISTRY IN BIOMINERALIZATION – DEVELOPMENT OF AN *IN VITRO* MODEL FOR CALCIUM PHOSPHATE MINERALIZATION

Amy Marie Blakeley, Ph.D.
Cornell University 2013

Structure-function relationships in mineralized tissues, such as bone and teeth, depend upon the chemical interactions of the interfaces between cells, proteins, organic matrix, and mineral (calcium phosphate). Development of *in vitro* models that more accurately model mineralization systems *in vivo* will assist in understanding medical conditions as well as inform biomimetic materials development.

Understanding the heirachical structures in mineralized tissues relies on the chemical control of crystal nucleation and growth at the interfaces. Studies presented in this thesis provide additional *in vitro* tools for studying *in vivo* systems by controlling for interface chemistry, mineralization environment, and experimental setup for elucidating the effect of interfaces in biomineralization. Covalently bound surface chemistry – oxide, methyl, carboxylate, 2-aminoethyl dihydrogen phosphate, osteopontin, and bovine

serum albumin (BSA) - on porous silicon substrates has a distinct affect on surface mineral nucleation and morphology. The morphology and coverage resulting from suspending the differed from those reported in literature. This method has potential for selectively examining the effects of covalently bound protein conformations and segments, more closely mimicking the conformation constraints at interfaces in biological systems.

Hydrogel-based double diffusion system (DDS) has the potential to allow for the simultaneous *in vitro* study of cell-mineral-matrix interactions in a 3-D environment, the 'holy-grail' of mineralization studies. Successful hydroxyapatite mineralization was demonstrated at both room temperature and incubator conditions using a custom build polycarbonate DDS with polydimethylsiloxane membranes for gas permeability, minimal polyethyleneimine coating for gel adhesion, and cell culture compatible Agarose. This system provides researchers with a new tool for combining cell, mineral, and matrix in a 3-D environment for understanding the complexity of cell-mineral-matrix interactions.

Understanding how proteins interact with surface chemistry as well as their structural changes and coverage, provides important clues towards biology's ability to exert control over biomineralization. Analysis of the monolayer-protein interface via infrared spectroscopy demonstrated that the

protein conformation increases in disorder upon adsorption to the surface based on amide peak positions and amounts of adsorbed protein varied as a function of chemistry. Work in this thesis provides tools and information towards developing *in vitro* systems that elucidate complex interactions in mineralized tissues.

BIOGRAPHICAL SKETCH

Amy Marie Richter Blakeley was born in 1982 to Karen and Randy Richter in Minot, ND. She grew up the daughter of a diesel mechanic playing in the shop and on the farm as well as exploring her mother's science classrooms. This love of exploring sparked her interest in science, whether it be looking at the specimen jars in the classroom, helping set up classroom labs, playing in the grain fields, or exploring the shores of the local lake.

Amy's collegiate endeavors started after graduating from Rugby High School in 2000. She attended North Dakota State University (NDSU) where she majored in Chemistry with a polymers and coatings option. Amy started scientific research her first semester at NDSU under the supervision of Dr. Dennis Tallman. It was here, working on the electroless deposition of polymers on aluminum alloys for corrosion protection, that she found her enjoyment for solving scientific questions in the lab. During her time at NDSU, she was a Goldwater scholar, participated in many extracurricular activities, and participated in an REU at Cornell University.

In the fall of 2004, Amy started graduate school in the Cornell Chemistry department working on MEM's devices and silicon surface chemistry with Melissa Hines. After finishing her master's in the Hines group, Amy decided to change research focus and joined Lara Estroff's

group during the fall of 2008. Here, she studied bio-inspired materials, specifically hydroxyapatite similar to the mineral component found in bone and teeth. She used her knowledge of silicon surface chemistry and machining experimental set ups to develop *in vitro* models for HA formation as well as study interfaces in mineralization. Amy will be joining Sappi Fine Paper NA's research and development team in Westbrook, ME as a Research Scientist in January 2013.

To my family and friends: Your love and support has made this journey possible.

ACKNOWLEDGMENTS

My journey towards finishing my PhD would not have been possible without the help of many people both professionally and personally.

First and foremost, I would like to thank Professor Lara Estroff for mentoring me. She took me on as a student who was changing groups well into their PhD and allowed me to rebuild my confidence and skills as a scientist. She reminded me how collaborative research can be while also connecting me with a wonderful group of colleagues and collaborators.

I am deeply appreciative of my labmates who have pushed me to grow not only as a scientist but also as a person. The Hines group 'crew' of Ian Clark, Debodhonyaa Sengupta, Ankush Gupta, Marc Faggin, and Brandon Aldinger, your support, simulating conversations, and laughter in the basement of Baker Lab will be some of my foundest graduate school memories. Ellen Keen of the Estroff lab for collaborating on the silk fibroin GAFTIR work, writing a paper, and many lunch conversations. Miki Kunitake for sharing an office and listening to my experimental mutterings as well as sharing my coffee addiction. Jason Dorvee for discussions regarding the DDS and surface chemistry. Debra Lin for her help with the biological and cell culture applications. Ruiqi Song, Hiroaki Sai, and Hanying Li for our overlapped time together. Undergraduates in the Estroff Lab,

Elaine Higashi and Allison Fleck, for their contributions to my work.

My work would not have been possible without the facility managers at CCMR who spent countless hours helping me learn more about materials characterization. Specifically, Mick Thomas on the FE-SEM and Maura Weathers on x-ray diffraction tools. Campus machine shops and machinists were also essential to my work – Nate Ellis in the LASSP machine shop, Paul Bishop in the Bard Machine shop, and Glen Swan in the Chemical Engineering machine shop.

Much of my surfaces work was made possible via collaboration with Professor Adele Boskey. Adele was always willing to share her knowledge and resources making the surfaces work possible. And thanks to my committee members Professors Christopher Ober and Bruce van Dover.

Last but not least, I would like to thank my family and friends. My friends made adventures outside of the lab more enjoyable, whether it be kayaking or debating campus governance. Brenda Wickes and Ellen Gainer for encouraging me to continue in graduate school. My parents and brother have been there for me through all the trials and tribulations of higher education. My son, Drew, for waiting to arrive into this world until I defended. And my husband, Daniel, for being a calming influence and always supporting me in this adventure.

TABLE OF CONTENTS

LIST OF FIGURES

LIST OF TABLES

LIST OF SCHEMES

LIST OF EQUATIONS

LIST OF ABBREVIATIONS

$-CH_3$	Methyl terminated monolayer
-COOH	Carboxylate terminated monolayer
$-NH_2$	Amine terminated monolayer
-OH	Alcohol terminated monolayer
$-PO_4H_2$	Phosphate terminated monolayer
AA	Amino acid
ACP	Amorphous calcium phosphate
ACS	American Chemical Society
ADP	2-aminoethyl dihydrogen phosphate
AFM	Atomic force microscopy
ATR	Attenuated total reflection spectroscopy
BBS	Borax buffered solution
BSA	Bovine Serum Albumin
c	Concentration
Ca	Calcium
$CaCO_3$	Calcium carbonate
CD	Circular dichroism
cDDS	Combination double diffusion system

CNF	Cornell NanoScale Science and Technology Facility
D	Diffusivity
DCPD	Brushite or dicalcium phosphate
DDS	Double diffusion system
DI water	Deionized water
ECM	Extra-cellular matrix
EDC	1-ethyl-3-[3-dimethylaminopropyl]carbodimide hydrochloride
EDX or EDS	Energy-dispersive x-ray spectroscopy
FE-SEM	Field Emission Scanning Electron Microscopy
FTIR	Fourier transform infrared spectroscopy
GAFTIR	Grazing angle Fourier transform infrared spectroscopy
GeATR	Germanium attenuated total reflection spectroscopy
HA or HAP	Hydroxyapatite
HF	Hydrofluoric acid
I.D.	Inner diameter
IAP	Ion activity product
ICP-AES	Inductively coupled plasma - atomic emission spectroscopy
iDDS	Incubator double diffusion system

IL-8	Interleukin 8
IMD	1-(3-aminopropyl)Imidazole
IR	Infrared spectroscopy
Ksp	Solubility product
mDDS	Mini-double diffusion system
n16N	30 AA N-terminal domain of n16
NaOH	Sodium hydroxide
NCPs	noncollagenous proteins
NHS	N-hydroxysuccinimide
NPT	National pipe thread
O.D.	Outer diameter
OCP	Octacalcium Phosphate
OPN	Osteopontin
OSCC-3	Oral squamous cell carcinoma
PBS	Phosphate buffered saline
pDDS	Polycarbonate Double Diffusion System
PDL	Periodontal Ligament
PDMS	Polydimethylsiloxane
PEG	Polyethylene glycol
PEI	Polyethyleneimine

Pi	Phosphate
PLG	Poly(lactide-co-glycolide)
pSi	Porous Silicon
PVD	Physical vapor deposition
pXRD	Powder x-ray diffraction
QCM	Quartz crystal microbalance
R-$SiCl_3$	Silanes
S	Solution supersaturation
SAED	Selected area electron diffraction
SAMs	Self assembled monolayers
SBF	Simulated body fluid
SEM	Scanning Electron Microscopy
SPR	Surface plasmon resonance spectroscopy
STR	Single tube twin reservoir system
T	Titrant concentration
TCP	Tricalcium phosphate
TEM	Transmission Electron Microscopy
Tyr	Tyrosine
v	Number of ions in the mineral formula unit
W	Reaction concentration

x	Distance
XPS	X-ray photoelectron spectroscopy
XRD	X-ray diffraction
β-TCP	β-tricalcium phosphate

Chapter 1:

SURFACES FOR DIRECTING CACLIUM PHOSPHATE MINERALIZATION

1.1 INTRODUCTION

Nature utilizes millions of years of experience to tailor the intricate structures of mineralized tissues such as bone, teeth, and mollusk shells to fit their function and environment. The most common inorganic components in mineralized tissues are calcium carbonate in mollusk shells and calcium phosphate in bone and teeth. The nucleation and growth of the biominerals are under tight regulation.[1] For example, tooth enamel has a defined, nucleating surface at which crystal growth is initiated within a gel-like matrix.[2] The heirachical levels of the tooth contain a multitude of interfaces. The interfaces between the smaller components in the hierarchy affect the overall properties and function of the mineralized tissue. The structure-function relationships in bone and teeth depend upon the chemical interactions at the interfaces between cells, proteins, organic matrix, and mineral (calcium phosphate). An understanding of the heirachical structures present in each system guides the development of *in vitro* models probing the component interfaces. Understanding the chemical control of crystal nucleation and growth at the interfaces of cell-mineral-proteins-matrix will help guide researchers and clinicians in developing materials for repair of mineralized tissues.

Bone is a dynamic composite structure that provides a rigid framework for the

body composed of approximately 70% mineral (carbonated hydroxyapatite) and 30% organic matrix (collagen and non-collagenous proteins) by dry weight.[3,4] Cells (osteoblasts and osteoclasts) within the body are constantly working to repair and regenerate the bone structure in response to the applied stresses on the bone framework. Weiner and Wagner proposed seven heirachical levels in the structure of bone (Figure 1.1).[5] Starting from the most basic components of the individual calcium phosphate crystals and collagen fibrils of level 1, each level of bone structure increases in complexity until reaching the full bone assembly of level 7. The images demonstrate a large number of interfaces with complex chemical interactions and structural assemblies.

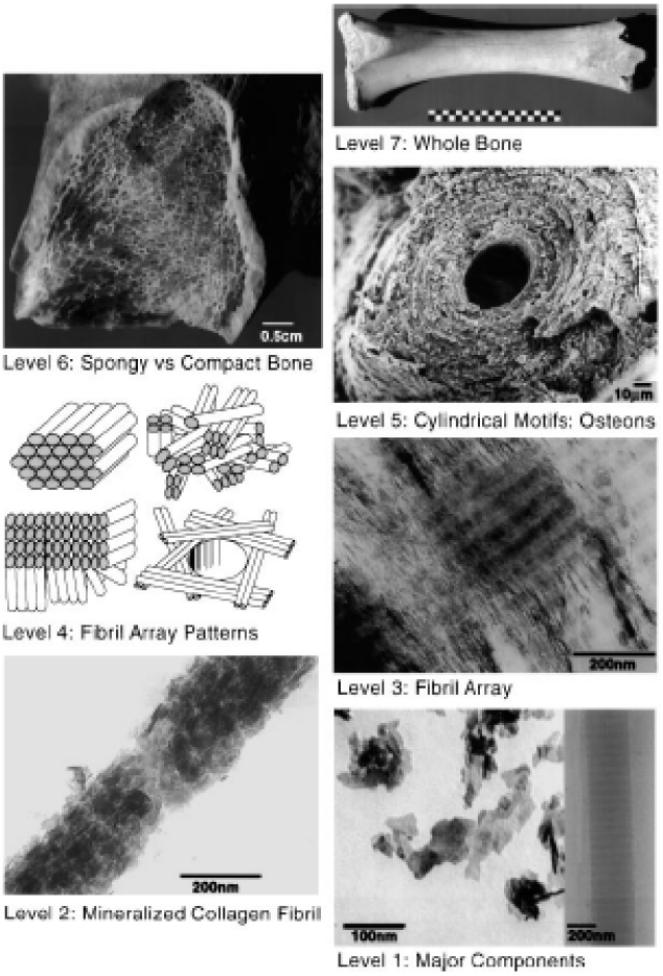

Figure 1.1: Seven levels of bone structure.[5] Level 1: Isolated crystals from human bone (left) and unmineralized and unstained collagen fibril from turkey tendon (right) in vitreous ice TEM. Level 2: TEM images of mineralized collagen from turkey tendon. Level 3: TEM of mineralized turkey tendon. Level 4: Four fibril array patterns found in bone. Level 5: SEM of a single human bone osteon. Level 6: Cross-sectional image of fractured, fossilized human femur. Level 7: Whole bovine bone.

Teeth demonstrate a similar complexity to bone. Not only are there a multitude of interfaces within the tooth structure but there is also a unique organization of carbonated hydroxyapatite crystals within the outer layer (enamel) of the tooth that results in a hard, abrasion resistant material (Figure 1.2).[2,6] Each level of the enamel

(bulk, meso, micro, and nano) exhibits a complex assembly of hydroxyapatite within an organic matrix. Enamel is also the most 'mineralized' tissue in the mammalian body comprised of 95-97% by weight hydroxyapatite.

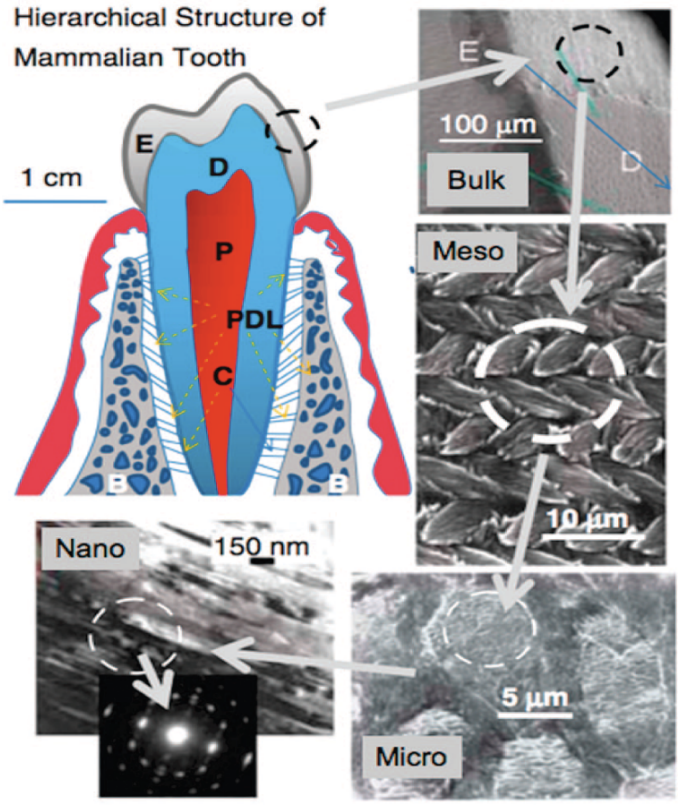

Figure 1.2: Structure of mammalian tooth and enamel. Enamel (E) is the outer layer of the tooth above the dentin (D) while the pulp (P) contains nerves and blood vessels. The cementum (C) is the outer layer of mineralized tissue surrounding the root of the tooth that is anchored to jawbone via the periodontal ligament (PDL). The cut out images depict the heirachical structure of the enamel. Bulk: The structure across the dentin-enamel junction. Meso: Prismatic enamel comprised of weaving rods of mineral. Micro: Single rod composition. Nano: Organized array of HA crystals aligned along the c-axis.[2,7]

Effective study of mineralization in bone and teeth requires development of *in vitro* models/tools to be able to study the interactions of mineral-matrix-cell-protein at the interfaces. This requires understanding of the phases and morphology of calcium phosphate minerals, synthetic methods used to produce calcium phosphate, and chemically tunable surfaces.

1.2 PHASES OF CALCIUM PHOPSHATE AND MORPHOLOGIES

The main mineral component of bone and teeth is hydroxyapatite (HA or HAP; $Ca_{10}(PO_4)_6(OH)_2$). The biological form of HA is most commonly found as carbonated hydroxyapatite where a small percentage of the OH^- and/or PO_4^{-3} groups have been substituted by carbonate groups (CO_3^{2-}). The general structure of hydroxyapatite is hexagonal with a P63/m space group, which refers to a space group with six-fold symmetric axis with a threefold helix (Figure 1.3).[8-10] In order to understand the formation of hydroxyapatite in a biological system, the possible synthetic phases of calcium orthophosphates in *in vitro* systems must be considered as well as the morphologies.

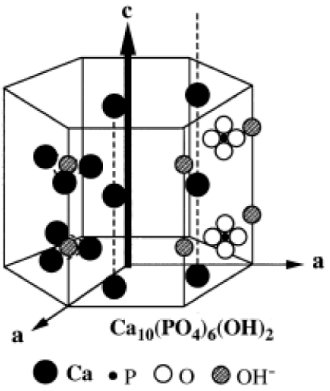

Figure 1.3: Crystal structure of hydroxyapatite with the hexagonal orientation outlined and dashed lines emphasizing the Ca channel structure.[9]

The most relevant of phases to consider when studying hydroxyapatite are brushite or dicalcium phosphate (DCPD), octacalcium phosphate (OCP), and amorphous calcium phosphate (ACP), each with distinct properties, synthetic conditions, and morphologies.[4] OCP, DCPD, and ACP have all been proposed as possible precursors to HA formation in biology.[11] ACP typically forms spherical particles,[12] HA forms needle and/or rosette-like crystals,[13] and OCP tends to form plates or ribbons.[14]

One of the most challenging aspects of synthesizing calcium orthophosphates are their relatively poor solubilites and sensitivity to solution conditions (Figure 1.4 and Table 1.1).[11,15] The solubility isotherms of calcium phosphates demonstrate the complexity of the synthetic conditions at physiological pH 7.4. Small changes in the pH, concentration of calcium and phosphate ions in solution, or ionic strength affect

the phase of the synthetic calcium phosphate.

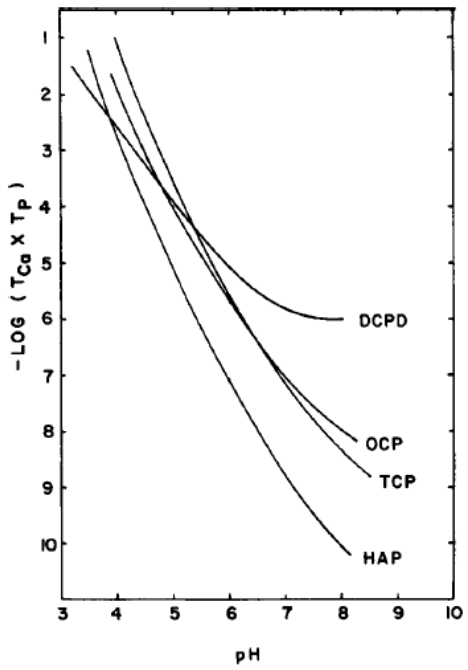

Figure 1.4: Solubility isotherms at 37° C and 0.1 M ionic strength of dicalcium phosphate (DCPD), octacalcium phosphate (OCP), tricalcium phosphate (TCP), and hydroxyapatite (HAP).[16]

Table 1.1: Ca/P molar ratios, general chemical formula, and solubility product of common phases of calcium phosphates.[8,11]

Ca/P ratio	Phase	Formula	Solubility Product (37˚C)
1.00	Brushite (DCPD)	$CaHPO_4{\cdot}2H_2O$	1.87×10^{-7} M^2
1.33	octacalcium phosphate (OCP)	$Ca_8H_2(PO_4)_6{\cdot}5H_2O$	2.5×10^{-99} M[16]
1.20-2.20	amorphous calcium phosphate (ACP)	$Ca_xH_y(PO4)_z{\cdot}nH_2O$, n= 3-4.5	*a*
1.50	β-tricalcium phosphate (β-TCP)	$\beta\text{-}Ca_3(PO_4)_2$	2.5×10^{-30} M^5
1.67	hydroxyapatite (HA or HAP)	$Ca_{10}(PO_4)_6(OH)_2$	5.52×10^{-118} M[18]

[a] The solubility product cannot be accurately measured.

X-ray diffraction and infrared spectroscopy are used to distinguish between the phases of calcium phosphate experimentally. ACP does not have a distinct x-ray

pattern due to its amorphous nature. OCP, DCPD, and HA have similar diffraction patterns with the exception of distinct peaks for OCP at 4.7° 2θ and DCPD at 11.6 2θ. HA is most often distinguished by diffractions at ~26° 2θ, a triplet around 31° 2θ, and the lack of the OCP and DCPD peaks.[12,17] Infrared spectroscopy (IR) also provides a useful way to distinguish calcium phosphate phases, especially between ACP and HA, via vibrational differences in the 500-1500 cm^{-1} region (Table 1.2). The Raman spectroscopy signatures are not as distinct. However, an extensive study by Wuthier et. al has quantified the synthetic and biological calcium phosphate Raman spectra.[18]

Table 1.2: Phase distinguishing infrared spectroscopy peaks and modes.[19-23]

Phase	Distinct Peak positions (cm^{-1})	Peak Character/mode	Ref
Brushite (DCPD)[a]	-	-	21
octacalcium phosphate (OCP)	865, 910	P-(OH) stretching mode of the HPO42- group	19
amorphous calcium phosphate (ACP)	550-600; 900-1200	broad P-O antisymetric bending mode; broad P-O symmetric and anti-symmetric stretching	20,22
hydroxyapatite (HA or HAP)	564 and 574; 962, 1020, 1060 and 1110	P-O antisymetric bending mode splitting; P-O symmetric and anti-symmetric stretching	23

[a] Complex set of vibrations. See Ref 21 for representative spectra.

Solution supersaturation ratio (S; Eqn 1.1) plays an important role in solution based mineral precipitation. IAP is the ion activity product, K_{sp} is the solubility product, and v is the number of ions in the mineral formula unit. S for hydroxyapatite is given by Eqn 1.2

$$S = \left(\frac{IAP}{K_{sp}}\right)^{\frac{1}{\nu}} \qquad \text{(Eqn 1.1)}$$

$$S = \left(\frac{[a(Ca^{2+})]^{10}[a(PO_4^{3-})]^6[a(OH^-)]^2}{K_{sp}}\right) \qquad \text{(Eqn 1.2)}$$

For hydroxyapatite, K_{sp} is 5.52 x 10^{-118} (Table 1.1). S values determine the precipitation of mineral from solution with S < 1 resulting in undersaturation, S = 1 in equilibrium, and S > 1 resulting in precipitation. Given hydroxyapatite's relative insolubility, minimal concentrations of calcium and phosphate (i.e. approximately < 2.0 mM depending upon solution ionic strength) are needed before solution precipitation. Principles of supersaturation and phase control are both important for solution based mineralization systems.

1.3 SYNTHETIC METHODS FOR CALCIUM PHOSPHATE

Solution-based mineralization is the primary synthesis method used for *in vitro* studies of hydroxyapatite formation on surfaces. While solid-state and sol-gel methods[24] can be used to synthesize calcium phosphate phases, they are not practical for the application of studying the effect of surface chemistry on HA formation. Three synthetic methods – aqueous solution mixing and heating, simulated body fluid (SBF), and constant composition – will be discussed.

1.3.1 Aqueous Solution Mixing and Heating

Aqueous solution mixing is one of the most common methods of synthesizing

calcium phosphate mineral. As shown by Figure 1.4 (solubility isotherm), the pH as well as ion concentrations are important for obtaining the targeted mineral phase. For the purpose of this discussion, HA will be the targeted mineral phase. Generally, this method involves mixing solutions of calcium and phosphate salts in a ratio similar to the targeted phase (5:3 calcium to phosphate ratio for HA) at a pH favorable for the phase formation (pH > 9 for HA).[25,26] Buffer solutions or a pH stat system are used to maintain the reaction pH. HA can be synthesized at pH 7.4, however, detailed analysis should be utilized to confirm that the phase is HA not OCP, which preferentially forms under acidic conditions. Following a period of particle 'maturation' in solution, the calcium phosphate particles are filtered and then dried at room temperature, vacuum, or mild heat (100˚C) resulting in a poorly crystalline HA. The temperature during the maturation phase as well as the pH have been shown to be crucial to phase formation and mineral Ca/P ratio.[25] The crystallinity of the final HA product can be increased by calcining the particles typically between 1000 - 1300˚C.[25,27,28,29]

The crystallinity and aspect ratio of the resulting particles can also be affected by using hydrothermal reaction methods. Hydrothermal reactions involve suspending calcium phosphate particles suspended in aqueous solution under heating (< 350˚C) in a Parr® bomb.[30-32] The resulting particles typically have needle-like morphology and are highly crystalline without using the high temperatures of calcination.

1.3.2 Simulated Body Fluid (SBF)

Simulated body fluid (SBF) contains ion concentrations that closely mimic the concentrations found in blood plasma (Table 1.3).[33,34] Many researchers using surfaces *in vitro*, utilized SBF solutions for formation of hydroxyapatite.[33,35-42] SBF solutions are typically buffered to a physiological pH between 7.2 and 7.6 using 0.1 M Tris buffer and maintained at 0.15 M ionic strength. While solutions of SBF are easily prepared using sodium and chloride salts, the number of counter ions as well as buffer complicate the analysis of chemistry and surface effects on morphology/phase of calcium phosphate. Exact solution concentrations are difficult to analyze as precipitation occurs and experiments are typically run in excess of 7 days, many times as long as 30 days. Anytime solution is removed to analyze solution composition via atomic adsorption or inductively coupled plasma, the disruption to the solution could potentially cause early precipitation.

Table 1.3: Representative Simulated Body Fluid (SBF) Formula.[34]

Ions[a]	Concentration, mM
Na^+	142.0
Cl^+	148.0
K^+	6.5
Mg^{2+}	1.5
HCO_3^-	4.2
Ca^{2+}	2.5
HPO_4^{2-}	1.0
SO_4^{2-}	1.0

[a]Solutions are typically buffered with 0.1 M Tris buffer.

1.3.3 Constant Composition and pH Static

The constant composition and pH static methods pioneered by Nancollas and coworkers allow researchers to study mineral formation while actively controlling the temperature, atmosphere, and solutions compositions while monitoring pH and calcium concentrations.[11,15,43-50] Both pH and calcium concentrations have been utilized for controlling mineral formation. Application of this system has been studied for calcium phosphate,[11,15,43-45] calcium oxalate,[46,47] and calcium carbonate[48] crystal growth. In order to determine the titrant concentrations in the reaction, the mass balance equations for the targeted mineral must be completed. Equations 1.3 – 1.8 are the result of mass balance calculations for HA formation.[43] This set of calculations can also be done for octacalcium phosphate (Eqns 1.9 – 1.13) to target OCP formation rather than HA.[44]

Hydroxyapatite Mass Balance Equations

$$T_{CaCl_2} = 2W_{CaCl_2} + 5C_{eff} \quad \text{(Eqn. 1.3)}$$

$$T_{NaCl} = 2W_{NaCl} - 10C_{eff} \quad \text{(Eqn. 1.4)}$$

$$T_{NaH_2PO_4} = 2W_{NaH_2PO_4} + 3C_{eff} \quad \text{(Eqn. 1.5)}$$

$$T_{NaOH} = 2W_{NaOH} + 7C_{eff} \quad \text{(Eqn.1.6)}$$

$$C_{eff} = {}^{W_{CaCl_2}}/_{10} \quad \text{(Eqn. 1.7)}$$

$$W_{NaOH} = W_{NaH_2PO_4} - C_{eff} \quad \text{(Eqn. 1.8)}$$

Octaclacium Phosphate Mass Balance Equations

$$T_{CaCl_2} = 2W_{CaCl_2} + 4C_{eff} \quad \text{(Eqn. 1.9)}$$

$$T_{NaCl} = 2W_{NaCl} - 8C_{eff} \quad \text{(Eqn. 1.10)}$$

$$T_{NaH_2PO_4} = 2W_{NaH_2PO_4} - 3C_{eff} \quad \text{(Eqn. 1.11)}$$

$$T_{NaOH} = 2W_{NaOH} - 5C_{eff} \quad \text{(Eqn.1.12)}$$

$$C_{eff} = {}^{W_{CaCl_2}}/_{8} \quad \text{(Eqn. 1.13)}$$

Changes in calcium concentrations determine the titrant addition for the constant composition system while a pH Stat system uses changes in pH. The complex set of titrant addition, solution composition, and monitoring require substantial equipment needs – automated titrators, a calcium electrode, a reference electrode, a pH electrode, and a sealed reaction vessel. This method also allows for the monitoring of the kinetics (time, titrant volumes, pH changes) of mineral formation while also directing the phase (solution composition and mass balance equations).

1.4 SURFACES FOR DIRECTING THE NUCLEATION OF CALCIUM PHOSPHATES

One way of directing the growth of poorly soluble salts, such as hydroxyapatite (HA), is to provide a substrate that reduces the interface energy and promotes nucleation. Rigid, chemically modifiable surfaces provide an ideal substrate for

investigating calcium phosphate mineralization. Three main metal substrates have been used for calcium phosphate mineralization studies – silicon/silicon dioxide, titanium, and gold – each with specific advantages and applications. More flexible polymer substrates have also been used for HA mineralization studies, but will not be covered here.[51-54]

Experimental geometry considerations are also important in the study of calcium phosphate mineralization on surfaces. Substrates placed at the bottom of a vessel in solution-based mineralization experiments are potentially susceptible to mineral forming in solution depositing on the substrate, or 'gravitational' mineralization. Suspension of substrates upside down in solution ensures that observed mineral formation is only observed at the substrate interface. For the purpose of this text, these two geometries will be referred to as gravitational and suspended geometries, respectively.

1.4.1 Silicon

Silicon serves as an ideal 'nucleating' substrate for mineralization because it can be selectively functionalized, patterned via nanofabrication techniques, and used as a flat or porous substrate. Extensively used in the semiconductor industry, a significant body of literature exists regarding chemical modification,[55-67] as well as the preparation of porous substrates[68] for biological applications.[55,69] Silicon monolayer chemistry has also been shown to protect the surface from chemically demanding environments,[62,64,65,70] such as acidic, basic, ionic, and high temperature conditions,

making silicon surfaces ideal for biological applications. Silicon substrates and oxides have also been shown to be biocompatible within cellular systems degrading into non-toxic silicic acid.[71-74]

1.4.1.1 Surface Functionalization Methods

Silicon surface chemistry allows for covalent attachment of chemically tailored monolayers to the surface. The general routes for achieving this chemistry can be grouped into the following general categories based on Si-O and Si-H chemistry: oxidation,[57] silane-based,[57-60] hydrosilylation,[56,61,62,65] and Grignard[63,64] (Figure 1.5). Si-Si and electrochemical routes[55] are also possible but are not reviewed in this text. Understanding of the general chemical routes to surface functionalization and packing provides a platform for selectively introducing surface chemistry into mineralization systems.

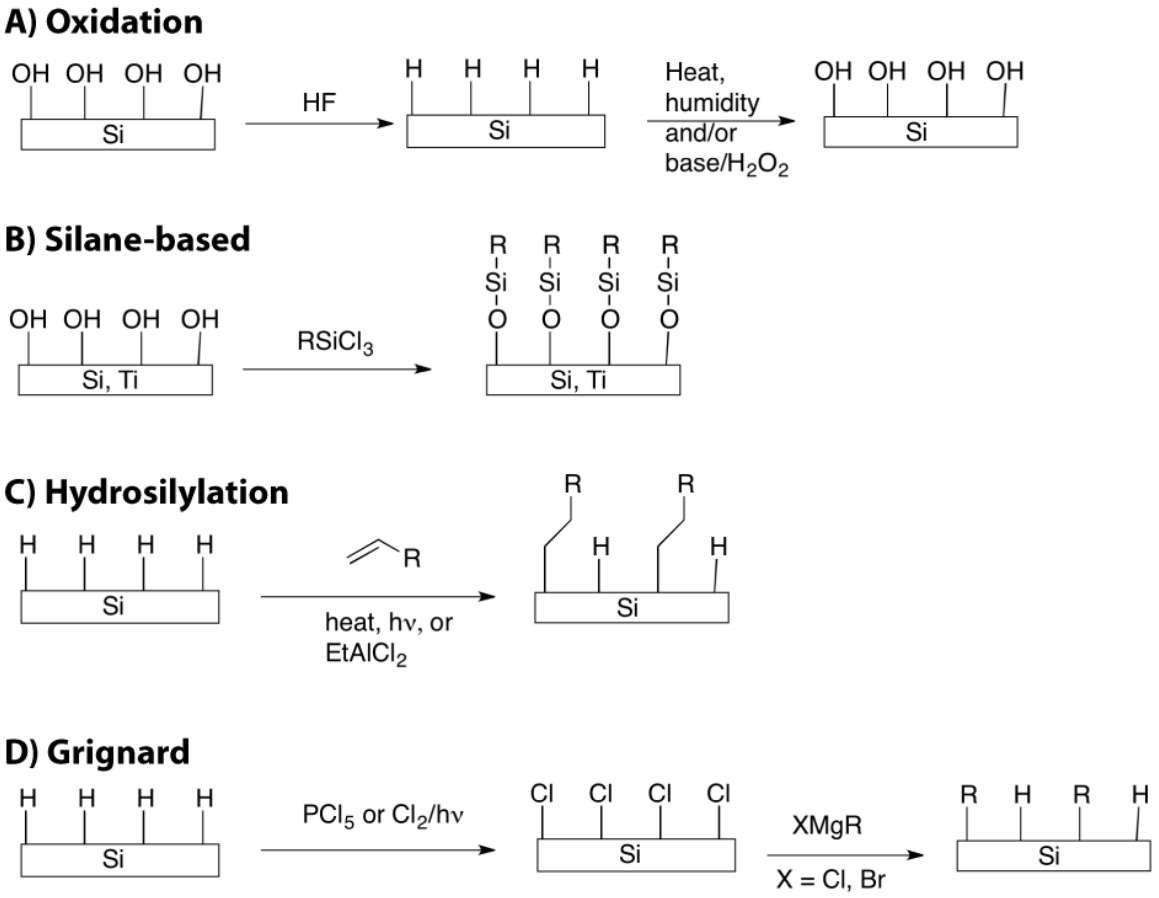

Figure 1.5: General routes to functionalization of silicon surfaces: A) Oxidation chemistry via heating or chemical means[57] B) Silane-based chemistry[57-60] C) Hydrosilylation using heating, light, or Lewis Acids[56,61,62,65] D) Grignard reaction via surface halogenation.[59,60]

Oxidation of the silicon surface will happen naturally with a native oxide layer (~13 Å) formed over time in atmosphere. For experimental applications, it is typically desirable to have a thicker, more consistent oxide formed over a shorter time period (hours vs. days or weeks). Chemical oxidation is typically achieved by removing the native oxide layer from a silicon sample using hydrofluoric acid to achieve a hydrogen terminated silicon surface.[57] The freshly hydrogen terminated surface is then placed in

a thermal and/or humid environment (Figure 1.5A). To achieve an oxide surface via wet chemical techniques, surfaces are typically placed in a solution of NH_4OH/H_2O_2 at 70˚C for approximately 20-30 minutes. A variety of thermal techniques are available ranging from heating at temperatures from 200-1100˚C under atmospheric or oxygen-rich conditions to furnaces that introduces gases at high temperatures.[57] Oxidation of the silicon surface is a typical way to passivate or protect the underlying substrate, as well as a platform for silane-based chemistries.

Silane-based functionalization utilizes silane chemistry to attach monolayers to a silicon dioxide surface, typically a silicon substrate with a thin oxide layer or a glass slide (Figure 1.5B).[57-59] This chemistry reacts a trichlorosilane with the oxide surface, resulting in a monolayer of R groups on the substrate surface attached via a Si-O-Si bond. While this chemistry appears straightforward, it is susceptible to the cleavage of the Si-O bond under acidic or basic conditions.[75,76] The introduction of the oxide layer can also introduce defects and roughness that may not be desirable for some applications.[77-79]

Hydrosilylation chemistry is the most robust way to add chemistry to a silicon surface, which uses heat, light, or a Lewis acid to covalently attach a primary alkene to the silicon surface (Figure 1.5C).[56,61,62,65] The alkene reacts with the Si-H bonds on the surface to create a Si-C linkage. The R group of the primary alkene has to be chosen carefully so as not to preferentially react with the Si-H bonds over the alkene. This chemical route allows for the introduction of a carboxylic acid terminated monolayer,

opening up a variety of routes for attachment of complex molecules. The most biologically relevant route is the ability to use amine coupling chemistry to attach primary amines (R-NH_2) via an amide bond with the carboxylic acid functional group. This reaction allows for the attachment of proteins, various amino acids, and other compounds containing NH_2 groups.[67]

Grignard-based surface chemistry compliments the capabilities of the hydrosilylation reaction. Grignard chemistry uses PCl_5 or chlorine gas to halogenate a freshly hydrogen terminated silicon surface under air and water free conditions (Figure 1.5D).[59,60] The halogenated surface is then reacted with a Grignard reagent (XMgR; X = Cl, Br) under reflux. Two interesting chemistries not achievable via hydrosilylation routes are available with this reaction method– methyl termination and terminal alkene. Having a terminal alkene opens a variety of catalyst and synthetic routes for functionalizing the silicon surface, for example, the covalent attachment of polymer overlayers using a Grubbs catalyst and ring-opening metathesis polymerization.[66]

The packing of molecules on the surface also plays an important role in directing surface mineralization (i.e., the spacing of the functional groups can affect the aggregation of ions and the nucleation of crystallites). Theoretical studies have shown that alkyl monolayers, such as those formed via hydrosilylation or Grignard reaction routes, can at best terminate 50% of the surface Si-H bonds on a silicon (111) surface due to steric hinderances.[80] This percentage decreases as the size of the

terminal R group increases. The silane-based monolayers have an inherently disordered surface chemistry as a result of the roughness of the underlying, amorphous oxide surface.[79,81]

1.4.1.2 Silicon Surface Mineralization

Although silicon surfaces have robust, tunable surface chemistry, they have rarely been used to study calcium phosphate mineralization. The studies that have been done on silicon surfaces use predominately porous silicon (pSi) substrates[36,68,82-85] and are all in simulated body fluid (SBF) with the exception Sommerdijk and co-workers who used Tris-buffered solutions. For the purposes of this discussion, the applications of silicon surfaces to calcium phosphate mineralization will be divided into pSi,[36,64,74-77] silane,[35] and bulk/polysilicon.[86-90]

pSi studies of calcium phosphate mineralization all used oxide surface chemistry and SBF as the mineralization solution.[36,64,74-77] The pSi studies tend to focus on the formation and/or rate of formation of hydroxyapatite on a surface for biomimetic applications, rather than the effect of the surface in addition to selective chemistry. Experiments were carried out over the time frame of hours to 6 weeks with the samples placed at the bottom of the reaction vessel. One of the earliest and most distinctive examples of calcium phosphate mineralization on pSi is work of L.T. Canham.[36] In this study, oxidized (i.e., 'aged') and freshly prepared pSi substrates were placed in SBF. The freshly prepared pSi substrates showed substantial

degradation in the SBF while the passivated pSi prevented degradation. Mineralization on the pSi and adjacent bulk silicon was observed within 7 days (Figure 1.6). Observed mineral morphology is consistent with that of gravitational assisted mineralization.

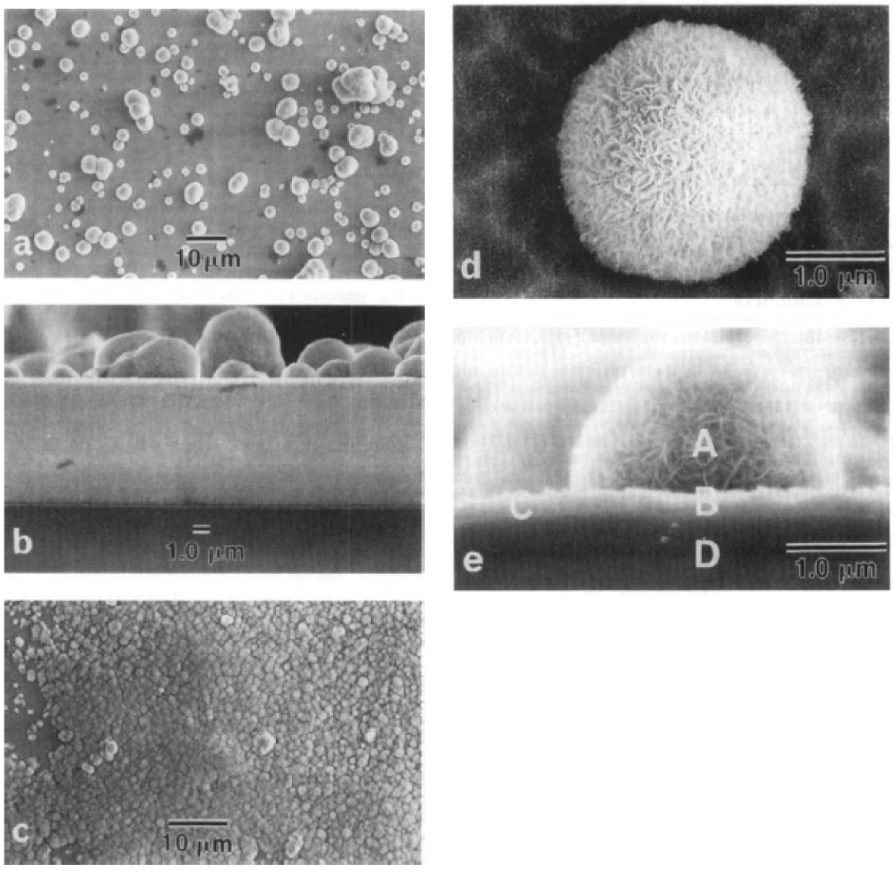

Figure 1.6: SEM studies of three porous silicon surfaces heavily 'aged' by lengthy storage in ambient air. A) and B) Mineralization on pSi area after 7 days exposure to SBF. C) Mineralization layer on bulk silicon area adjacent to pSi after 6 days exposure to SBF. D) Isolated apatite spherulite on bulk silicon. E) Apatite spherulite on bulk silicon area after 4 weeks in SBF.[36]

Ducheyne and co-workers used silane-based chemistry to explore the effect of functionality on calcium phosphate mineralization from SBF.[35] This study looked at

four surface chemistries – oxide, -NH_2, -COOH, and -OH – in SBF for 1, 7, 14, and 21 days at 37˚C pH 7.4. Surfaces were placed in the bottom of 20 mL of SBF solution with continuous shaking. The surfaces displayed differences in the amount of calcium phosphate mineralization on the surface as a result of surface chemistry (Figures 1.7 and 1.8) in addition to differences in crystallinty (pXRD results). These results contradict results presented for both titanium[38,39] and gold[37,40,41,91] functionalized surfaces, where either -COOH or -PO_4H_2 functional groups demonstrated the most calcium phosphate mineralization. While the morphological analysis of this study is not as detailed as would be ideal, it does demonstrate the ability of surface chemistry to provide insight to calcium phosphate mineralization *in vitro*.

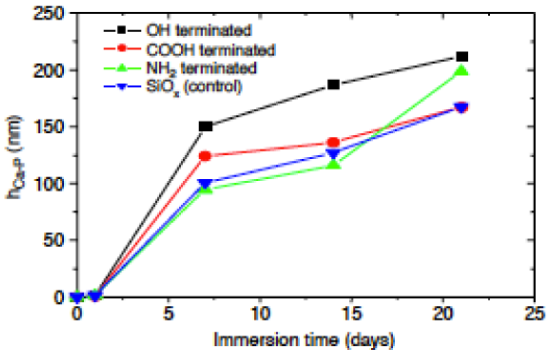

Figure 1.7: Thickness of calcium phosphate on silane-functionalized silicon surfaces as measured via ellipsometry after 1, 7, 14, and 21 days of immersion in SBF. [35]

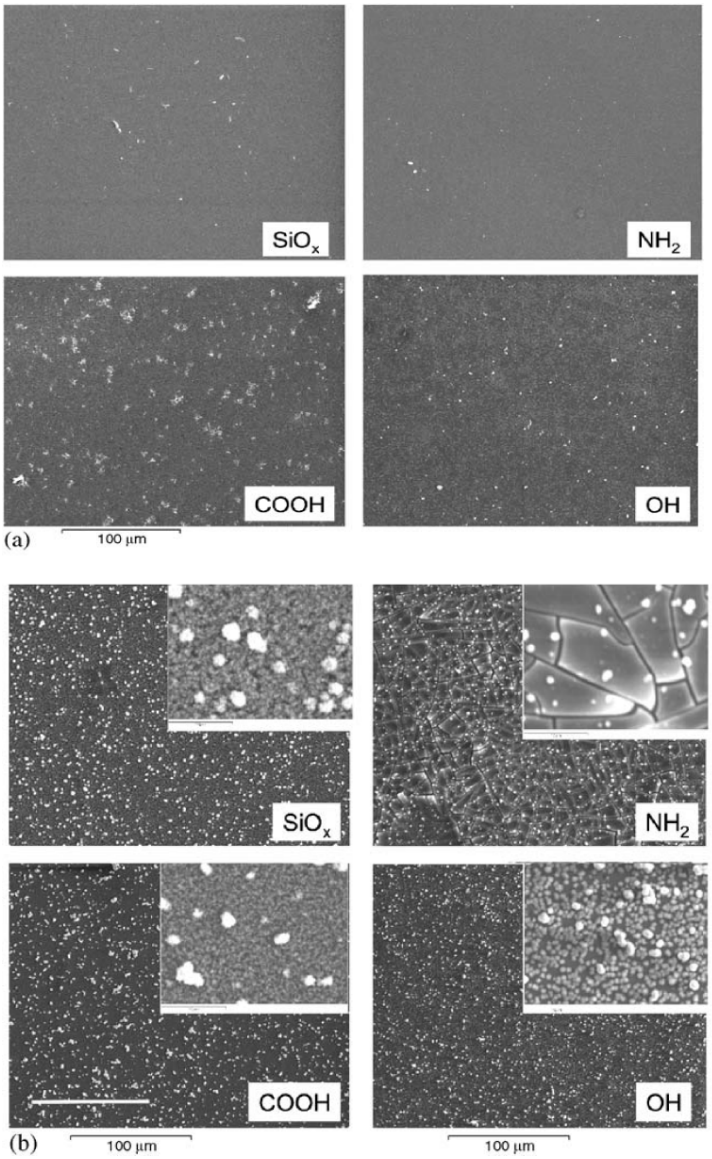

Figure 1.8: SEM images showing calcium phosphate precipitation on SiO_x (oxide), -NH_2, -COOH, and -OH surface chemistries after immersion in SBF for 1 (A) and 7 (B) days. The inserts in B are 10 x representations of the figures.[35]

Bulk and polysilicon surfaces have been explored for hydroxyapatite formation on oxidized silicon surfaces.[86-90] The primary goal of all these studies was to demonstrate hydroxyapatite mineralization for integration into biological systems. Polysilicon is used in fabrication of microstructures on silicon surfaces. In this

study,[82] degradation of the polysilicon layer was observed in SBF depending upon the application parameters of the polysilicon. However, a specific polysilicon condition was able to demonstrate calcium phosphate mineralization under SBF conditions. Ma and co-workers[89] showed successful mineralization on oxidized Si (100) and Si (111) surfaces. While the bulk morphology on the surface varied, the micro-structure was similar to spherulites observed by Canham on pSi surfaces.[36] Increased cell attachment was also successful on these surfaces.

Recent work by Sommerdijk and co-workers has started to examine the effect of surfaces functionalized with carboxylates have on the formation of calcium phosphate.[92] This work utilized porous silicon carbide substrates whose surface chemistry is similar to that of silicon with the exception that treatment with hydrofluoric acid leaves a hydroxyl terminated surface rather than hydrogen terminated. Both silanes and primary alkenes (hydrosilylation) can be used to functionalize the surface. The surfaces in this work are functionalized with primary alkenes. This work extensively characterized not only the mineral morphology but also the phase present on the surface after mineralization at 37˚C for one month or 50˚C for 5 days in Tris-buffered calcium phosphate solutions. Mineral morphology varied based upon the surface chemistry (Figure 1.9). Unmodified SiC surfaces displayed a mix of plate- and needle-like mineral morphologies (Figure 1.9A) while the carboxylate functionalized surface had homogeneous coverage of a plate-like calcium phosphate crystals (Figure 1.9B). A combination of EDX, TEM, and SAED

investigations concluded that the mineral formed on the carboxylate-functionalized SiC surface was a highly crystalline coating of a mixture of OCP and HA. Interestingly, this study was also able to demonstrate that the pores had not been 'clogged' as a result of mineral formation allowing for future biological studies that require diffusion of solution and small molecules.

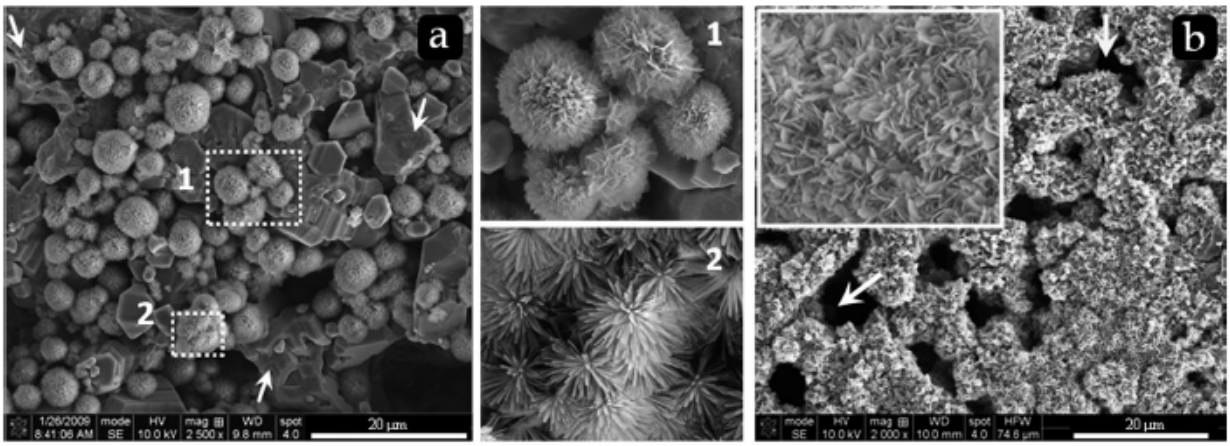

Figure 1.9: SEM images of mineralized SiC. A) Unmodified SiC substrate containing two types of crystals – plate-like (Inset 1) and needle-like (Inset 2) – with arrows indicated the bare SiC surface. B) Carboxylate-functionalized SiC substrate showing homogenous coverage of plate-like crystals (inset) with arrows indicating open pores of the SiC substrate.[92]

1.4.2 Titanium

Titanium substrates are the most extensively research of the three metal substrates due to their direct application in biomedical implants.[93-99] The primary goal of calcium phosphate mineralization studies on titanium has been to improve the biocompatibility of the implants (screws, rods, plates, etc.)[98-100]

1.4.2.1 Surface Functionalization Methods

The primary methods of titanium surface modification include chemical functionalization, deposition, and electrochemical modifications.[86-90] Chemical methods include treatment with acid/base to create an oxide layer or porous oxide[97] on the surface as well as silane based functionalization to attach chemically well-defined monolayers.[39,101] Deposition techniques utilize chemical vapor deposition (CVD), plasma deposition, thermal spray, and physical vapor deposition (PVD), to name a few, with the primary goal of adding materials such as hydroxyapatite (HA), TiN, TiC, TiCN, calcium silicate, and TiO_2.[95,97,98,102] Electrochemical anodization is used to add an oxide layer to the titanium surface while also potentially incorporating electrolyte ions present in the solution or to create a porous surface morphology.[97] For the purpose of this text, the focus will be on chemical methods of surface modification.

Titanium can be oxidized by immersion in an acid/hydrogen peroxide or sodium hydroxide to create a TiO_x layer on the surface.[97,103,104] This layer can then be used as an 'attachment' platform for deposition of hydroxyapatite. Alternatively, silanes ($R\text{-}SiCl_3$) can be directly attached to the oxide layer on the titanium (Figure 1.10). The silane-based monolayer chemistry utilizes trichlorosilane molecules of the general structure $R\text{-}SiCl_3$ to react with the -OH of the titanium oxide to attach monolayer chemistry to the substrate where the R group consists of an alkene spacer with a chemically specific head group (i.e., -OH, -COOH, $-CH_2{=}CH_2$, etc.). Silane-

based chemistry is also a common reaction schematic used in the functionalization of glass and silicon substrates as discussed in Section 1.4.1.1 (Figure 1.5). The monolayers attached to titanium via this method have a similar amount of disorder to that of the silane-based monolayers on silicon surfaces. The addition of biologically relevant molecules (i.e. proteins, small molecules, peptides, amino acids, etc.) is facilitated by using covalent coupling chemistry via the terminal carboxylate groups.[105]

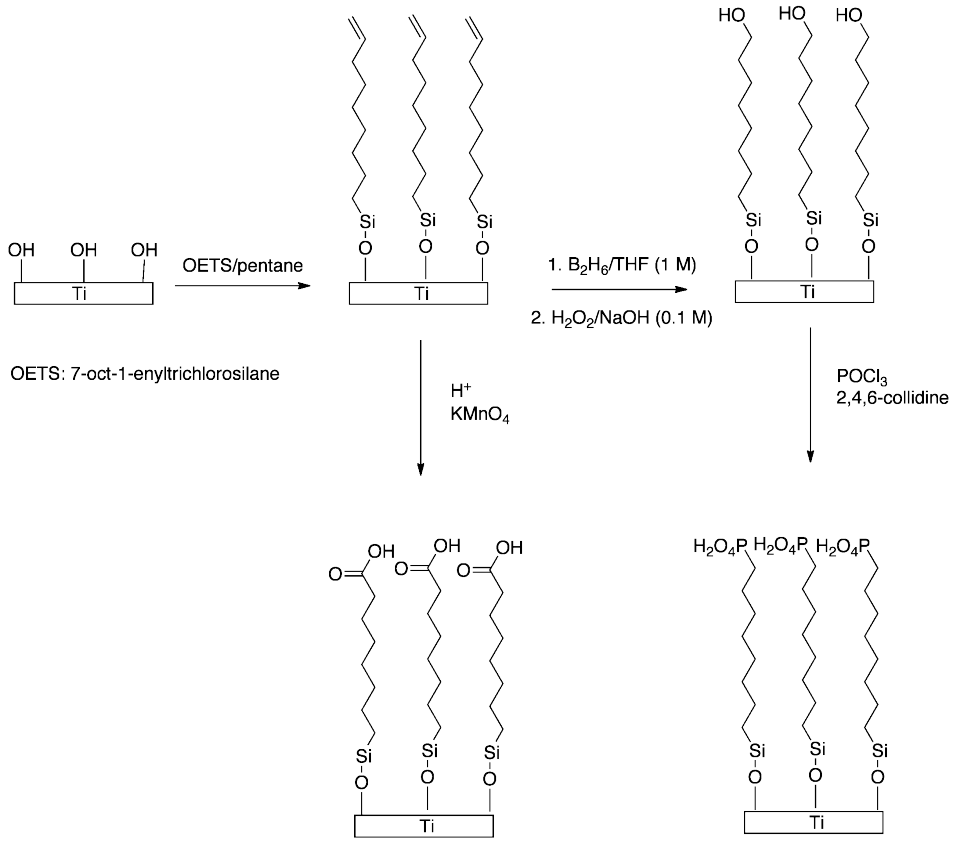

Figure 1.10: Schematic of synthetic routes used to prepare alkene, -COOH, -OH, and -PO_4H_2 monolayers on titanium surfaces.[38]

1.4.2.2 Mineralization Results

Improving the osteoconductive properties of the titanium surface for implants in the body has been the goal of most HA mineralization studies on titanium substrates.[99] These studies have shown coating the titanium surface with HA improves the ability of bone to grow into/on a surface (i.e., osteoconductivity).[94] Studies quantifying the effect of chemistries, other than the oxide,[106]on the ability to form hydroxyapatite on the titanium surface have used silane-based chemistry and mineralization in SBF at 37˚C to emulate physiological conditions.[38,39,93,101,107]

Four main functional groups have been targeted in the mineralization studies: -COOH, -OH, $-SO_3H$, and $-PO_4H_2$. Colby and co-workers[39] demonstrated that after 30 days immersion in SBF at 37˚C that surface chemistry had a distinct effect on both the amount (COOH> PO_4H_2>SO_3H>OH, Figure 1.11) and crystallinity (COOH and SO_3H were more crystalline) of the deposited mineral on the surface. A similar study was carried out by Liu and co-workers.[38] However, this study showed that $-PO_4H_2$ increased nucleation of hydroxyapatite more than -COOH. Interestingly, both studies, showed that as received titanium (native oxide layer), chemically oxidized titanium surfaces, and -OH monolayers had varying degrees of influence on calcium phosphate mineralization, even though, all three have hydroxyl groups at the surface.

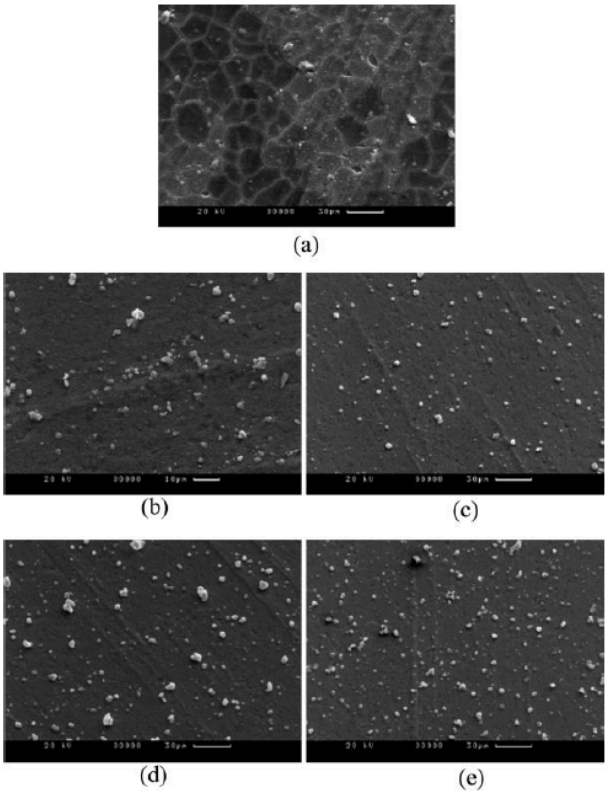

Figure 1.11: SEM images of calcium phosphate mineralization on functionalized titanium surfaces after 30 days immersion in SBF: (A) pure Ti (B) -OH monolayer (C) -SO_3H monolayer (D) -OH monolayer (E) -COOH monolayer.[39]

1.4.3 Gold

Gold surfaces have been studies since the 1980's for their ability to be functionalized via thiol chemistry. Monolayers on gold have been used extensively to study calcium carbonate mineralization,[108-111] with minimal application to calcium phosphate mineralization.[37,40-42,91] Gold is biocompatible and has been used extensively for nanoparticle drug delivery applications.[112-115]

1.4.3.1 Surface Functionalization Methods

Gold monolayer chemistry has been review by Love and coworkers.[116] A summary of self-assembled monolayers on gold using alkanethiols will be presented here. Thiol-based self assembled monolayers (SAMs) are formed by immersion of a clean gold surface in an alkanethiol of the general structure R-$(CH_2)_n$-SH. R is the terminal functional group, the alkane chain is a spacer, and SH is the ligand/head group that binds to the gold substrate (Figure 1.12). The SH group preferentially binds to the gold surface allowing the surface chemistry (-R) to be tailored to a specific application. The packing of the alkyl spacers of the monolayer on the gold surface is the most ordered of all three (Si, Au, and Ti) surfaces and chemistries presented. In vacuum, a well-ordered monolayer on gold forms a 2-D crystal on the surface. The most common -R groups are -OH, -COOH, -NH_2, and -CH_3 for their abundance in biology and commercial availability, as well as being a platform for further chemical functionalization.

One of the more useful chemistries for biological applications to DNA, proteins, and peptides is coupling chemistry in which a carboxylate and primary amine are covalently linked via an amide bond.[117] While the chemistry of alkanethiols are extremely versatile, their stability is such that ligands can be exchanged and/or removed on the surface.[118] The stability of alkanethiol monolayers should be a consideration when experimental conditions require long-term studies or demanding conditions (i.e., strong acid or base, high temperatures, etc.).

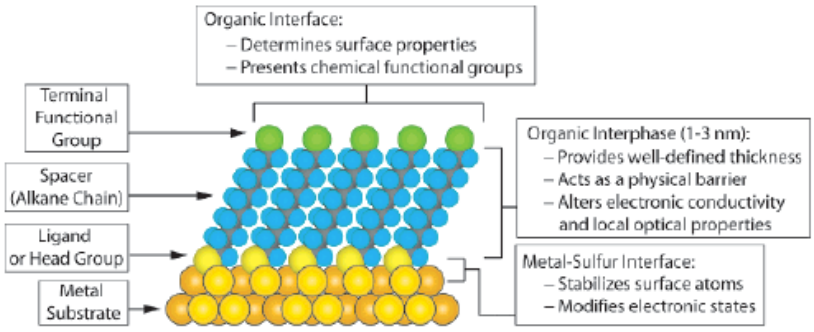

Figure 1.12: Schematic diagram of an ideal self assembled monolayer (SAM) of alkanethiol on gold surface with the anatomy and characteristics of the SAM highlighted.[116]

1.4.3.2 Gold Surfaces and Calcium Phosphate Mineralization

Only a handful of studies, to the best of our knowledge, have been done using SAMs on gold to study calcium phosphate mineralization.[37,40-42,91] Most calcium phosphate mineralization studies on gold SAM surfaces use SBF solutions[37,40-42] with the exception of Hirata's use of ammonium acetate buffered calcium and phosphate solutions.[91] Quartz crystal microbalance (QCM) studies have also been used to quantify the amount of calcium phosphate mineralization.[37,40,41] Matsuda and Tanahashi found that the growth rate varied as a result of SAM R groups, PO_4H_2 > COOH >>$CONH_2$≅OH>NH_2>>CH_3.[40] In fact, patterned islands of methyl SAMs surrounded by carboxylate SAMs, show no mineralization while the carboxylate demonstrated significant mineralization (Figure 1.13). Mineralization studies were carried out from 1 to 30 days in SBF at 37˚C, with most of the results presented for 30 day experiments. While the mineral phase analysis and micro-scale morphology are

not detailed in this study, the terminal functionality of the SAM on gold did have an affect on the formation of calcium phosphate mineral on the surface.

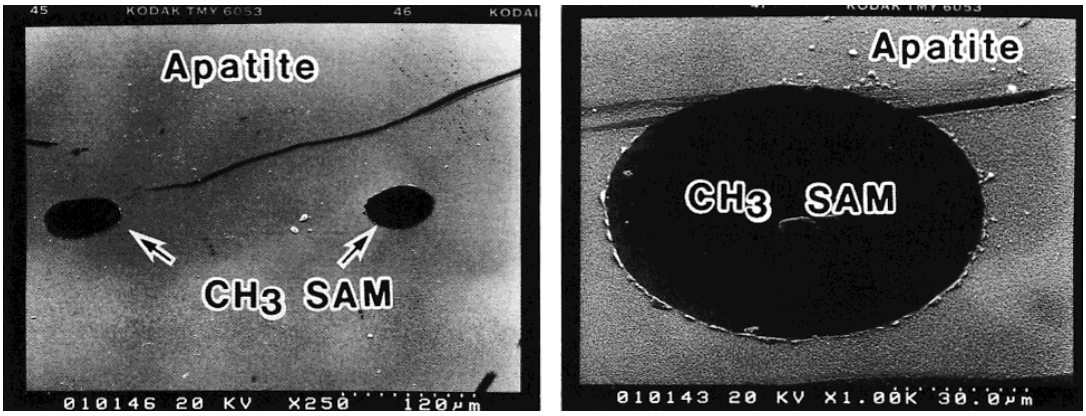

Figure 1.13: SEM images demonstrating a significant amount of mineralization on –COOH terminated SAMs and little on the -CH_3 terminated SAM after 30 days in SBF solution at 37°C.[40]

Allara and co-workers provided a more detailed analysis of calcium phosphate mineralization from SBF solutions on SAMs (-COOH, -OH, and -CH_3) in 2003, especially of the mineral phase present on the surface.[37] The majority of the mineral and kinetic results presented were those of the -COOH surfaces as there was significantly more deposition on the -COOH SAMs than on the -OH or -CH_3 surfaces. Using QCM measurements, the -COOH surfaces demonstrated two regions in the mineralization, an induction period ranging from 11-14 days where almost no mineral is deposited on the surface and a region of extensive growth in which the

mass on the surface changes quickly (Figure 1.14). The measured induction times varied up to 20% over six repeated measurements. This study did show a more detailed set of SEM images (Figure 1.15) for the microstructure of the calcium phosphate on the surface and used Tof-SIMS analysis to determine that the mineral phase on the surface was octacalcium phosphate (OCP) or hydroxyapatite (HA) depending upon the initial calcium concentration. Based upon their data, Allara and co-workers concluded that crystallites were nucleating in solution, adsorbing to the surface, and coalescing into HA on the SAM. In other words, calcium phosphate mineralization was happening via gravitation mineralization rather than directly on the SAM surface, indicating that experimental geometry plays an important role in studying surface versus gravitational mineralization.

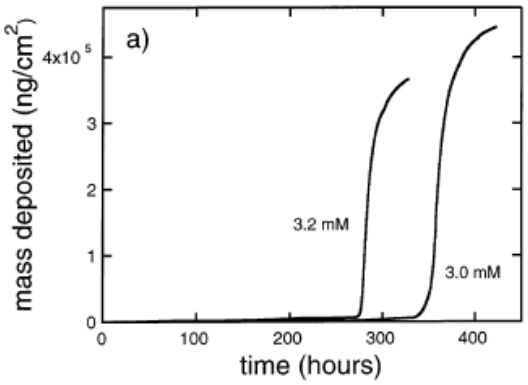

Figure 1.14: Quartz crystal microbalance (QCM) measurements for deposition of calcium phosphate onto a -COOH SAM surface from supersaturated solutions containing 3.0 and 3.2 mM $CaCl_2 \cdot H_2O$. The region of little mass change from 11-14 days was indicative of an induction period with a growth region happening over a period of 48-72 hrs before plateauing.[37]

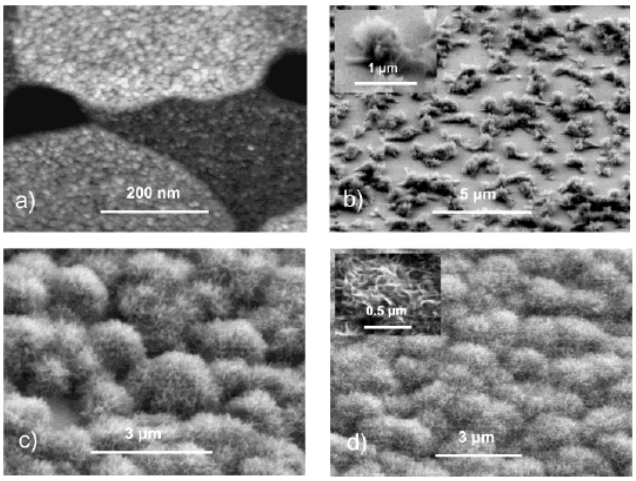

Figure 1.15: AFM (A) and FE-SEM images (45° tilt angle; B, C, D) of calcium phosphate deposition on -COOH SAMs from 3.0 mM calcium solutions. A top AFM view of a calcium phosphate layer on a SAM (A) is shown 40 h into the induction period. SEM images 13 hrs (B), 18 hrs (C), and 53 hrs (D) into the growth region are shown corresponding to total reaction times of 353, 358, and 393 hrs, respectively. Image insets are higher magnifications.[37]

A study published the same year by Koumoto and co-workers using 1.5 SBF solutions quantified electrostatic and pH effects on calcium phosphate mineralization using QCM and SEM analysis.[41] QCM results demonstrated the effect of not only chemistry but also the solution pH and charge across the microbalance resonator (Figure 1.16). At physiological pH 7.4, calcium phosphate mineralization on the SAM surfaces from 1.5 SBF solutions is greatest on -COOH SAM surfaces followed by $-NH_2$ and -OH. While this study analyzed the phase of calcium phosphate on SAM surfaces using XRD, they attempted to distinguish overlapping hydroxyapatite and ocatacalcium phosphate peaks because the data did not go to small enough 2θ to distinguish the two phases (OCP peak at 4.7° 2θ). At pH 7.0, brushite (DCPD) was

observed on the -COOH SAM while according to the data presented, hydroxyapatite was formed all remaining surfaces. SEM analysis of the functionalized resonator surfaces demonstrated varying surface morphology from a continuous 'network' on -OH SAM at pH 7.4 to a particulate network on the -COOH SAM at pH 7.4 (Figure 1.17). This study also reported a series of experiments including ICP measurements, without surfaces, of the mineralization solution in a polypropylene vessel to quantify changes in supersaturation and the effect charge has on mineral formation to determine the mechanism by which calcium phosphate forms on functionalized surfaces. From the data presented, homogenous nucleation occurred in 1.5 SBF solutions $\geq$ 7.4 pH while the charge affected the phase of calcium phosphate present.

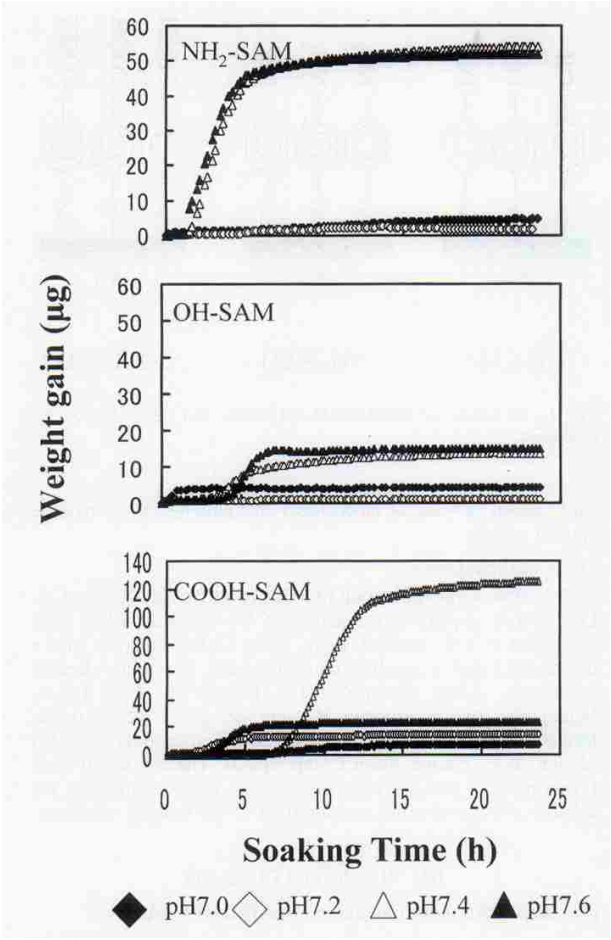

Figure 1.16: Quartz crystal mircrobalance (QCM) measurements for deposition of calcium phosphate onto a -NH_2, -OH, -COOH SAM surfaces from 1.5 SBF solutions at 50°C for pH 7.0, 7.2, 7.4, and 7.6.[41]

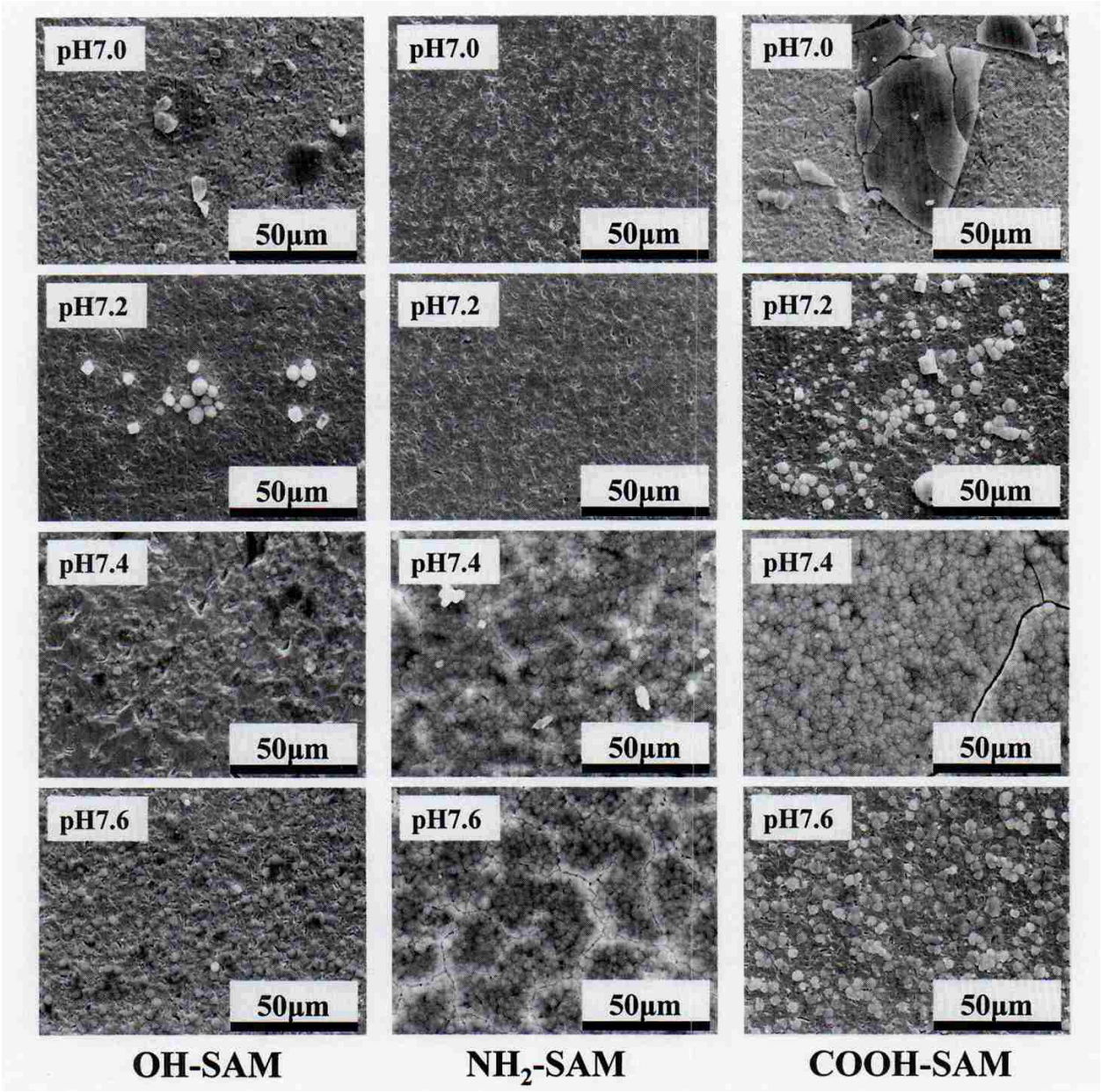

Figure 1.17: SEM analysis of calcium phosphate deposits on -NH_2, -OH, -COOH SAM surfaces after 24 hrs in 1.5 SBF solutions.[41]

Ammonium acetate buffered calcium phosphate solutions at relatively high concentrations (12.5 mM Ca^{2+}, 7.5 mM PO_4^{3-}) were used by Okazaki and co-workers to quantify mineral formation with surface plasmon resonance (SPR) and mineral

morphology with SEM on -NH_2, -OH, -COOH and -CH_3 SAMs.[91] This study was able to show that the thickness of deposited mineral in addition to the morphology was affected by the SAM functionality (Figure 1.18). A 'flake-like' morphology was observed on the -NH_2 and -COOH SAMs, with 'broccoli clusters' observed on the -OH, -COOH, and -CH_3 surfaces. XRD results confirmed the presence of hydroxyapatite, however, the morphology of the surface affected the crystallinity of the hydroxyapatite present. The SPR results indicated that the deposition of the calcium phosphate varied with surface chemistry.

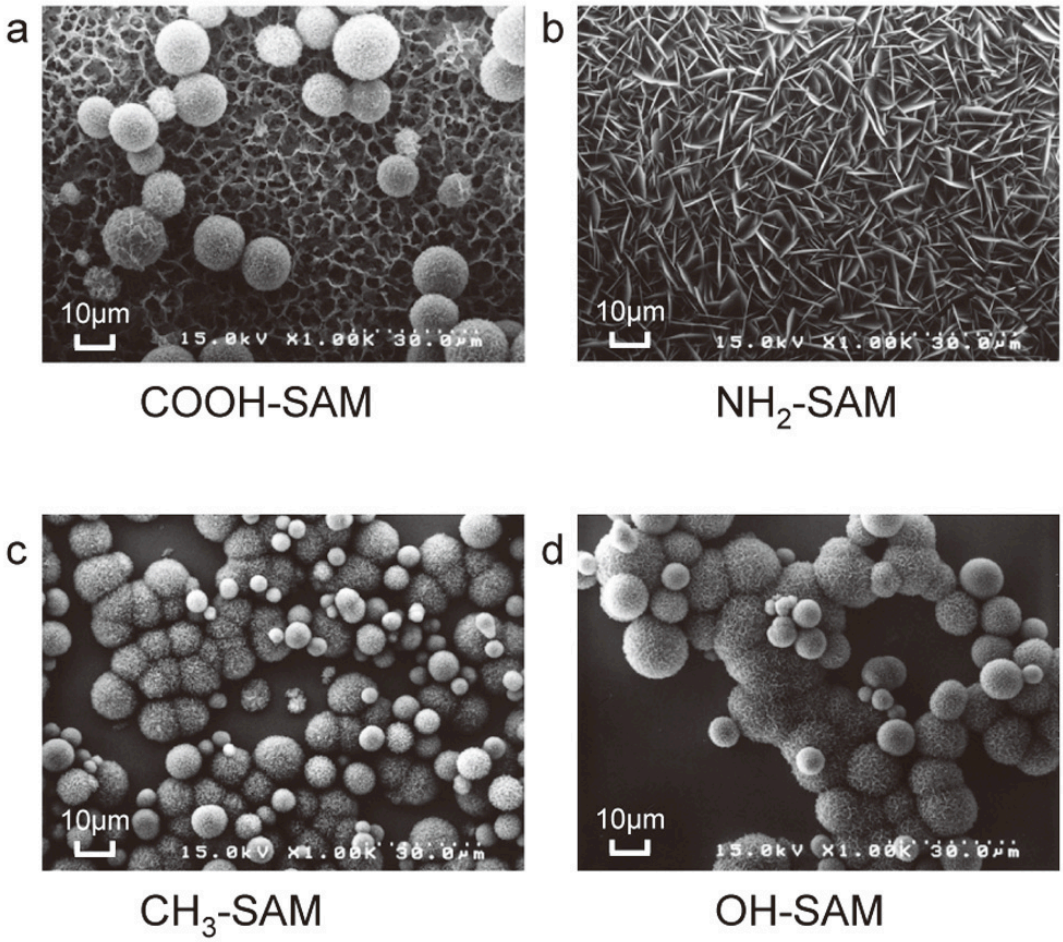

Figure 1.18: SEM analysis of calcium phosphate deposits on -NH_2, -OH, -COOH, and -CH_3 SAM surfaces after 3 days at 37°C ammonium acetate buffered calcium phosphate solutions (12.5 mM Ca^{2+}, 7.5 mM PO_4^{3-}).[91]

A 2012 study by Cui and co-workers has looked at the effect of surface chemistry utilizing a suspended sample geometry, where as all previous studies had used a gravitational-based geometry.[42] The morphology results in this study are similar to those observed by Okazaki using 1.5 SBF solutions rather than ammonium acetate buffered solutions with the exception of the -CH_3 surface (Figure 1.19). Over the period of 14 days, no mineral formation was observed on the -CH_3 SAM surface.

Cross sectional analysis of the -NH_2 and -COOH surfaces indicate a significant difference in the amount of mineral present on the surfaces, 0.3 and 1 μm, respectively. Infrared spectroscopy analysis confirmed hydroxyapatite formation on the -NH_2 and -COOH surfaces and amorphous calcium phosphate on the gold control surface.

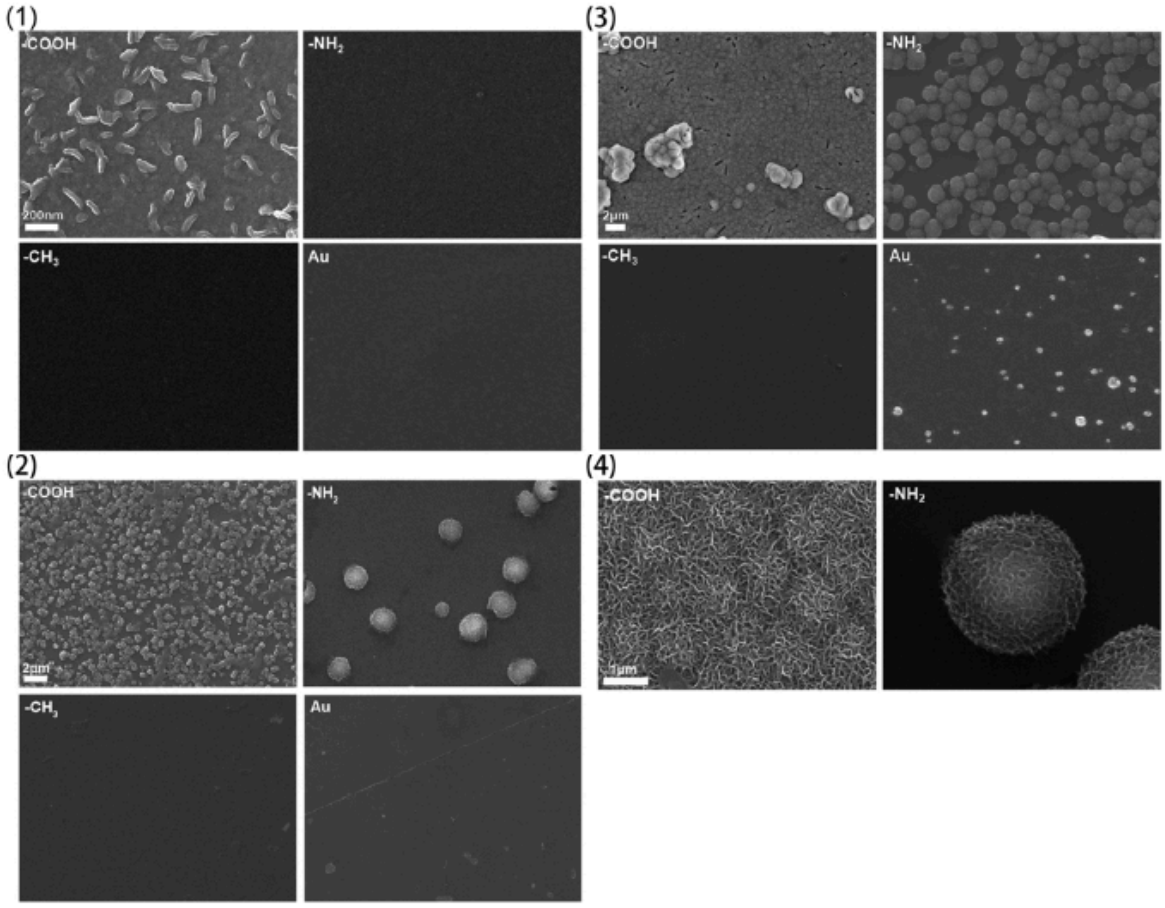

Figure 1.19: SEM analysis of calcium phosphate deposits on -NH_2, -COOH, and -CH_3, SAM surfaces with Au control after 3 (1), 5 (2), and 10 (3) days at 37°C in 1.5 SBF. Enlarged views of the -NH_2 and -COOH SAMs after 10 days (4) are also shown.[42]

The calcium phosphate mineralization studies on SAMs demonstrated that surface chemistry has a clear affect on the formation of calcium phosphate on surfaces after days or weeks in solution.[37,40-42,91] However, none of the studies provide a detailed analysis of the effect of surface chemistry on mineral morphology at various times throughout the mineralization process. The recent study by Cui and co-workers also demonstrates the difference that gravitational vs. suspended geometries have on the mineral formed on -CH_3 SAMs as compared to the mineral formed in the study by Okazaki on the micron scale. The stability of the SAMs in aqueous environments also leads to questions regarding the presence and affect of the chemistry over extended periods of time, indicating that a covalently attached surface chemistry would be preferred for reaction times on the order of days and weeks for calcium phosphate as compared to the relatively short mineralization period (~24 hrs) for calcium carbonate.

1.5 SUMMARY AND OUTLOOK

The use of chemically functionalized surfaces to direct calcium phosphate mineralization holds potential for understanding biological mineralization processes. Biology carefully orchestrates the mineralization process via control of cell-mineral-extracellular matrix interactions. One of the main challenges in understanding calcium phosphate mineralization is the ability to separate the variables (ions, buffering, temperature, surface chemistry, experimental geometry, extracellular matrix, etc.) affecting mineralization.

Table 1.4: Summary of HA mineralization studies on metallic substrates (Au, Ti, and Si) from the literature and presented in this dissertation.

Ref.	Surface	Chemical Route	-R Groups	Solution	Exp. Geometry	Exp. Time	↑ HA	Morphology Differences
[37]	Au	Thiol	COOH, OH, CH_3	SBF	Gravitational	1 - 21 days	COOH	No
[40]	Au	Thiol	CH_3, PO_4H_2, COOH, $CONH_2$, OH, NH_2	SBF	Gravitational	1 - 30 days	PO_4	No
[41]	Au	Thiol	COOH, OH, NH_2	1.5 SBF	Gravitational	24 hrs	COOH	Yes[a]
[91]	Au	Thiol	CH_3, COOH, OH, NH_2	Buffered	Gravitational	3-7 days	COOH	Yes[a]
[42]	Au	Thiol	CH_3, COOH, NH_2	SBF	Suspended	3-14 days	COOH	Yes[a]
[38]	Ti	Silane-based	Alkene, OH, PO_4H_2, COOH	SBF	Gravitational	18 hrs - 1+ wks	PO_4	No
[39]	Ti	Silane-based	OH, SO_3H, PO_4H_2, COOH	SBF	Gravitational	1 - 30 days	COOH	No
[35]	SiO_2	Silane-based	OH, NH_2, COOH	SBF	Gravitational	1 - 21 days	OH	No
[36]	Si	Oxidation	OH	SBF	Gravitational	1 day - 6 wks	-	No
[92]	SiC	Hydro-silyation	OH, COOH	Buffered	Gravitational	5-30 days	COOH	Yes[b]
This work (Chap. 2)	Si	Hydro-silyation	OH, COOH, CH_3, PO_4, BSA, OPN	buffered and un-buffered	Suspended	Buffered: 18 hr – 7 days Unbuffered: 100 - 600 min	PO_4 (Static pH)	Yes[b]

[a]Micron-scale deposition differences observed in calcium phosphate coverage on the surface.
[b]Nano-scale morphology differences observed as calcium phosphate forms.

The mineralization studies presented in Section 1.4 demonstrate the potential for surface chemistry to direct calcium phosphate mineralization. Many of them, however, are not well-controled in regards to experimental geometry, surface chemistry, and morphological analysis (Table 1.4). By controlling the experimental geometry and solution conditions, a morphological difference of the calcium phosphate as a result of surface chemistry is observed (Chapter 2). Further understanding of heterogeneous nucleation of calcium phosphates requires control over the mineralization environment via solution composition, temperature regulation, extracellular matrix, and surface chemistry. Development of *in vitro* models for studying calcium phosphate mineralization is an important step towards understanding and utilizing biology's control over calcium phosphate nucleation and growth.

1.6 OUTLINE OF DISSERTATION

In this dissertation, I present work towards developing an *in vitro* model of calcium phosphate mineralization. To understand the effect of surface chemistry, Chapter 2 of this dissertation presents a study using functionalized porous silicon surfaces in a suspended geometry to study surface nucleated calcium phosphate mineralization. Three solution conditions – buffered, unbuffered-titration controlled, and unbuffered-static – were systematically tested, each building off the previous to exert more control over the solution composition and temperature or quantify silicon

surface nucleation. The effect of proteins at interfaces also plays an important role in applying *in vitro* mineralization results to *in vivo* systems. I covalently bound bovine serum albumin (BSA) and osteopontin (OPN) to pSi surfaces. The third chapter of this dissertation focuses on the development of a hydrogel-based double diffusion system for studying calcium phosphate mineralization in a 3-D environment with cell incorporation. Cell culture compatible agarose gel was used to model the extracellular matrix in the development of a double diffusion calcium phosphate mineralization system for cellular studies in an incubator, an important tool in the study of cell – mineral – matrix interactions *in vitro*. The last chapter presents a study of physisorbed protein (silk fibroin and BSA) on gold monolayers with respect to the IR peak positions relation to surface conformation as well as the amount of surface bound protein (Chapter 4).

REFERENCES

(1) Mann, S. *Biomineralization: Principles and Concepts in Bioinorganic Materials Chemistry*; Oxford University Press: Oxford, UK, 2001.

(2) Palmer, L. C.; Newcomb, C. J.; Kaltz, S. R.; Spoerke, E. D.; Stupp, S. I., Biomimetic Systems for Hydroxyapatite Mineralization Inspired by Bone and Enamel, *Chem. Rev.* **2008**, *108*, 4754.

(3) Salgado, A. J.; Coutinho, O. P.; Reis, R. L., Bone Tissue Engineering: State of the Art and Future Trends, *Macromol. Biosci.* **2004**, *4*, 743.

(4) LeGeros, R. Z., Calcium Phosphate-Based Osteoinductive Materials, *Chem. Rev.* **2008**, *108*, 4742.

(5) Weiner, S.; Wagner, H. D., The Material Bone: Structure Mechanical Function Relations, *Annu. Rev. Mater. Sci.* **1998**, *28*, 271.

(6) Robinson, C.; Kirkham, J.; Shore, R. *Dental Enamel : Formation to Destruction*; CRC Press: Boca Raton, 1995.

(7) Tamerler, C.; Sarikaya, M., Molecular Biomimetics: Genetic Synthesis, Assembly, and Formation of Materials Using Peptides, *MRS Bull.* **2008**, *33*, 504.

(8) Dorozhkin, S. V., Calcium Orthophosphates, *Journal of Materials Science* **2007**, *42*, 1061.

(9) Nakano, T.; Kaibara, K.; Tabata, Y.; Nagata, N.; Enomoto, S.; Marukawa, E.; Umakoshi, Y., Unique Alignment and Texture of Biological Apatite Crystallites in Typical Calcified Tissues Analyzed by Microbeam X-Ray Diffractometer System, *Bone* **2002**, *31*, 479.

(10) De Groot, K. *Bioceramics of Calcium Phosphate*; CRC Press: Boca Raton, 1983.

(11) Wang, L. J.; Nancollas, G. H., Calcium Orthophosphates: Crystallization and Dissolution, *Chem. Rev.* **2008**, *108*, 4628.

(12) Dorozhkin, S. V., Amorphous Calcium (Ortho)Phosphates, *Acta Biomaterialia* **2010**, *6*, 4457.

(13) Koutsoukos, P. G.; Nancollas, G. H., The Morphology of Hydroxyapatite Crystals Grown in Aqueous-Solution at 37-Degrees-C, *J. Cryst. Growth* **1981**, *55*, 369.

(14) Iijima, M.; Moriwaki, Y., Effects of Inorganic-Ions on Morphology of Octacalcium Phosphate Grown on Cation Selective-Membrane at Physiological Temperature and Ph in Relation to Enamel Formation, *J. Cryst. Growth* **1989**, *96*, 59.

(15) Koutsoukos, P.; Amjad, Z.; Tomson, M. B.; Nancollas, G. H., Crystallization of Calcium Phosphates - Constant Composition Study, *J. Am. Chem. Soc.* **1980**, *102*, 1553.

(16) Johnsson, M. S. A.; Nancollas, G. H., The Role of Brushite and Octacalcium Phosphate in Apatite Formation, *Crit. Rev. Oral Biol. Medicine* **1992**, *3*, 61.

(17) Elliott, J. C. *Structure and Chemistry of the Apatites and Other Calcium Orthophosphates*; Elsevier: Amsterdam [The Netherlands]; New York, 1994.

(18) Sauer, G. R.; Zunic, W. B.; Durig, J. R.; Wuthier, R. E., Fourier-Transform Raman-Spectroscopy of Synthetic and Biological Calcium Phosphates, *Calcified Tissue International* **1994**, *54*, 414.

(19) Fowler, B. O.; Moreno, E. C.; Brown, W. E., Infra-Red Spectra of Hydroxyapatite Octacalcium Phosphate and Pyrolysed Octacalcium Phosphate, *Arch. Oral Biol.* **1966**, *11*, 477.

(20) Pleshko, N.; Boskey, A.; Mendelsohn, R., Novel Infrared Spectroscopic Method for the Determination of Crystallinity of Hydroxyapatite Minerals, *Biophys. J.* **1991**, *60*, 786.

(21) Wuthier, R. E.; Rice, G. S.; Wallace, J. E. B.; Weaver, R. L.; Legeros, R. Z.; Eanes, E. D., Invitro Precipitation of Calcium-Phosphate under Intracellular Conditions - Formation of Brushite from an Amorphous Precursor in the Absence of Atp, *Calcified Tissue International* **1985**, *37*, 401.

(22) Blumenth.Nc; Holmes, J. M.; Posner, A. S., Effect of Preparation Conditions on Properties and Transformation of Amorphous Calcium Phosphate, *Mater. Res. Bull.* **1972**, *7*, 1181.

(23) Baddiel, C. B.; Berry, E. E., Spectra Structure Correlations in Hydroxy and Fluorapatite, *Spectrochim. Acta* **1966**, *22*, 1407.

(24) Burdick, J. A.; Mauck, R. L.; Springer: Wien; New York, 2011.

(25) Raynaud, S.; Champion, E.; Bernache-Assollant, D.; Thomas, P., Calcium Phosphate Apatites with Variable Ca/P Atomic Ratio I. Synthesis, Characterisation and Thermal Stability of Powders, *Biomaterials* **2002**, *23*, 1065.

(26) Rhee, S. H.; Tanaka, J., Hydroxyapatite Coating on a Collagen Membrane by a Biomimetic Method, *J. Am. Ceram. Soc.* **1998**, *81*, 3029.

(27) Raynaud, S.; Champion, E.; Bernache-Assollant, D., Calcium Phosphate Apatites with Variable Ca/P Atomic Ratio Ii. Calcination and Sintering, *Biomaterials* **2002**, *23*, 1073.

(28) Rodriguez-Lorenzo, L. M.; Vallet-Regi, M., Controlled Crystallization of Calcium Phosphate Apatites, *Chem. Mater.* **2000**, *12*, 2460.

(29) Cazalbou, S.; Combes, C.; Eichert, D.; Rey, C., Adaptative Physico-Chemistry of Bio-Related Calcium Phosphates, *J. Mater. Chem.* **2004**, *14*, 2148.

(30) Earl, J. S.; Wood, D. J.; Milne, S. J., Hydrothermal Synthesis of Hydroxyapatite, *Journal of Physics: Conference Series* **2006**, *26*, 268.

(31) Riman, R. E.; Suchanek, W. L.; Byrappa, K.; Chen, C. W.; Shuk, P.; Oakes, C. S., Solution Synthesis of Hydroxyapatite Designer Particulates, *Solid State Ionics* **2002**, *151*, 393.

(32) Pathi, S. P.; Lin, D. D. W.; Dorvee, J. R.; Estroff, L. A.; Fischbach, C., Hydroxyapatite Nanoparticle-Containing Scaffolds for the Study of Breast Cancer Bone Metastasis, *Biomaterials* **2011**, *32*, 5112.

(33) Kokubo, T.; Kushitani, H.; Sakka, S.; Kitsugi, T.; Yamamuro, T., Solutions Able to Reproduce Invivo Surface-Structure Changes in Bioactive Glass-Ceramic a-W3, *J. Biomed. Mater. Res.* **1990**, *24*, 721.

(34) Muller, L.; Muller, F. A., Preparation of Sbf with Different Hco3- Content and Its Influence on the Composition of Biomimetic Apatites, *Acta Biomaterialia* **2006**, *2*, 181.

(35) Toworfe, G. K.; Composto, R. J.; Shapiro, I. M.; Ducheyne, P., Nucleation and Growth of Calcium Phosphate on Amine-, Carboxyl- and Hydroxyl-Silane Self-Assembled Monolayers, *Biomaterials* **2006**, *27*, 631.

(36) Canham, L. T., Bioactive Silicon Structure Fabrication through Nanoetching Techniques, *Adv. Mater.* **1995**, *7*, 1033.

(37) Tarasevich, B. J.; Chusuei, C. C.; Allara, D. L., Nucleation and Growth of Calcium Phosphate from Physiological Solutions onto Self-Assembled Templates by a Solution-Formed Nucleus Mechanism, *J. Phys. Chem. B* **2003**, *107*, 10367.

(38) Liu, Q.; Ding, J.; Mante, F. K.; Wunder, S. L.; Baran, G. R., The Role of Surface Functional Groups in Calcium Phosphate Nucleation on Titanium Foil: A Self-Assembled Monolayer Technique, *Biomaterials* **2002**, *23*, 3103.

(39) Liu, D. P.; Majewski, P.; O'Neill, B. K.; Ngothai, Y.; Colby, C. B., The Optimal Sam Surface Functional Group for Producing a Biomimetic Ha Coating on Ti, *Journal of Biomedical Materials Research Part A* **2006**, *77A*, 763.

(40) Tanahashi, M.; Matsuda, T., Surface Functional Group Dependence on Apatite Formation on Self-Assembled Monolayers in a Simulated Body Fluid, *J. Biomed. Mater. Res.* **1997**, *34*, 305.

(41) Zhu, P. X.; Masuda, Y.; Yonezawa, T.; Koumoto, K., Investigation of Apatite Deposition onto Charged Surfaces in Aqueous Solutions Using a Quartz-Crystal Microbalance, *J. Am. Ceram. Soc.* **2003**, *86*, 782.

(42) Liu, Z.-X.; Wang, X.-M.; Wang, Q.; Shen, X.-C.; Liang, H.; Cui, F.-Z., Evolution of Calcium Phosphate Crystallization on Three Functional Group Surfaces with the Same Surface Density, *CrystEngComm* **2012**.

(43) Wang, L. J.; Guan, X. Y.; Yin, H. Y.; Moradian-Oldak, J.; Nancollas, G. H., Mimicking the Self-Organized Microstructure of Tooth Enamel, *J. Phys. Chem. C* **2008**, *112*, 5892.

(44) Wang, L. J.; Guan, X. Y.; Du, C.; Moradian-Oldak, J.; Nancollas, G. H., Amelogenin Promotes the Formation of Elongated Apatite Microstructures in a Controlled Crystallization System, *J. Phys. Chem. C* **2007**, *111*, 6398.

(45) Yang, X. D.; Wang, L. J.; Qin, Y. L.; Sun, Z.; Henneman, Z. J.; Moradian-Oldak, J.; Nancollas, G. H., How Amelogenin Orchestrates the Organization of Hierarchical Elongated Microstructures of Apatite, *J. Phys. Chem. B* **2010**, *114*, 2293.

(46) Nancollas, G. H.; Henneman, Z. J., Calcium Oxalate: Calcium Phosphate Transformations, *Urol. Res.* **2010**, *38*, 277.

(47) Wang, L. J.; Guan, X. Y.; Tang, R. K.; Hoyer, J. R.; Wierzbicki, A.; De Yoreo, J. J.; Nancollas, G. H., Phosphorylation of Osteopontin Is Required for Inhibition of Calcium Oxalate Crystallization, *J. Phys. Chem. B* **2008**, *112*, 9151.

(48) Kazmierczak, T. F.; Tomson, M. B.; Nancollas, G. H., Crystal-Growth of Calcium-Carbonate - a Controlled Composition Kinetic-Study, *J. Phys. Chem.* **1982**, *86*, 103.

(49) Uskokovic, V.; Kim, M. K.; Li, W.; Habelitz, S., Enzymatic Processing of Amelogenin During Continuous Crystallization of Apatite, *J. Mater. Res.* **2008**, *23*, 3184.

(50) Uskokovic, V.; Li, W.; Habelitz, S., Amelogenin as a Promoter of Nucleation and Crystal Growth of Apatite, *J. Cryst. Growth* **2011**, *316*, 106.

(51) Wei, G. B.; Ma, P. X., Structure and Properties of Nano-Hydroxyapatite/Polymer Composite Scaffolds for Bone Tissue Engineering, *Biomaterials* **2004**, *25*, 4749.

(52) Williams, J. M.; Adewunmi, A.; Schek, R. M.; Flanagan, C. L.; Krebsbach, P. H.; Feinberg, S. E.; Hollister, S. J.; Das, S., Bone Tissue Engineering Using Polycaprolactone Scaffolds Fabricated Via Selective Laser Sintering, *Biomaterials* **2005**, *26*, 4817.

(53) Rizzi, S. C.; Heath, D. T.; Coombes, A. G. A.; Bock, N.; Textor, M.; Downes, S., Biodegradable Polymer/Hydroxyapatite Composites: Surface Analysis and Initial Attachment of Human Osteoblasts, *J. Biomed. Mater. Res.* **2001**, *55*, 475.

(54) Tanahashi, M.; Yao, T.; Kokubo, T.; Minoda, M.; Miyamoto, T.; Nakamura, T.; Yamamuro, T., Apatite Coating on Organic Polymers by a Biomimetic Process, *J. Am. Ceram. Soc.* **1994**, *77*, 2805.

(55) Stewart, M. P.; Buriak, J. M., Chemical and Biological Applications of Porous Silicon Technology, *Adv. Mater.* **2000**, *12*, 859.

(56) Buriak, J. M., Organometallic Chemistry on Silicon and Germanium Surfaces, *Chem. Rev.* **2002**, *102*, 1271.

(57) Song, J. H.; Sailor, M. J., Chemical Modification of Crystalline Porous Silicon Surfaces, *Comments Inorg. Chem.* **1999**, *21*, 69.

(58) Anderson, R. C.; Muller, R. S.; Tobias, C. W., Chemical Surface Modification of Porous Silicon, *J. Electrochem. Soc.* **1993**, *140*, 1393.

(59) Dubin, V. M.; Vieillard, C.; Ozanam, F.; Chazalviel, J. N., Preparation and Characterization of Surface-Modified Luminescent Porous Silicon, *Physica Status Solidi B-Basic Research* **1995**, *190*, 47.

(60) Parikh, A. N.; Liedberg, B.; Atre, S. V.; Ho, M.; Allara, D. L., Correlation of Molecular-Organization and Substrate Wettability in the Self-Assembly of N-Alkylsiloxane Monolayers, *J. Phys. Chem.* **1995**, *99*, 9996.

(61) Bateman, J. E.; Eagling, R. D.; Worrall, D. R.; Horrocks, B. R.; Houlton, A., Alkylation of Porous Silicon by Direct Reaction with Alkenes and Alkynes, *Angewandte Chemie-International Edition* **1998**, *37*, 2683.

(62) Sieval, A. B.; Demirel, A. L.; Nissink, J. W. M.; Linford, M. R.; van der Maas, J. H.; de Jeu, W. H.; Zuilhof, H.; Sudholter, E. J. R., Highly Stable Si-C Linked Functionalized Monolayers on the Silicon (100) Surface, *Langmuir* **1998**, *14*, 1759.

(63) Warntjes, M.; Vieillard, C.; Ozanam, F.; Chazalviel, J. N., Electrochemical Methoxylation of Porous Silicon Surface, *J. Electrochem. Soc.* **1995**, *142*, 4138.

(64) Bansal, A.; Li, X. L.; Lauermann, I.; Lewis, N. S.; Yi, S. I.; Weinberg, W. H., Alkylation of Si Surfaces Using a Two-Step Halogenation Grignard Route, *J. Am. Chem. Soc.* **1996**, *118*, 7225.

(65) Webb, L. J.; Lewis, N. S., Comparison of the Electrical Properties and Chemical Stability of Crystalline Silicon(111) Surfaces Alkylated Using Grignard Reagents or Olefins with Lewis Acid Catalysts, *J. Phys. Chem. B* **2003**, *107*, 5404.

(66) Juang, A.; Scherman, O. A.; Grubbs, R. H.; Lewis, N. S., Formation of Covalently Attached Polymer Overlayers on Si(111) Surfaces Using Ring-Opening Metathesis Polymerization Methods, *Langmuir* **2001**, *17*, 1321.

(67) Voicu, R.; Boukherroub, R.; Bartzoka, V.; Ward, T.; Wojtyk, J. T. C.; Wayner, D. D. M., Formation, Characterization, and Chemistry of Undecanoic Acid-Terminated Silicon Surfaces: Patterning and Immobilization of DNA, *Langmuir* **2004**, *20*, 11713.

(68) Canham, L. *Properties of Porous Silicon*; The Institution of Electrical Engineers: United Kingdom: INSPEC, 1997.

(69) Faucheux, N.; Schweiss, R.; Lutzow, K.; Werner, C.; Groth, T., Self-Assembled Monolayers with Different Terminating Groups as Model Substrates for Cell Adhesion Studies, *Biomaterials* **2004**, *25*, 2721.

(70) Linford, M. R.; Fenter, P.; Eisenberger, P. M.; Chidsey, C. E. D., Alkyl Monolayers on Silicon Prepared from 1-Alkenes and Hydrogen-Terminated Silicon, *J. Am. Chem. Soc.* **1995**, *117*, 3145.

(71) Wang, P. Y.; Clements, L. R.; Thissen, H.; Jane, A.; Tsai, W. B.; Voelcker, N. H., Screening Mesenchymal Stem Cell Attachment and Differentiation on Porous Silicon Gradients, *Adv. Funct. Mater.* **2012**, *22*, 3414.

(72) El-Ghannam, A., Bone Reconstruction: From Bioceramics to Tissue Engineering, *Expert Review of Medical Devices* **2005**, *2*, 87.

(73) McInnes, S. J. P.; Voelcker, N. H., Silicon-Polymer Hybrid Materials for Drug Delivery, *Future Medicinal Chemistry* **2009**, *1*, 1051.

(74) Ni, M.; Tong, W. H.; Choudhury, D.; Rahim, N. A. A.; Iliescu, C.; Yu, H., Cell Culture on Mems Platforms: A Review, *International Journal of Molecular Sciences* **2009**, *10*, 5411.

(75) Brook, M. A. *Silicon in Organic, Organometallic, and Polymer Chemistry*; Wiley: New York, 2000.

(76) Smith, E. A.; Chen, W., How to Prevent the Loss of Surface Functionality Derived from Aminosilanes, *Langmuir : the ACS journal of surfaces and colloids* **2008**, *24*, 12405.

(77) Morral, A. F. I.; Cabarrocas, P. R. I., Shedding Light on the Growth of Amorphous, Polymorphous, Protocrystalline and Microcrystalline Silicon Thin Films, *Thin Solid Films* **2001**, *383*, 161.

(78) Kern, W.; Noyes Publications: Park Ridge, N.J., U.S.A., 1993.

(79) Metwalli, E.; Haines, D.; Becker, O.; Conzone, S.; Pantano, C. G., Surface Characterizations of Mono-, Di-, and Tri-Aminosilane Treated Glass Substrates, *J. Colloid Interf. Sci.* **2006**, *298*, 825.

(80) Nemanick, E. J.; Solares, S. D.; Goddard, W. A., III; Lewis, N. S., Quantum Mechanics Calculations of the Thermodynamically Controlled Coverage and Structure of Alkyl Monolayers on Si(111) Surfaces, *J. Phys. Chem. B* **2006**, *110*, 14842.

(81) Cras, J. J.; Rowe-Taitt, C. A.; Nivens, D. A.; Ligler, F. S., Comparison of Chemical Cleaning Methods of Glass in Preparation for Silanization, *Biosens. Bioelectron.* **1999**, *14*, 683.

(82) Canham, L. T.; Reeves, C. L.; Loni, A.; Houlton, M. R.; Newey, J. P.; Simons, A. J.; Cox, T. I., Calcium Phosphate Nucleation on Porous Silicon: Factors Influencing Kinetics in Acellular Simulated Body Fluids, *Thin Solid Films* **1997**, *297*, 304.

(83) Li, X.; Coffer, J. L.; Chen, Y. D.; Pinizzotto, R. F.; Newey, J.; Canham, L. T., Transition Metal Complex-Doped Hydroxyapatite Layers on Porous Silicon, *J. Am. Chem. Soc.* **1998**, *120*, 11706.

(84) Pramatarova, L.; Pecheva, E.; Dimova-Malinovska, D.; Pramatarova, R.; Bismayer, U.; Petrov, T.; Minkovski, N., Porous Silicon as a Substrate for Hydroxyapatite Growth, *Vacuum* **2004**, *76*, 135.

(85) Chadwick, E. G.; Clarkin, O. M.; Tanner, D. A., Hydroxyapatite Formation on Metallurgical Grade Nanoporous Silicon Particles, *Journal of Materials Science* **2010**, *45*, 6562.

(86) Chung, R. J.; Hsieh, M. F.; Panda, R. N.; Chin, T. S., Hydroxyapatite Layers Deposited from Aqueous Solutions on Hydrophilic Silicon Substrate, *Surface & Coatings Technology* **2003**, *165*, 194.

(87) Chung, R.-J.; Chin, T. S.; Cheng, H.-Y.; Wen, H.-W.; Hsieh, M.-F., Photo-Luminescent Hydroxyapatite Coatings through a Bio-Mimetic Process, *Biomol. Eng* **2007**, *24*, 459.

(88) Wang, P. E.; Chaki, T. K., Hydroxyapatite Films on Silicon Single-Crystals by a Solution Technique - Texture, Supersaturation and Ph-Dependence, *Journal of Materials Science-Materials in Medicine* **1995**, *6*, 94.

(89) Chong, S. C.; Loo, J.; Lee, P. S.; Ma, J., Biomimetic Processing of Bioactive Interface on Silicon Substrates, *Journal of Biomedical Materials Research Part B-Applied Biomaterials* **2008**, *85B*, 368.

(90) Canham, L. T.; Reeves, C. L.; King, D. O.; Branfield, P. J.; Crabb, J. G.; Ward, M. C. L., Bioactive Polycrystalline Silicon, *Adv. Mater.* **1996**, *8*, 850.

(91) Hirata, I.; Akamatsu, M.; Fujii, E.; Poolthong, S.; Okazaki, M., Chemical Analyses of Hydroxyapatite Formation on Sam Surfaces Modified with Cooh, Nh2, Ch3, and Oh Functions, *Dent. Mater. J.* **2010**, *29*, 438.

(92) Dey, A.; van den Hoogen, C. J.; Rosso, M.; Lousberg, N.; Hendrix, M.; Friedrich, H.; Ramirez-Rico, J.; Zuilhof, H.; de With, G.; Sommerdijk, N., Biomimetic Mineralization of Calcium Phosphate on a Functionalized Porous Silicon Carbide Biomaterial, *Chempluschem* **2012**, *77*, 694.

(93) Soballe, K.; Hansen, E. S.; Rasmussen, H. B.; Jorgensen, P. H.; Bunger, C., Tissue Ingrowth into Titanium and Hydroxyapatite-Coated Implants During Stable and Unstable Mechanical Conditions, *J. Orth. Res.* **1992**, *10*, 285.

(94) Suchanek, W.; Yoshimura, M., Processing and Properties of Hydroxyapatite-Based Biomaterials for Use as Hard Tissue Replacement Implants, *J. Mater. Res.* **1998**, *13*, 94.

(95) Habibovic, P.; Barrere, F.; van Blitterswijk, C. A.; de Groot, K.; Layrolle, P., Biomimetic Hydroxyapatite Coating on Metal Implants, *J. Am. Ceram. Soc.* **2002**, *85*, 517.

(96) Kokubo, T.; Kim, H. M.; Kawashita, M.; Nakamura, T., Bioactive Metals: Preparation and Properties, *Journal of Materials Science-Materials in Medicine* **2004**, *15*, 99.

(97) Liu, X. Y.; Chu, P. K.; Ding, C. X., Surface Modification of Titanium, Titanium Alloys, and Related Materials for Biomedical Applications, *Materials Science & Engineering R-Reports* **2004**, *47*, 49.

(98) Yang, Y. Z.; Kim, K. H.; Ong, J. L., Review on Calcium Phosphate Coatings Produced Using a Sputtering Process - an Alternative to Plasma Spraying, *Biomaterials* **2005**, *26*, 327.

(99) Variola, F.; Vetrone, F.; Richert, L.; Jedrzejowski, P.; Yi, J.-H.; Zalzal, S.; Clair, S.; Sarkissian, A.; Perepichka, D. F.; Wuest, J. D.; Rosei, F.; Nanci, A., Improving Biocompatibitity of Implantable Metals by Nanoscale Modification of Surfaces: An Overview of Strategies, Fabrication Methods, and Challenges, *Small* **2009**, *5*, 996.

(100) Pham, M. T.; Maitz, M. F.; Reuther, H.; Muecklich, A.; Prokert, F.; Steiner, G., Nucleation of Calcium Phosphate by Surface-Bound Extracellular Matrix, *Journal of Biomedical Materials Research Part A* **2004**, *71A*, 16.

(101) Nanci, A.; Wuest, J. D.; Peru, L.; Brunet, P.; Sharma, V.; Zalzal, S.; McKee, M. D., Chemical Modification of Titanium Surfaces for Covalent Attachment of Biological Molecules, *J. Biomed. Mater. Res.* **1998**, *40*, 324.

(102) Ducheyne, P.; Vanraemdonck, W.; Heughebaert, J. C.; Heughebaert, M., Structural-Analysis of Hydroxyapatite Coatings on Titanium, *Biomaterials* **1986**, *7*, 97.

(103) Bunker, B. C.; Rieke, P. C.; Tarasevich, B. J.; Campbell, A. A.; Fryxell, G. E.; Graff, G. L.; Song, L.; Liu, J.; Virden, J. W.; McVay, G. L., Ceramic Thin-Film Formation on Functionalized Interfaces through Biomimetic Processing, *Science* **1994**, *264*, 48.

(104) Campbell, A. A.; Fryxell, G. E.; Linehan, J. C.; Graff, G. L., Surface-Induced Mineralization: A New Method for Producing Calcium Phosphate Coatings, *J. Biomed. Mater. Res.* **1996**, *32*, 111.

(105) Quinton, D.; Galtayries, A.; Prima, F.; Griveau, S., Functionalization of Titanium Surfaces with a Simple Electrochemical Strategy, *Surface & Coatings Technology* **2012**, *206*, 2302.

(106) Jonasova, L.; Muller, F. A.; Helebrant, A.; Strnad, J.; Greil, P., Biomimetic Apatite Formation on Chemically Treated Titanium, *Biomaterials* **2004**, *25*, 1187.

(107) Hanawa, T.; Ota, M., Calcium-Phosphate Naturally Formed on Titanium in Electrolyte Solution, *Biomaterials* **1991**, *12*, 767.

(108) Aizenberg, J.; Black, A. J.; Whitesides, G. H., Oriented Growth of Calcite Controlled by Self-Assembled Monolayers of Functionalized Alkanethiols Supported on Gold and Silver, *J. Am. Chem. Soc.* **1999**, *121*, 4500.

(109) Cusack, M.; Freer, A., Biomineralization: Elemental and Organic Influence in Carbonate Systems, *Chem. Rev.* **2008**, *108*, 4433.

(110) Meldrum, F. C.; Colfen, H., Controlling Mineral Morphologies and Structures in Biological and Synthetic Systems, *Chem. Rev.* **2008**, *108*, 4332.

(111) Sommerdijk, N.; de With, G., Biomimetic Caco3 Mineralization Using Designer Molecules and Interfaces, *Chem. Rev.* **2008**, *108*, 4499.

(112) Wang, C.-K.; Wang, C.-Z.; Wang, J.-C.; Hung, C.-C.; Li, W.-Y.; Chen, W.-C., Preparation and Characterization of Calcium Phosphate Deposited on Gold Nanoparticles, *J. Non-Cryst. Solids* **2010**, *356*, 927.

(113) Aryal, S.; Bahadur K. C, R.; Bhattarai, S. R.; Prabu, P.; Kim, H. Y., Immobilization of Collagen on Gold Nanoparticles: Preparation, Characterization, and Hydroxyapatite Growth, *J. Mater. Chem.* **2006**, *16*, 4642.

(114) Leff, D. V.; Brandt, L.; Heath, J. R., Synthesis and Characterization of Hydrophobic, Organically-Soluble Gold Nanocrystals Functionalized with Primary Amines, *Langmuir* **1996**, *12*, 4723.

(115) Daniel, M. C.; Astruc, D., Gold Nanoparticles: Assembly, Supramolecular Chemistry, Quantum-Size-Related Properties, and Applications toward Biology, Catalysis, and Nanotechnology, *Chem. Rev.* **2004**, *104*, 293.

(116) Love, J. C.; Estroff, L. A.; Kriebel, J. K.; Nuzzo, R. G.; Whitesides, G. M., Self-Assembled Monolayers of Thiolates on Metals as a Form of Nanotechnology, *Chem. Rev.* **2005**, *105*, 1103.

(117) Lahiri, J.; Isaacs, L.; Tien, J.; Whitesides, G. M., A Strategy for the Generation of Surfaces Presenting Ligands for Studies of Binding Based on an Active Ester as a Common Reactive Intermediate: A Surface Plasmon Resonance Study, *Anal. Chem.* **1999**, *71*, 777.

(118) Schlenoff, J. B.; Li, M.; Ly, H., Stability and Self-Exchange in Alkanethiol Monolayers, *J. Am. Chem. Soc.* **1995**, *117*, 12528.

Chapter 2:

FUNCTIONALIZED POROUS SILICON SURFACES TO DIRECT CALCIUM PHOSPHATE MINERALIZATION

2.1 ABSTRACT

Development of materials for the repair of mineralized tissues and interfaces relies on controlling crystal nucleation and growth at surfaces. One method for controlling the nucleation of crystals *in vitro* is by using surfaces functionalized with monolayers on silicon. A series of experimental models with 'nucleating' surfaces (functionalized porous silicon (pSi) surfaces) were assayed for solution growth of hydroxyapatite (HA). Surface chemistries, as confirmed via infrared spectroscopy, include methyl, carboxylate, and oxide, as well as attachment of additional molecules such as 2-aminoethyl dihydrogen phosphate (ADP) and 1-(3-aminopropyl)imidazole via N-hydroxysuccinimide/1-ethyl-3-[3-dimethylaminopropyl]carbodiimide hydrochloride (NHS/EDC) coupling chemistry. NHS/EDC chemistry was also used to covalently-link the proteins osteopontin (OPN) and bovine serum albumin (BSA) to the pSi surface. Hydroxyapatite formation on the functionalized pSi surfaces was confirmed by 2-D XRD while nucleation density and crystal morphology were analyzed via scanning electron microscopy (SEM). This work introduces three methods and time frames for studying the growth of HA on pSi surfaces: 1) Tris buffered solutions from 18 hrs to 7 days; 2) titration-controlled solutions with pH 7.3 end point at 110 – 600 minutes; 3) static pH solutions at pre-solution nucleation times

less than 110 minutes. Surfaces from the Tris-buffered system proved to be the least reproducible with the Tris buffer causing a delay in bulk solution precipitation as well as inconsistent surface morphologies among experiments. The titration-controlled system regulates the temperature as well as addition of calcium and phosphate solutions in a 5:3 molar ratio based on a set-point pH without the use of solution buffers. Nucleation density of HA varied as a function of surface chemistry on the pSi surfaces but surface morphologies were similar among all surface chemistries. Analysis of the titration and pH curves did not provide consistent trends in nucleation, induction, or pH decrease times. Finally, the static pH solutions were used to monitor mineral formation before bulk nucleation and decrease in solution pH. At 100 minutes (no visible nucleation), the static pH system demonstrated morphology differences on surfaces as a result of surface chemistry with amorphous-, needle-, and rosette-like morphologies on the methyl, carboxylate, and ADP surfaces, respectively. All other tested surfaces had little to no mineralization. This series of experiments demonstrates that tailoring the individual surface chemistries *in vitro* can provide clues to the nucleation and growth of HA at interfaces in biomineralized structures.

2.2 INTRODUCTION

Mineralized tissues, such as tooth and bone, have hierarchical structures consisting of nanoparticles of hydroxyapatite (HA) within an organic matrix. For example, tooth enamel has a defined, nucleating surface at which crystal growth is

initiated within a gel-like matrix.[1] Architecture of mammalian teeth involve interactions between the enamel – the outer most layer, dentin – the structural hydroxyapatite component, pulp – the nerve and blood vessel containing component, and the cementum – the mineralized tissue that resembles both bone and dentin surrounding the root serving as the connection for the periodontal ligament. Along all levels of the tooth hierarchy, the structure is an intricate network of highly organized hydroxyapatite crystallites within an inorganic matrix whose complex interfaces lead to specific structure functions. However, in many *in vitro* models of hydroxyapatite mineralization, nucleation is not controlled at interfaces.[1-8]

Porous silicon (pSi) is an ideal 'nucleating' substrate because it can be covalently functionalized via hydrosilylation, which reacts a primary alkene with a freshly hydrogen terminated silicon surface.[9] In addition, passivated and functionalized pSi can withstand pH, thermal, and solution ionic strength variations.[9,10] making them ideal candidates to introduce covalently bound surface chemistry (i.e., nucleating substrates) in mineralization assays. pSi substrates are preferred over their bulk counterparts because they have a larger surface area exposing reactive silicon facets for functionalization as well as being easier to analyze via infrared spectroscopy due to the increased surface area.[9,11] A complete discussion of the use of silicon substrates used for *in vitro* models of calcium phosphate mineralization can be found in Chapter 1, Section 1.4.

2.2.1 Experimental Design

For all experiments, pSi substrates were made using electrochemical etching techniques[11] followed by functionalization via thermal oxidation, hydrosilylation, or coupling chemistry (Figure 2.1). The surface chemistry was chosen based on the implications within biological systems – oxide chemistry as a control, methyl, and carboxylate to model proteins with a high number of amino acids with hydrophobic groups (e.g. leucine) and hydrophilic groups (e.g. glutamic and aspartic acid), respectively, and coupling chemistry to attach more biologically relevant materials to the surface (osteopontin (OPN), bovine serum albumin (BSA), and 2-aminoethyl dihydrogen phosphate (ADP)). BSA is a standard control protein[12] while OPN's phosphorylation state has been shown to affect HA formation.[13-15] ADP results in a high density of terminal phosphate groups on the surface. This subset of surface chemistries can provide clues towards directing mineral nucleation and growth at surface interfaces and within organic matrices.

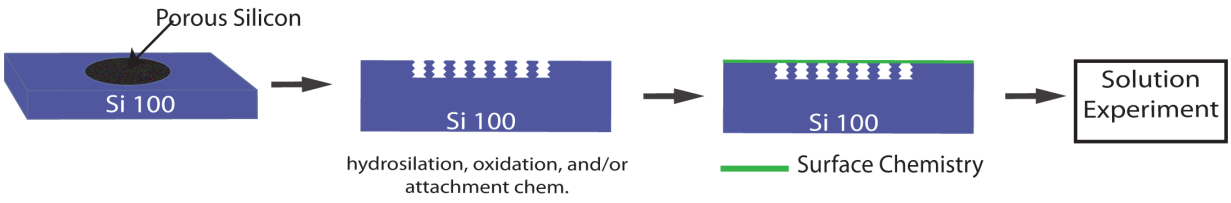

Figure 2.1: Experimental design schematic using functionalized pSi substrates as 'nucleating' surfaces for calcium phosphate mineralization in three solution-based crystallization experiments.

Functionalized pSi surfaces were then introduced into the solution-based assays (Figure 2.1). In this study, we chose to use three solution-based systems with different time spans to assay calcium phosphate mineralization on pSi surfaces: 1) Tris-buffered solutions (18 hrs to 7 days); 2) titration-controlled solutions with a pH 7.3 end point (110 – 600 minutes); 3) static pH solutions at pre-solution nucleation times (< 110 minutes). Tris-buffered systems provide a straightforward way of maintaining physiological pH (7.4) while also introducing ions such as calcium and phosphate without external dosing or monitoring equipment. Separate solutions of calcium and phosphate prepared in pH balanced (7.4) Tris buffer solutions are mixed in a 5:3 mM molar ratio, respectively, to create the reaction solution. Surfaces in a buffered system are suspended for a defined period of time and then removed for analysis.

Nancollas and co-workers have extensively characterized constant composition and titration based systems for calcium phosphate,[7,8,16-18] calcium oxalate,[19,20] and calcium carbonate[21] crystal growth. The Nancollas constant composition system actively controls the temperature, atmosphere, and solution compositions during the mineralization reaction while monitoring the pH as well as calcium and phosphate concentrations.[17] Ionic strength, calcium concentration, phosphate concentration, and pH was maintained using titration solutions whose concentrations were calculated using mass balance equations.[17,18] Titrant addition for the constant composition system was determined based on changes in calcium concentration. The system contained two titrators, one with calcium and a salt to maintain calcium concentration

and ionic strength, respectively, and a second with phosphate and a base to maintain phosphate concentration and pH, respectively.

The same general principles of the constant composition system apply to a titration-based pH stat system when introducing chemistries, proteins, or substrates that could affect the measured calcium concentrations.[7,8] The titration-based system controls titrant addition as a function of pH changes rather than calcium concentration, hence calcium concentrations may vary. Analysis of the titration and pH curves provide insight into the effect of solution additives (i.e. surfaces, seed mineral, proteins) on the nucleation of calcium phosphate.

A static pH system uses a similar setup to the titration-controlled system except that the titration equipment used to maintain solution composition and pH are absent. No solution nucleation happens during the reaction time and pH remains at or above the pH 7.4 set point. The key advantages to the titration-controlled and static systems are that they control and/or monitor solution concentration, pH, temperature, and atmosphere while removing buffers from the system. The combination of controlled mineralization and nucleating substrates (functionalized pSi) demonstrates that tailoring the individual surface chemistries *in vitro* can provide clues to the nucleation and growth of HA mineralization at surface interfaces in biomineralized structures.

2.3 RESULTS AND DISCUSSION

2.3.1 Porous Silicon (pSi) Surface Chemistry

Six pSi surface chemistries - oxide, methyl, carboxylate, 2-aminoethyl dihydrogen phosphate (ADP), osteopontin (OPN), and bovine serum albumin (BSA) – were examined during mineralization studies as were three proof-of-concept/quenching chemistries – NHS/EDC coupling chemistry, 1-(3-Aminopropyl)Imidazole (IMD), and hydroxylamine. General routes to pSi surface functionalization are shown in Schemes 2.1-2.4.

Oxide functionality was achieved by removing the native oxide layer from a pSi sample using hydrofluoric acid to achieve a hydrogen terminated silicon surface (Scheme 2.1). The freshly hydrogen terminated surfaces were then placed in a Parr bomb under heating and 100% humidity to form a thermal oxide (i.e., passivation layer) that can withstand the ionic, aqueous conditions of mineralization experiments.[22] Surface oxidation was confirmed via infrared spectroscopy (Figure 2.2).

Scheme 2.1: Thermal oxidation of pSi substrates.

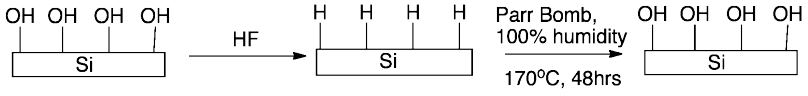

Hydrosilylation chemistry provided a chemical route to covalently attaching primary alkenes to the silicon surface (Scheme 2.2).[9,23,24] Primary alkenes (1-dodecene and 10-undecanoic acid) and freshly hydrogen-terminated pSi surfaces were reacted under air- and water-free conditions with heating. The alkene reacts with the Si-H bonds on the surface to form a silicon-carbon linkage with the surface. The functionality of the terminal-end, opposite the primary alkene has to be chosen carefully so as not to preferentially react with the Si-H bonds rather than with the alkene. Terminal methyl and carboxylate groups were confirmed via infrared spectroscopy (Figure 2.2). Successful coupling reactions provide further evidence that the carboxylate groups are terminal and not reacted with the silicon surface (Figures 2.3 and 2.4).

Scheme 2.2: Hydrosilylation chemistry of pSi substrates resulting in methyl and carboxylate chemistries.

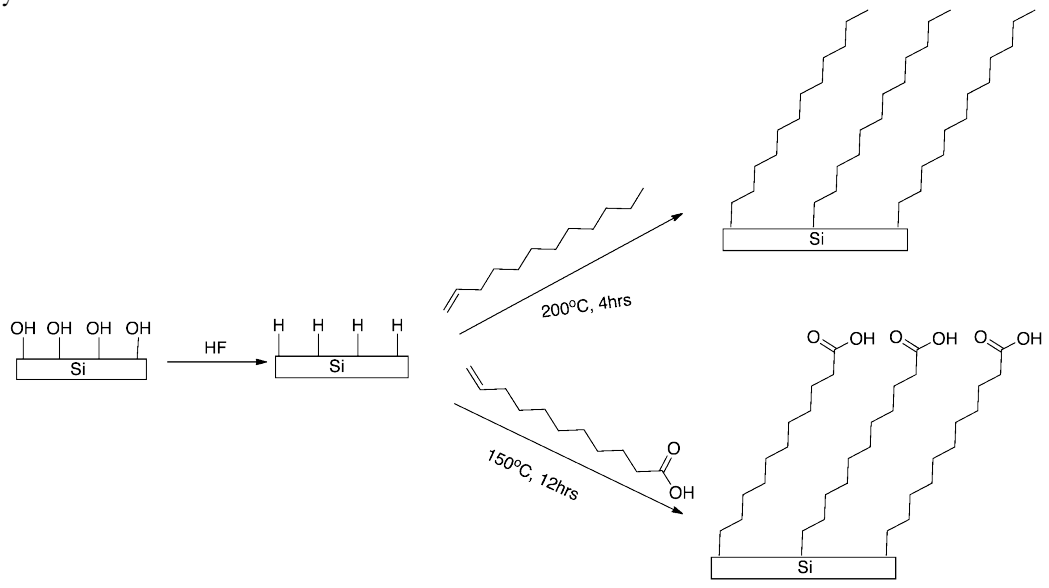

Amine coupling to carboxylate surfaces functionalized via hydrosilylation was carried out using N-hydroxysuccinimide/1-Ethyl-3-[3-dimethylaminopropyl]carbodiimide hydrochloride (NHS/EDC) coupling chemistry (Scheme 2.3).[25-27] A reaction solution containing equal amounts of 0.1 M NHS and 0.4 M EDC was used to activate the carboxylic acid group of pSi surface for amide bond formation. The NHS is then displaced by a reaction with a primary amine (NH_2-R) creating an amide linkage between the original carboxylic acid and the coupled amine. For successful coupling of the primary amine, the amine solution (neat or aqueous) had a pH greater than 8. Successful amine coupling was confirmed via IR spectroscopy by the presence of amide peaks (Figure 2.3, Table 2.1). Coupling chemistry was proven to be effective by first using 1-(3-aminopropyl)imidazole (IMD) and monitoring appearance as well shifts in amide peaks (~1700-1400 cm^{-1}). IMD was not used in any further mineralization studies.

Scheme 2.3: Coupling chemistry reaction schematic for small NH_2-R compounds.

EDC: 1-Ethyl-3-[3-dimethylaminopropyl]carbodiimide hydrochloride
NHS: N-hydroxysuccinimide

NH_2-R:	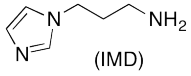 (IMD)	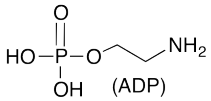 (ADP)
Reaction Conditions	Neat, 4 hrs Room Temp	0.5 M in BBS, pH 9.5 4 hrs, Room Temp

Coupling of proteins to the surface was achieved using the same principles as the coupling of small molecules (Scheme 2.4).[25,26,28] Borax buffered solution (BBS; pH 8.5), a non-phosphate or amine containing buffer, was used to dissolve osteopontin (OPN) and bovine serum albumin (BSA) at a concentration of 20 μg/mL.[28] The primary amines in the OPN and BSA reacted with the NHS on the surface to created covalent amide linkages with the silicon surface. Hydroxylamine was used to quench any unreacted surface NHS on the surface after protein attachment. A pH greater than 8.0 of the coupling solution proved to be crucial for the OPN, BSA, and ADP reactions as well as avoiding proteins buffered in tris or phosphate buffered saline (PBS) to prevent introduction of reactive amine groups and additional phosphate,

respectively.[28] Successful protein coupling with the pSi surface was confirmed via IR spectroscopy by the presence of amide peaks characteristic of proteins (Figure 2.4, Table 2.1).

Scheme 2.4: Coupling chemistry reaction schematic of proteins (NH_2-R) using hydroxylamine to quench unreacted EDC.

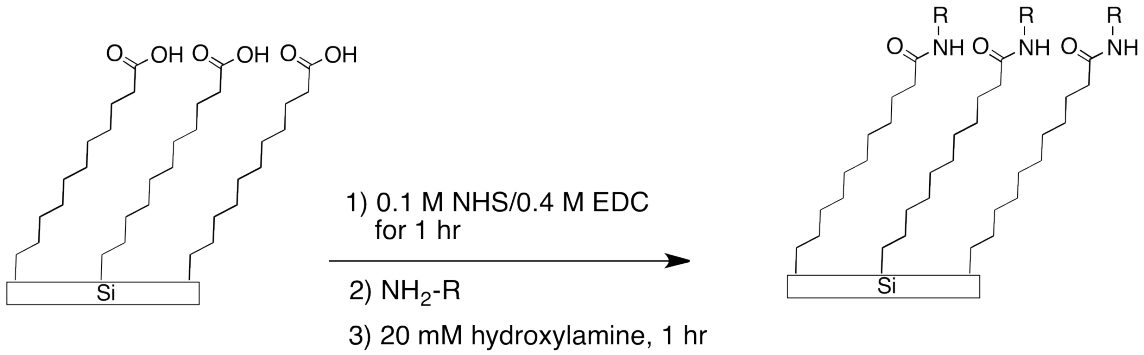

EDC: 1-Ethyl-3-[3-dimethylaminopropyl]carbodiimide hydrochloride
NHS: N-hydroxysuccinimide

NH_2-R:	Bovine Serum Albumin **(BSA)**	Ostepontin **(OPN)**
Reaction Conditions:	20 μg/mL in BBS (Borax Buffered Solution), pH 8.5 12 hrs, 4˚C	

Compiled FTIR peak positions for the amide region of the carboxylate, ADP, IMD, hydroxylamine, BSA, and OPN surface chemistries are displayed in Table 2.1. Literature values for random coil, β-sheet, α-helix, and denatured proteins in addition to experimental values for adsorbed proteins on functionalized gold surfaces are presented for comparison. [29,30,31,32] The peak around 1709 cm^{-1} is the unreacted carboxylate from the original substrate. Peaks from ~1600-1700 cm^{-1} and ~1500-1600

cm^{-1} are Amide I and II peaks, respectively, that are indicative of the protein conformation. The small amount of silicon oxide on all surface chemistries prevented further analysis of the calcium phosphate mineral on the surface via GeATR due to the overlap of the oxide and phosphate peaks at ~1100cm^{-1}.

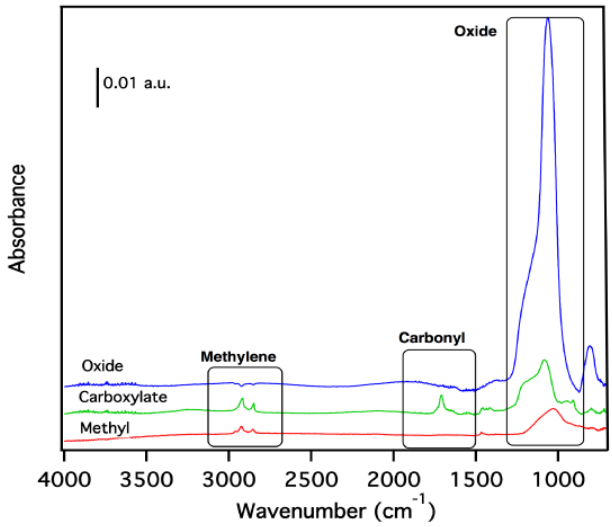

Figure 2.2: GeATR spectra of silicon surface chemistry before mineralization. Expected peaks for methylene at ~2900 cm^{-1}, carboxylate at ~1700 cm^{-1}, and oxide at ~1100 cm^{-1} are consistent with literature spectra.[9,22-24,27,33]

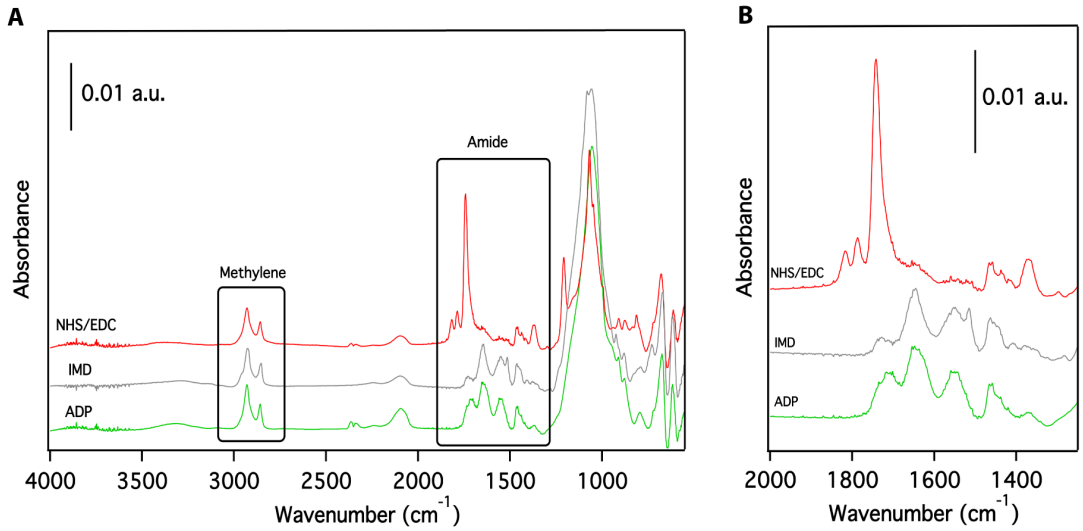

Figure 2.3: GeATR spectra of silicon surface chemistry (A) before mineralization. Expected peaks for amide bond formation at ~1500-1700 cm^{-1}, are present, indicating successful amine coupling (B). [25-27] The oxide peaks at ~1100 cm^{-1} indicate a small amount of oxidation of the underlying pSi substrate.

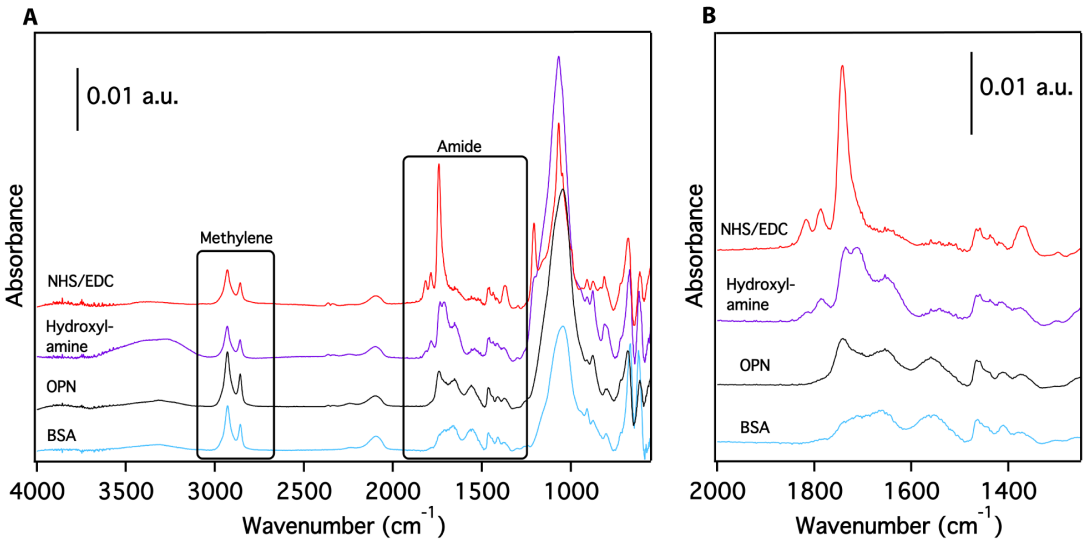

Figure 2.4: GeATR spectra of silicon surface chemistry (A) before mineralization. Expected peaks for amide bond formation with proteins at ~1500-1700 cm^{-1} are present, indicating successful amine coupling (B).[12,27] The oxide peaks at ~1100 cm^{-1} indicate a small amount of oxidation of the underlying pSi substrate.

Table 2.1: Amide IR peak positions (cm^{-1}) from GeATR spectra of small molecules and proteins on porous silicon surfaces compared to adsorbed protein peak positions on functionalized gold surfaces. Literatures values presented for comparison.

pSi Surface Chemistry	**Amide I (cm^{-1})**	**Amide II (cm^{-1})**
Carboxylate	1709	
NHS/EDC	1816,1786, 1741	
IMD	1722, 1647	1548, 1515
ADP	1709, 1643	1550
Hydroxylamine	1824, 1785, 1734, 1712, 1652	1539
OPN	1739, 1656	1556
BSA	1705, 1663	1557
Adsorbed Proteins on Gold Surfaces[a]		
BSA (α-helix)	1670	1543
Silk Fibroin (Random Coil)	1673	1542
Silk Fibroin (β-sheet)	1667	1542
Literature Values		
Random Coil[b]	1648-1644	
β-sheet[b]	1632-1621	
α-helix[b]	1655-1650	
Denatured[c]	1671	
BSA (α-helix)[d]	1653	1538

[a] Protein adsorbed on carboxylate functionalized gold surfaces (Chapter 4).
[b] Miyazawa, et al., *J. Am. Chem. Soc.* **1961**, *83*, 712.
[c] Cerda-Costa, et al., *Biochemistry* **2009**, *48*, 10582.
[d] Mielczarski, et al., *J. Phys. Chem. B* **2008,** 112, 5228-5237.

2.3.2 Mineralization Using Tris Buffered Solutions

Mineralization in buffered solutions was carried out on oxide, methyl, and carboxylate pSi surfaces. An example pSi surface and a mineralized sample cross section are shown in Figure 2.5. Surfaces were suspended upside down to prevent gravitational mineralization, which occurs when calcium phosphate nucleates in solution and then deposits on the surface. By suspending upside down, the observed surface calcium phosphate is nucleating on the surface rather than in solution.

Reaction solutions contain 5 mM calcium (Ca) and 3 mM phosphate (Pi) in 0.15 M tris buffered at pH 7.4. Reactions were run at both room temperature and 37˚C for 18 hrs, 24 hrs, 3 days, and 7 days. A larger amount of mineral was present on surfaces placed in the bottom of a petri dish face up versus pSi surfaces suspended upside down in control experiments (Figure 2.6). Preliminary experiments at 2.5:1.5 mM Ca:Pi showed little to no mineralization after 7 days thus were not further explored. Results presented herein for Tris experiments are for 7 day experiments at 5:3 mM Ca:Pi, unless otherwise noted. Noticeable solution precipitation was observed in all solutions at 1.5 days without appreciable change in pH (7.40 ± 0.05). Mineral morphology and density for time periods shorter than 7 days proved to be irreproducible.

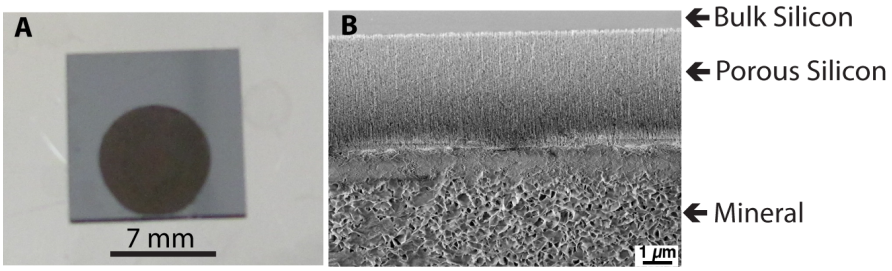

Figure 2.5: Picture of a porous silicon (pSi) sample used in experiments (A), the dark area is pSi while the shiny portion is bulk silicon, and FE-SEM cross section of a mineralize pSi sample (B) showing the bulk silicon, pSi, and mineral.

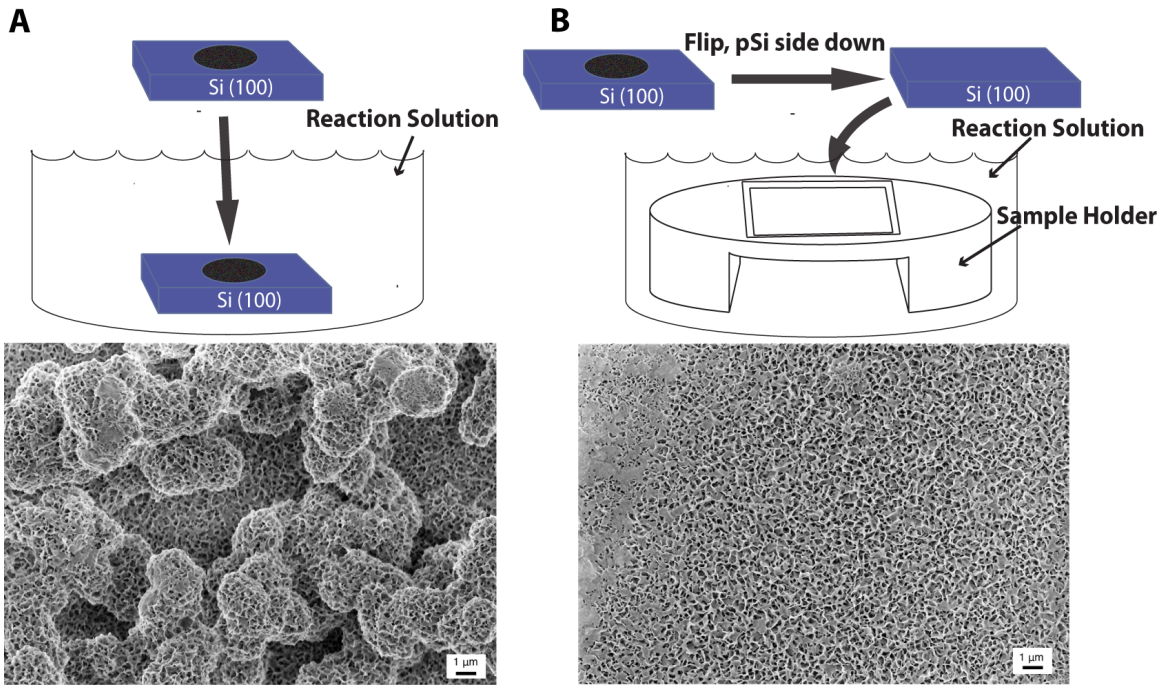

Figure 2.6: Control experiment FE-SEM images and geometries of hydroxyapatite mineralization in the face up/gravitational (A) and suspended (B) geometries under identical mineralization conditions.

Carboxylate surfaces resulted in the most varied morphology ranging from needle-, plate-, to rosette-like depending upon the location on the surface, pSi center, pSi edge, and bulk, respectively (Figure 2.7). Comparing the pSi region across the oxide, methyl, and carboxylate functionalities at room temperature demonstrated rosette-like morphology for both the oxide and methyl surfaces while the carboxylate had predominately needle-like morphology (Figure 2.8). The morphology varied significantly at 37˚C when compared to the room temperature morphology. However, the morphology differences are most likely not due to just temperature differences but also the decrease in buffering capacity of the Tris buffer at 37˚C.[34]

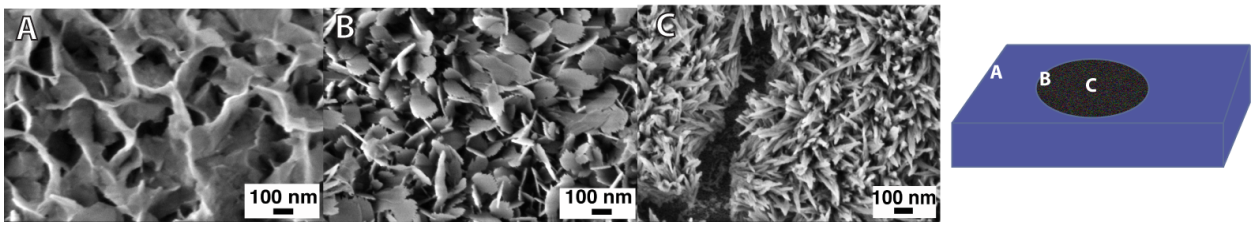

Figure 2.7: FE-SEM images of three locations on the carboxylate functionalized silicon surface. The images represent the hydroxyapatite mineral formation on the bulk (A), pSi edge (B), and pSi (C) middle respectively.

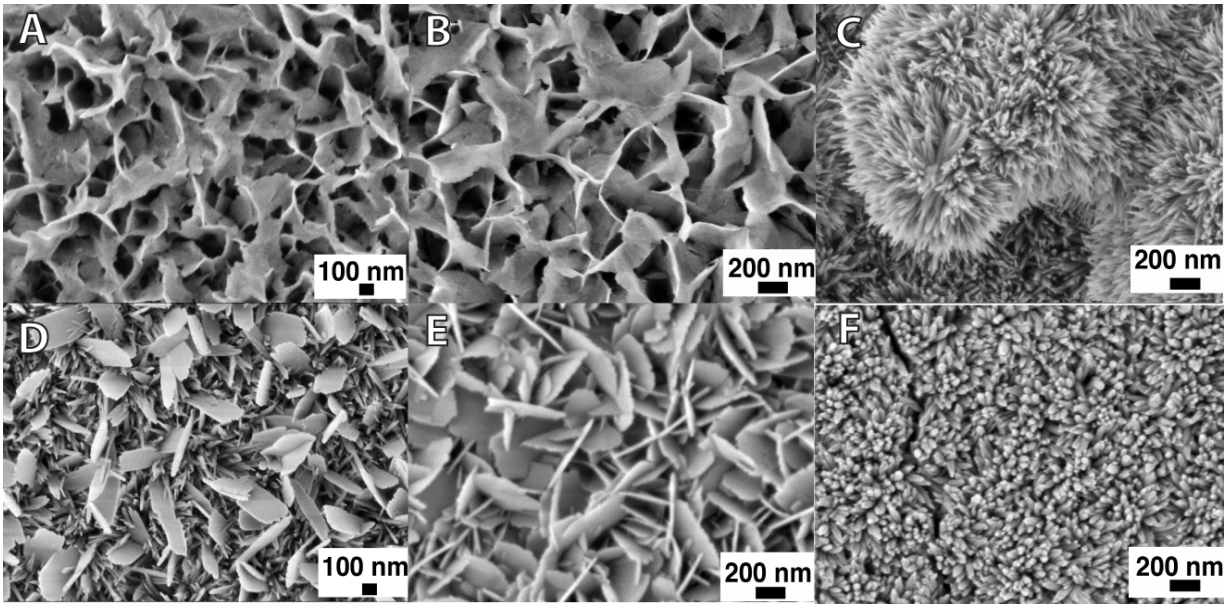

Figure 2.8: FE-SEM images of the oxide (A, D), methyl (B, E), and carboxylate (C, D) pSi surfaces at room temperature (A-C) and 37˚C (D-F). Differences in morphology were a result of surface chemistry as well as temperature.

The mineral on all surfaces was confirmed to be HA via 2-D x-ray diffraction (Figure 2.9). The presence or lack of bright spots along circular reflections demonstrates HA orientation on the surface (Figure 2.10A). Distinctive bright spots indicate orientation along the reflections crystal plane while a consistent brightness along the entire reflection circumference indicates polycrystalline material. Possible

mineral orientation along the HA (002) axis was observed on some of the carboxylate surfaces as evident by variations in ring intensity around the (002) reflection. Polycrystalline mineral, as indicated by continuous, uniform rings, was observed for both the methyl and oxide surfaces. Movement of the reflections bright spots corresponding to a change in the sample tilt angle (90˚ vs. 54˚), confirms that brightness in reflections are from crystal orientation not detector effects (Figure 2.10B and C).

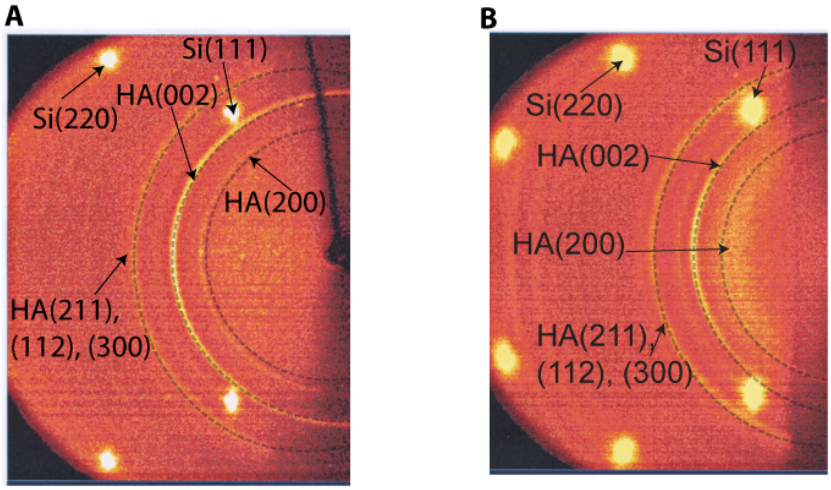

Figure 2.9: Representative 2D x-ray pattern of a methyl (A) and carboxylate (B) surface after 7-days in a 5:3 Ca:Pi tris buffered solution at room temperature. The hydroxyapatite, as well as the underlying silicon surface, reflections are labeled. Dotted lines added to aid in visualization.

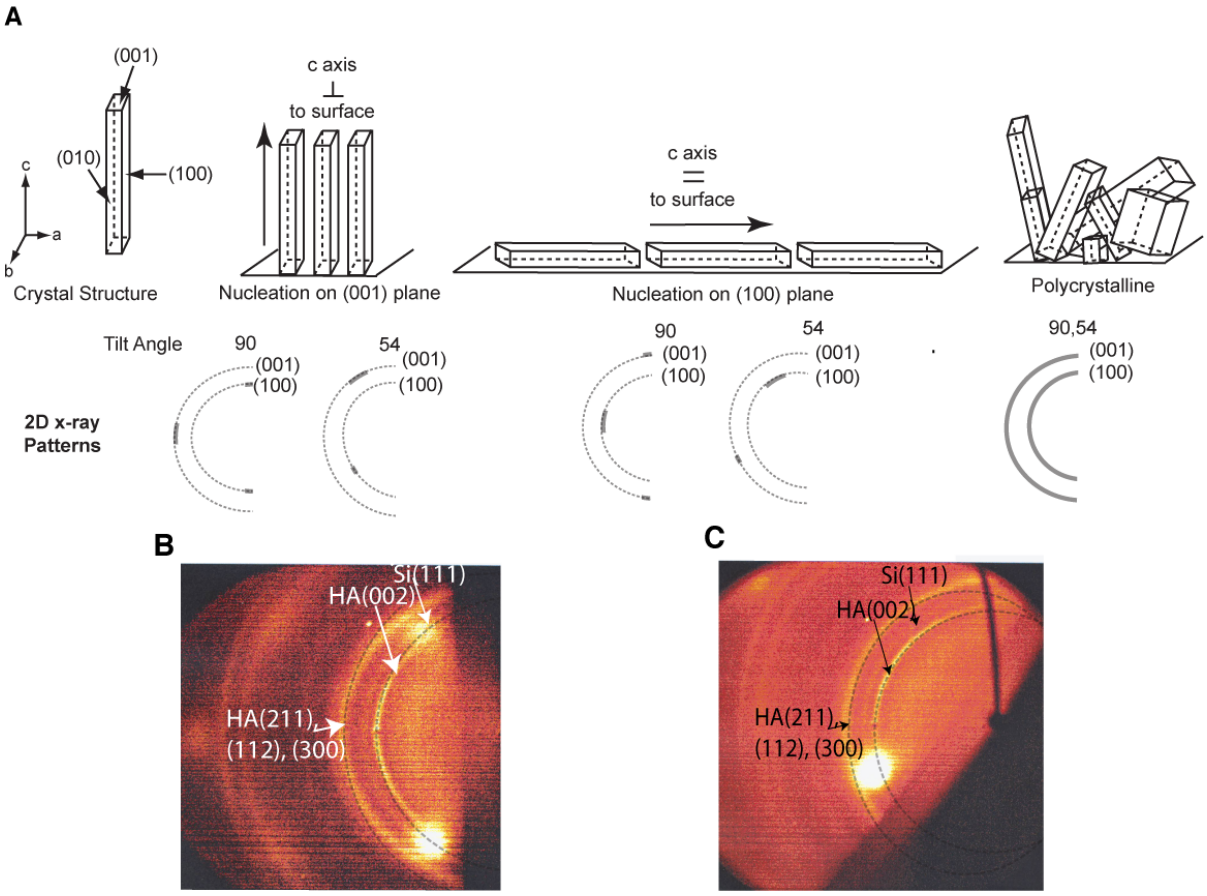

Figure 2.10: 2D x-ray schematic. A) Representation of hydroxyapatite orientations on a surface and corresponding 2-D x-ray patterns of sample tilt angles of 90˚ and 54˚ shown below crystal orientations. Bright spots or lack thereof indicate the orientation and crystallinity of the hydroxyapatite. Carboxylate surface 2D x-ray pattern at 90˚ tilt angle (B) and 54˚ tilt angle (C) show the movement of the bright spot along the HA (002) reflection with tilt angle indicating mineral orientation.

The Tris-buffered mineralization experiments demonstrated trends but were not reproducible among experiments, especially at the shorter reaction times. Fluctuations in room temperature and humidity (i.e., winter vs. summer experiments), appeared to have the most affect on reaction reproducibility. The lack of bulk solution mineralization until 1.5 days at these concentrations (5:3 mM Ca:Pi) show that the

Tris buffer was affecting the bulk solution nucleation. Solutions not containing buffer at these concentrations form visible precipitate almost immediately upon mixing. The Tris-buffered experiments did however demonstrate that the three chosen chemistries (oxide, methyl, and carboxylate) on pSi surfaces would potentially provide clues to calcium phosphate mineralization at interfaces under more controlled reaction conditions.

2.3.3 Mineralization on Surfaces Using Titration-Controlled Solutions

A dual constant composition system developed by Nancollas and co workers[7,8,16-21] allows for more control of solution composition without the use of buffers as well as tighter regulation of temperature, pH, and atmosphere. I modified a system available in the Boskey lab at the Hospital for Special Surgery to use changes in pH to control the addition of calcium (Eqn. 2.1 and 2.2) and phosphate (Eqn. 2.3 and 2.4) titrant solutions. The calcium (Ca) solution also contains sodium chloride to maintain a 0.15 M ionic strength while the phosphate (Pi) contains sodium hydroxide to maintain pH. Starting salts were chosen to minimize the types of counter ions available in solution (i.e. only Na^+ and Cl^-). Equations 2.1-2.6 result from mass balance calculations for hydroxyapatite. *T* is defined as the titrant concentration, while *W* is the reaction concentration.[17,18]

$$T_{CaCl_2} = 2W_{CaCl_2} + 5C_{eff} \quad \text{(Eqn. 2.1)}$$

$$T_{NaCl} = 2W_{NaCl} - 10C_{eff} \quad \text{(Eqn. 2.2)}$$

$$T_{NaH_2PO_4} = 2W_{NaH_2PO_4} + 3C_{eff} \quad \text{(Eqn. 2.3)}$$

$$T_{NaOH} = 2W_{NaOH} + 7C_{eff} \quad \text{(Eqn. 2.4)}$$

$$C_{eff} = {}^{W_{CaCl_2}}/_{10} \quad \text{(Eqn. 2.5)}$$

$$W_{NaOH} = W_{NaH_2PO_4} - C_{eff} \text{ (Eqn. 2.6)}$$

Attempts were made to use the calcium electrode to control titrant addition. However, the calcium values were not consistent with standards or calibration curves due the phosphate in our reaction setup as the electrode is based on potential differences across a phosphate impregnated polymer membrane.[35]

Reaction conditions were maintained at 3.0 mM Ca, 1.80 mM Pi, 0.15 M total ionic strength, and pH 7.4 to emulate physiological conditions. Two functionalized pSi surfaces were used for each run except for sample holder controls. The system was stopped at pH ~7.3 when the titrators could no longer keep up with the amount of nucleation happening in solution (Figure 2.11A).

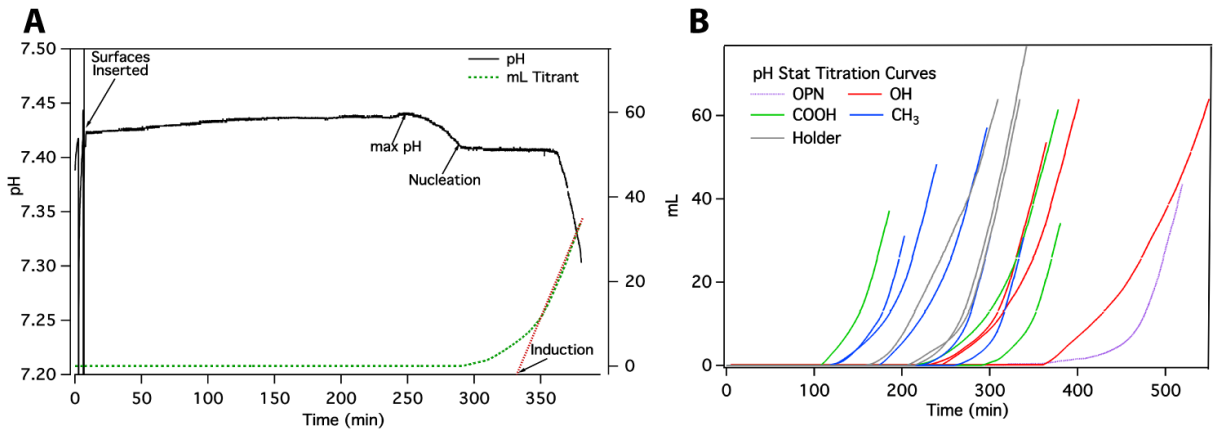

Figure 2.11: Representative plot (A) of mL of titration vs. pH and compiled titration data (B) for titration controlled mineralization experiments for all functionalized pSi surfaces and sample holder.

Analysis of the titration data, including nucleation time, induction time, pH decrease, and their differences did not show any clear trends as a function of surface chemistry (Figure 2.11B, Table 2.1). The parameters are defined as the time when addition of titrant starts (nucleation), a tangent to the steepest part of the slope crossed the x-axis (induction), the pH starts to decrease after reaching a maximum (pH decrease), and difference between nucleation and pH decrease (SpH), respectively. The standard deviations in the averaged data overlapped and indicated that any differences among surfaces were not statistically significant. The differences in nucleation, induction, and pH decrease, had standard deviations close to half the average value for several surface chemistries.

Table 2.2: Compiled data from titration controlled calcium phosphate mineralization experiments.

pSi Surface[f] Chemistry	Nucleation[a] (min)	Std. Dev.	Induction[b] (min)	Std. Dev.	Induction - Nucleation (min)	Std. Dev.	pH[c] ↓	Std. Dev.	SpH[d]	Std. Dev.
Oxide (*n=3*)	279.5	75.4	360.2	82.4	80.6	7.0	237.7	66.4	41.9	17.2
Carboxylate (*n=3*)	203.7	92.1	258.3	102.9	54.65	25.7	153.3	99.5	50.4	13.0
Methyl (*n=5*)	176.7	62.3	228.6	58.2	52.0	6.1	115.2	55.1	61.5	29.1
Osteopontin[e] (OPN) (*n=1*)	315.5	-	469.1	-	153.7	-	276	-	39.5	-
Sample Holder (*n=3*)	191.2	30.7	257.0	35.8	65.8	6.5	164.3	41.9	26.9	11.8

a *Nucleation :* The time when addition of titrant starts.
b *Induction* The point at which a tangent to the steepest part of the slope crossed the x-axis.
c *pH decrease:* The time point where the pH started to decrease after reaching a maximum.
d *SpH:* The difference between nucleation and pH decrease.

Surface morphology, as observed by SEM, across all four surface chemistries demonstrated similar morphology (Figure 2.12). Differences in the mineral density, OPN > carboxylate > oxide > methyl, were observed on the pSi region of the sample. 2-D x-ray analysis of all surfaces confirmed hydroxyapatite formation (Figure 2.13). Although the results of this setup were much more consistent, similar mineral morphology among surface chemistries was unexpected, especially considering the trends observed in the Tris buffered system. However, in looking at the reaction setup, the pSi surfaces, two 1 cm^2 pieces, comprise a relatively small amount of the nucleating surfaces (~5%). The reaction vessel, electrode, sample holder, and titration ports present a greater surface area for calcium phosphate mineral nucleation. Therefore, it is likely that nucleation on the pSi surfaces is happening prior to significant changes in pH or around the nucleation time point of the system, before

other surfaces dominate mineral nucleation. Based on this data, we moved to using a static pH system with a reaction time just below that of the fastest nucleation time (110 minutes for a carboxylate run). It was hoped that by removing the surfaces before bulk nucleation began, differences among the surfaces would be observed.

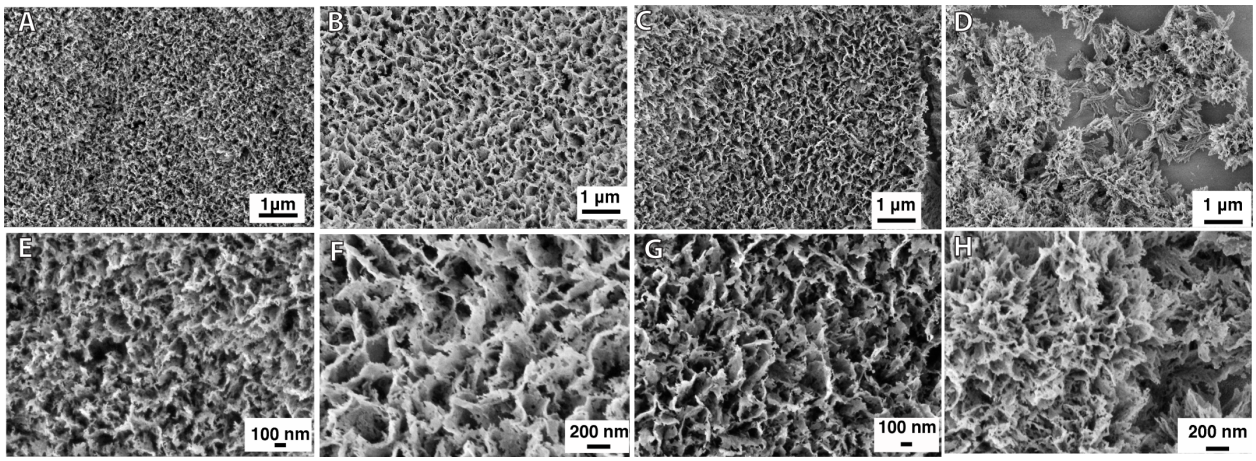

Figure 2.12: Representative FE-SEM images of OPN (A, E), carboxylate (B, F), oxide (C, G), and methyl (D, H) surfaces from the titration controlled experiments removed at pH ~7.3. pH 7.3 corresponded to 110 to 600 minutes. All surfaces have similar mineral morphology while differences in surface coverage (OPN>carboxylate>oxide>methyl) were observed.

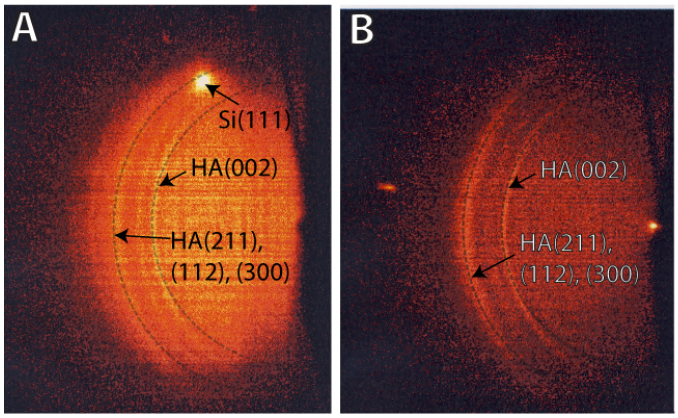

Figure 2.13: Representative 2-D x-ray pattern of a carboxylate (A) and OPN (B) surfaces after titration controlled experiments stopped at pH ~7.3. The hydroxyapatite, as well as the underlying silicon surface, reflections are labeled. Dotted lines added to aid in visualization.

2.3.4 Mineralization under Static pH Conditions

Static pH conditions are similar in principle to those of the titration-controlled system except the reaction is stopped prior to bulk nucleation (i.e. no solution nucleation, pH at or above set point of 7.4), negating the need for the addition of titrant. The shortest nucleation point from the titration-controlled assay was at 110 minutes, thus a reaction time of 100 minutes was chosen for this study. Prior to introduction into mineralization solutions, surfaces were incubated under two different conditions: 0.4 M $CaCl_2$, pH 6.5 and 0.4 M $CaCl_2$, pH 9.5, to account for possible differences in surface acidity.[36]

Consistent morphology and surface coverage were observed for each surface chemistry over at least three separate runs on different days (Figure 2.14). The pSi region of the oxide surfaces had no surface mineralization while the methyl,

carboxylate, and ADP functionalized surfaces resulted in mineral morphologies with amorphous-, needle-, and rosette-like morphology, respectively. The OPN and BSA showed sporadic mineralization across the pSi region (Figure 2.15).

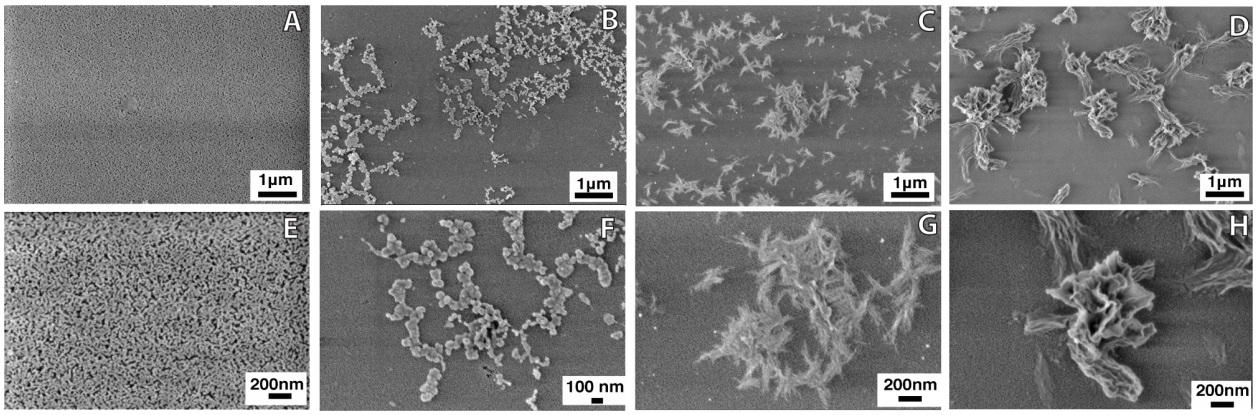

Figure 2.14: Representative FE-SEM images of the static mineralization assay at 100-minute reaction times of oxide (A, E), methyl (B, F), carboxylate (C, G), and ADP (D, H) pSi surface chemistries. The mineral morphology varies from none, amorphous, needle-like, and rosette for the oxide, methyl, carboxylate, and ADP chemistries, respectively.

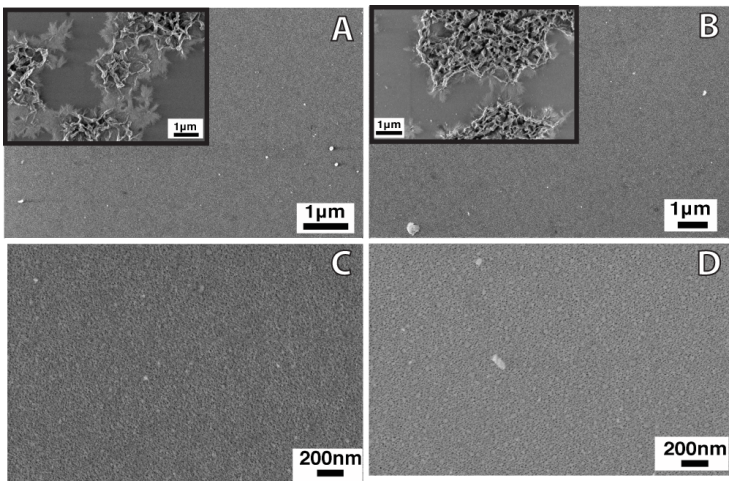

Figure 2.15: Representative FE-SEM images of the static mineralization assay at 100-minute reaction times of BSA(A, C) and OPN (B, D) pSi surface chemistries. The bulk of the pSi lacks mineral formation. Small areas of sporadic mineralization are show in the insets.

EDX analysis of the methyl and carboxylate surfaces indicate that both minerals are calcium phosphate with carboxylate surfaces having a Ca:Pi ratio of 1.75 ± 0.26 and methyl 1.57 ± 0.33 (Figure A2.2). The variability in these values is not surprising considering the relatively small amounts of material on the surface. 2-D x-ray results were unable to confirm hydroxyapatite formation due to the small amount of material on the surfaces as compared to both the tris buffered and titration controlled experiments.

The link between surface chemistry and calcium phosphate has been previously been difficult to pin-down, unlike calcium carbonate, a biomineral found in mollusk shells. Researchers studying calcium carbonate have been able to elucidate the effect that various surfaces and chemistries have on the specific morphology and phases of calcium carbonate.[36-39] The static pH assay results presented in this work are the first demonstration that the surface functionality directly influences calcium phosphate morphology. The methyl, carboxylate, and phosphate functional groups clearly show that surface chemistry has the potential to direct calcium phosphate mineral morphology and nucleation.

The ability to guide mineralization using surface chemistry also has application to understanding a protein's ability to inhibit, promote, and facility calcium phosphate mineralization in biological systems. The high density of phosphate groups on the ADP surface clearly have an effect on mineral nucleation and morphology, providing

further evidence that phosphorylation is important for directing mineral nucleation and morphology.[14,40] Interestingly, the phosphorylated version of OPN did not promote mineral nucleation in this system at this time point. The lack of mineral on the OPN surfaces at 100 minutes could be due to a difference in induction times. As seen in the titration data (Figure 2.11B and Table 2.2), the OPN surface had an induction time of 469.1 minutes as compared to the average induction times of 228.6 and 258.3 minutes for the methyl and carboxylate surfaces, respectively. Static pH experiments closer to the OPN induction time could possibly provide clues to OPN's function when covalently bound to a surface.

OPN is an inherently disordered protein while BSA has a α-helical conformation in solution. Possible conformational changes when bound to the surface could also be affecting the proteins ability to direct calcium phosphate mineralization. Chapter 4 describes a series of experiments physisorbing silk fibroin and BSA protein on functionalized gold surfaces. The Amide I and II peak positions were used to analyze the conformation of the physisorbed proteins. Physisorbed BSA had Amide I peak position of 1670 cm^{-1} on carboxylate surfaces while in the covalently bound protein presented here it is 1662 cm^{-1}, which is closer to the native α-helical position of 1653 cm^{-1}.[32] The peak positions indicate that the covalently bound proteins in this study has a conformation closer to native conformations than if physisorbed.

Previous studies of OPN nucleation have been done in solution- or gel-based systems.[13,14] Boskey and co-workers observed that while highly phosphorylated OPN promoted hydroxyapatite formation at concentrations less that 50 μg/mL, an inhibitory effect was observed at concentrations greater than 50 μg/mL in a gel-based system.[13] Covalent binding of the OPN protein to the pSi surface could be providing a localized concentration of protein. The covalent protein binding may also have an effect on conformational and/or chemical inhibitor effects not related to the protein phosphorylation dominating mineral formation. Recent work has also shown that different fragments of OPN, C-terminal, N-terminal, and SKK, have varying affects on HA mineral formation (Figure A2.1). The C- and N-terminal fragments behave similarly to full phosphorylated version of OPN while the SKK fragment inhibits HA formation.[41] In the current work, the sporadic mineralization sites are likely those where there is less protein on the surface or one of the few sites where protein conformation was such that promotion of mineral formation was observed. Mineralization may also be inhibited due to the covalent binding exposing a higher density of the SKK fragment to mineralization solutions. Further studies at longer static pH conditions for BSA and OPN, as well as smaller protein fragments, would assist in providing additional insight into the protein mineralization results observed in this study.

2.4 CONCLUSION

This *in vitro* model for calcium phosphate mineralization at surfaces clearly demonstrates that the surface chemistry can influence calcium phosphate nucleation, morphology, and density. Surface chemistries, such as oxide, methyl, and carboxylate, as well as more complex molecules and biologically relevant proteins chemistries were successfully bound to pSi surfaces using thermal oxidation, hydrosilylation, and coupling chemistries. Tris buffered solution mineralization proved to be the least reproducible while the additional control of the titration-controlled and static pH systems provided key insight into the effect of surface chemistry on mineralization. Although mineral morphologies among all surface chemistries in the titration-controlled system were similar, the titration data provided clues to the conditions at which the initial mineral is likely formed on the surfaces (i.e. static conditions less than 110 min). Static pH results indicated that simple chemistries (oxide, methyl and carboxylate) and phosphorylation play an important role in directing mineral formation at surface interfaces. Nucleating and non-nucleating chemistries within proteins and small molecules likely assist in directing the carefully orchestrated mineralization in biological systems. This study demonstrates that tailoring the individual surface chemistries, as well as, density and bound state of proteins *in vitro* can provide clues to the nucleation and growth of hydroxyapatite mineralization at surface interfaces in biomineralized structures.

2.5 MATERIALS AND METHODS

2.5.1 Silicon Surface Preparation

Highly doped (0.001-0.003 Ωcm) p-type silicon (100) wafers were purchased from Siltronix. Wafers were cut to 1 cm^2 pieces using the KS 7100 dicing saw at the Cornell NanoScale Science and Technology Facility (CNF). Porous silicon (pSi) surfaces were prepared using hydrofluoric acid (HF) electrochemical etching techniques.[11] *Caution*: 48-51% HF is toxic and OHSA safety protocols were followed. Briefly, 3:1 HF:ethanol solutions were prepared by mixing 180 mL of 48-51% HF (Baker Analyzed Reagent, ACS Grade, Circle of Safety) and 60 mL absolute ethanol (Pharmco) in plasticware. Seven silicon surfaces were placed in a custom-made Teflon etch assembly (Figure 2.16) with a spacer creating a 7 mm diameter circle exposed for etching. Surfaces were etched at 150 mA, 2 V for 5 minutes (7 surfaces) in the 3:1 HF:Ethanol solution, rinsed thoroughly with absolute ethanol, and dried with nitrogen. Surfaces were stored under ambient air conditions until ready for functionalization.

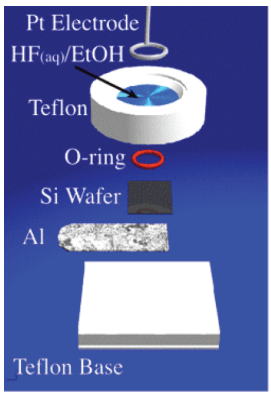

Figure 2.16: Schematic of porous silicon etch cell.[42]

2.5.2 Silicon Surface Chemistry

2.5.2.1 Thermal Oxidation

Oxide pSi surfaces were prepared by placing 5 porous silicon surfaces in a custom built slotted Teflon spacer in a Parr bomb (23 mL) with 3 drops of deionized (DI) water.[22] The Parr bomb Teflon vessel and spacer were cleaned prior to use by soaking for 1 hr in aqua regia, copious rinsing in DI water, and drying in 70°C oven for at least 4 hrs. *Caution:* Aqua Regia is a strong acidic mixture and was handled according to OHSA guidelines. The sealed Parr bomb was heated at 170°C for 46-52 hrs. Surfaces were removed immediately from Parr bomb and stored under ambient conditions until use.

2.5.2.2 Hydrosilylation

Methyl and carboxylate functionalized pSi surfaces were prepared by initially removing dissolved gases and water from 1-dodecene and 10-undecanoic acid, respectively, via a minimum of four freeze-pump, thaw cycles on a schlenk line under

nitrogen gas. The reaction vessel was then sealed under nitrogen and taken to the HF preparation area. pSi surfaces were re-hydrogen terminated by a 30 sec immersion in 3:1 HF:ethanol solution, rinsed with ethanol, dried with nitrogen, and placed immediately in the reaction vessel, minimizing exposure to atmospheric conditions. The reaction vessel was placed back on the schlenk line with 12 immersed pSi surfaces and vacuum pulled for 10 minutes before heating. A silicon oil bath was preheated to 200˚C (methyl) and 150˚C (carboxylic acid). The reaction vessel was returned to a nitrogen atmosphere and heated for 2 hrs (methyl) or 12 hrs (carboxylic acid). After cooling, surfaces were removed and rinsed three times in each of the following solvents: acetone, methanol, and dichloromethane. Surfaces were stored under ambient conditions after drying with nitrogen and were stable for at least six months. Surface chemistry was confirmed via infrared spectroscopy.

2.5.2.3 Coupling Chemistry

Coupling chemistry was carried out by immersing carboxylic acid terminated surfaces in a 1 mL solution containing equal amounts of 0.1 M N-hydroxysuccinimide (NHS, >98% Sigma Aldrich) and 0.4 M *N*-(3-Dimethylaminopropyl)-*N*′-ethylcarbodiimide hydrochloride (EDC, >98% Fluka) for 1 hr.[25,26] Surfaces were rinsed with DI water and immediately immersed in amine solution ($R\text{-}NH_2$). A proof-of-concept coupling was carried out by immersion in 4 mL of neat 1-(3-aminopropyl)imidazole (IMD) at room temperature for 3 hrs. Coupling reactions for

mineralization studies were completed by immersion in 75 μL of 20 μg/mL osteopontin (OPN, bovine source from Dr. Sørensen, Denmark, Appendix Figure A2.1) in pH 8.5 borax buffer solution (BBS), 100 μL of 20 μg/mL bovine serum albumin (BSA, Fisher Brand) in pH 8.5 BBS, or 1 mL of 0.5 M 2-aminoethyl dihydrogen phosphate (ADP, Sigma Aldrich) in pH 9.5 BBS for 12 hrs, 12 hrs, and 3 hrs, respectively.[28] A PDMS membrane with 1 cm x 1 cm cut-outs was used for the small volume protein experiments to provide surface tension drawing the liquid across the silicon surface. OPN and BSA reactions were carried out at 4˚C and ADP at room temperature. Surfaces were then rinsed with pH 8.5 BBS and immersed in 10 mM hydroxylamine hydrochloride[43] (ACS reagent, Sigma Aldrich) in pH 8.5 BBS for 1hr followed by rinsing in pH 8.5 BBS, as well as DI water, to quench unreacted surface NHS. OPN and BSA surfaces were stored in pH 8.5 BBS for no longer than 4 days before use in experiment while ADP functionalized surfaces were stored under ambient air for no longer than 7 days. Surface chemistry was confirmed via infrared spectroscopy.

2.5.3 Infrared Spectroscopy

Infrared analysis of pSi functionality was conducted using a Bruker Vertex 80v FTIR with a Pike Technologies Miracle Germanium ATR (256 scans, under vacuum) and a MCTA detector or Bruker Hyperion 2000 microscope with Germanium ATR

attachment (64 scans, nitrogen atmosphere). Measurements on both instruments were carried out at 2 cm^{-1} resolution.

2.5.4 Scanning Electron Microscopy (SEM)

Scanning Electron Microscopy (SEM) studies of surface morphology and nucleation density were carried out on uncoated samples using a LEO FESEM 1550 (1.0 keV, 10.0 μm aperture). Energy-dispersive X-ray spectroscopy (EDX) was carried out this same instrument at 12.0 keV, 30.0 μm aperture after coating with ~15-20 nm of amorphous carbon using an Edwards Auto 306 Evaporator.

2.5.5 2-D X-ray Diffraction

2-D X-ray diffraction measurements were performed using a Bruker General Area Detector Diffraction System v 4.1.27 (D8 Discover with Bruker HI-STAR area detector). Data was collected for 300 sec, at a detector distance of 5.90 cm, CuKα source, 15 two-theta, 10 Ω, and with samples at 90˚ or 54˚ tilt angle. Reflections were assigned after unwarping data using the Bruker Axes software package.

2.5.6 Tris Buffered Solution Mineralization

Stock solutions of 10 mM $CaCl_2.2H_2O$ (Sigma Aldrich) and 6 mM $(NH_4)_2HPO_4$ were prepared in 0.15 M tris-hydroxy-methyl-amino methane (Tris) buffer (Trizma® acid and base, Sigma Aldrich) at pH 7.4 with phosphate solutions used within two weeks. All solutions contained 0.1% sodium azide (Fluka). Equal amounts of each solution were simultaneously combined in a 10 mL petri dish

resulting in an effective concentration of 5 mM Ca^{2+} and 3 mM PO_4^{3-}. A custom machined delrin sample holder to suspend the sample upside down was placed in the solution as well as the functionalized pSi sample (Figure 2.17). Each pSi sample was placed in a separate dish. Samples were sealed with parafilm to prevent evaporation for 18 hrs, 24 hrs, 3 days, and 5 days at room temperature (~20-22˚C). After removing from the reaction solution, samples were rinsed with 0.15 M NH_4OH, dried with nitrogen, and stored under ambient conditions until SEM and x-ray analysis.

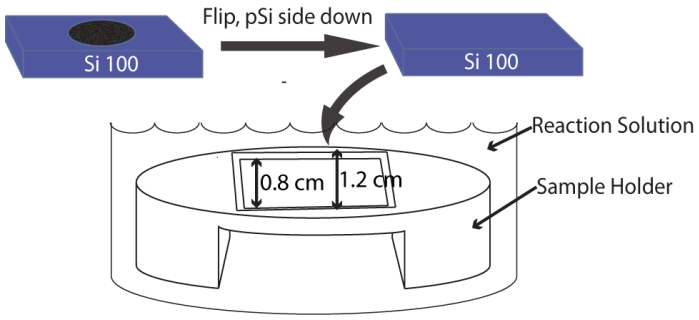

Figure 2.17: Schematic showing custom sample holder geometry and pSi sample orientation during the experiment. The central portion consisted of a outer square 1.2 cm x 1.2 cm that is 0.3 cm deep and inner square 0.8 cm x 0.8 cm creating a shelf for the pSi sample. This sample geometry prevented gravitational deposition of mineral and was maintained for all experiments.

2.5.7 Titration-controlled pH Method and Setup

The titration-controlled pH set up consisted of a 718 Stat Titrino with 765 Dosimate, combination glass electrode (item # 6.0233.10), combination ion electrode (calcium, item # 019019331), and Tiamo 1.1 software from Metrohm USA (Figure

2.18).[44] A jacketed reaction vessel with circulating water bath was utilized to maintain temperature at 25˚C. Stock solutions of 2 M NaCl (Sigma Aldrich, >99%), 1 M NaOH (Fisher), 400 mM NaH_2PO_4, and 400 mM $CaCl_2.2H_2O$ were prepared with 0.1% sodium azide within one week of experiment. Solutions of 0.1 M HCl were prepared as needed. Dispensor and titrator solutions were prepared according to equations 2.1 through 2.6 to maintain target concentrations (dispensor – Eqn. 2.1 and 2.2, titrator – Eqn 2.3 and 2.4), pH (7.4), and ionic strength (0.15 M) as well as to account for a 3:5 mL dosage ratio between dispenser and titrator. Tiamo software was set up with the following parameters: 1.5 mL maximum titration rate, 65 µL minimum titration rate, 0.5 mL after refill of dispenser/titrator, max total addition of 60 mL, monitor potential of calcium electrode, monitor pH of solution, and dynamic pH control.

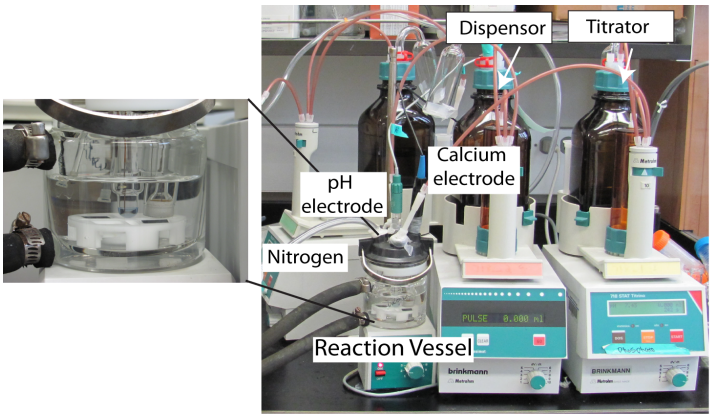

Figure 2.18: Photographs of titration-controlled pH set up with 718 Stat Titrino with 765 Dosimate, combination glass electrode, combination ion electrode, and Tiamo 1.1 software from Metrohm USA. The inset is a photograph of the jacketed reaction vessel with sample holder, titrator ports, and electrodes.

The pH electrode was calibrated using pH 4.00, 7.00, and 10.00 buffers (Fisher) and checked between runs with pH 7.40 buffer (Thermo). The jacketed reaction vessel, stir bar, and Teflon sample holder were soaked in 0.1 M HCl and DI water each for one hour followed by copious rinsing in DI water and drying with lint free cloths (VWR Catalog #: 21912-042) between each reaction. A nitrogen atmosphere was maintained in the reaction vessel but not bubbled into the solution. The 60 mL reaction solution was prepared with the stock solutions to contain 3.0 mM Ca^{2+}, 1.80 mM PO_4^{3-}, 0.15 total ionic strength (NaCl), and pH 7.4 (W_{NaOH}). Stock solutions were added in the following order – water, NaCl, PO_4^{3-}, NaOH, and Ca^{2+} – to prevent premature precipitation and formation of calcium carbonates. Two pSi samples that had been incubated in 0.4 M Ca^{2+} stock solution, pH 6.5, for 12 hrs, rinsed with DI water and dried with nitrogen were suspended in the reaction solution with stirring. Titrations were run until pH 7.3. Samples were rinsed with 0.15 M NH_4OH, dried with nitrogen, and stored under ambient conditions. Titration amounts, pH, and calcium electrode potential were exported to Microsoft Excel from the Tiamo software. Aliquots of reaction solution at the start and end of each reaction were taken for concentration analysis using flame atomic absorption (calcium) and UV-visible spectroscopy (phosphate).[45,46]

2.5.8 Titration Analysis

Igor analysis software was used to determine the time to nucleation, induction, and pH decrease as well as the differences associated between them. The nucleation

time is defined to be the time when the system started adding titrant; induction time was the point at which a tangent to the steepest part of the slope crossed the x-axis; pH decrease is the time point where the pH started to decrease after reaching a maximum; and SpH is the difference between nucleation and pH decrease.

2.5.9 Static pH Method and Setup

Stock solutions, buffers, sample holder, soaking/rinsing, and reaction concentrations were identical to those used in the pH Stat method. Static pH Method setup used Tiamo 2.3 software, 867 pH module, and Unitrode® electrode from Metrohm USA (Figure 2.19).[47] A homemade jacketed reaction vessel was constructed by using Torr® seal and sliced tubing to seal a 150mL beaker inside a 400 mL beaker with tubing ports. A peristaltic pump connected to a heated water reservoir and the reaction vessel was used to maintain reaction temperature at 25°C. Two sample incubation conditions were used – 1 hr in 0.4 M Ca^{2+}, pH 6.5 and 1 hr in 0.4 M Ca^{2+}, pH 9.5 – followed by rinsing in DI water and drying with nitrogen. Two samples were suspended upside down for each reaction and let react for 100 minutes with pH and temperature monitoring. Samples were rinsed with 0.15 M NH_4OH, dried with nitrogen, and stored under ambient conditions.

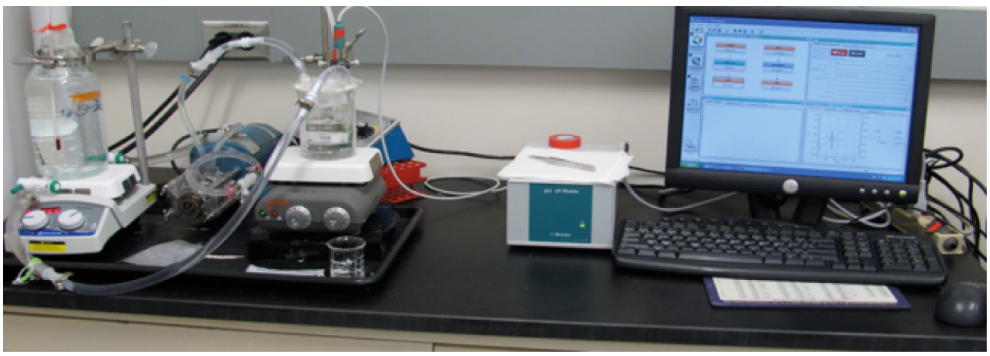

Figure 2.19: Photograph of static pH method setup using Tiamo 2.3 software, 867 pH module, and Unitrode® electrode from Metrohm USA as well as a custom jacketed reaction vessel.

REFERENCES

(1) Palmer, L. C.; Newcomb, C. J.; Kaltz, S. R.; Spoerke, E. D.; Stupp, S. I., Biomimetic Systems for Hydroxyapatite Mineralization Inspired by Bone and Enamel, *Chem. Rev.* **2008**, *108*, 4754.

(2) Murphy, W. L.; Mooney, D. J., Bioinspired Growth of Crystalline Carbonate Apatite on Biodegradable Polymer Substrata, *J. Am. Chem. Soc.* **2002**, *124*, 1910.

(3) Olszta, M. J.; Cheng, X. G.; Jee, S. S.; Kumar, R.; Kim, Y. Y.; Kaufman, M. J.; Douglas, E. P.; Gower, L. B., Bone Structure and Formation: A New Perspective, *Materials Science & Engineering R-Reports* **2007**, *58*, 77.

(4) Debruijn, J. D.; Klein, C.; Degroot, K.; Vanblitterswijk, C. A., The Ultrastructure of the Bone Hydroxyapatite Interface Invitro, *J. Biomed. Mater. Res.* **1992**, *26*, 1365.

(5) Boskey, A. L., Matrix Proteins and Mineralization: An Overview, *Connective Tissue Research* **1996**, *35*, 357.

(6) Qiu, S. R.; Orme, C. A., Dynamics of Biomineral Formation at the near-Molecular Level, *Chem. Rev.* **2008**, *108*, 4784.

(7) Wang, L. J.; Guan, X. Y.; Du, C.; Moradian-Oldak, J.; Nancollas, G. H., Amelogenin Promotes the Formation of Elongated Apatite Microstructures in a Controlled Crystallization System, *J. Phys. Chem. C* **2007**, *111*, 6398.

(8) Yang, X. D.; Wang, L. J.; Qin, Y. L.; Sun, Z.; Henneman, Z. J.; Moradian-Oldak, J.; Nancollas, G. H., How Amelogenin Orchestrates the Organization of Hierarchical Elongated Microstructures of Apatite, *J. Phys. Chem. B* **2010**, *114*, 2293.

(9) Buriak, J. M., Organometallic Chemistry on Silicon and Germanium Surfaces, *Chem. Rev.* **2002**, *102*, 1271.

(10) Bent, S. F., Organic Functionalization of Group Iv Semiconductor Surfaces: Principles, Examples, Applications, and Prospects, *Surf. Sci.* **2002**, *500*, 879.

(11) Canham, L. *Properties of Porous Silicon*; The Institution of Electrical Engineers: United Kingdom: INSPEC, 1997.

(12) *Proteins at Interfaces Ii: Fundamentals and Applications*; American Chemical Soceity: Washington, D.c., 1995.

(13) Gericke, A.; Qin, C.; Spevak, L.; Fujimoto, Y.; Butler, W. T.; Sorensen, E. S.; Boskey, A. L., Importance of Phosphorylation for Osteopontin Regulation of Biomineralization, *Calcified Tissue International* **2005**, *77*, 45.

(14) George, A.; Veis, A., Phosphorylated Proteins and Control over Apatite Nucleation, Crystal Growth, and Inhibition, *Chem. Rev.* **2008**, *108*, 4670.

(15) Omelon, S.; Baer, A.; Coyle, T.; Pilliar, R. M.; Kandel, R.; Grynpas, M., Polymeric Crystallization and Condensation of Calcium Polyphosphate Glass, *Mater. Res. Bull.* **2008**, *43*, 68.

(16) Wang, L. J.; Nancollas, G. H., Calcium Orthophosphates: Crystallization and Dissolution, *Chem. Rev.* **2008**, *108*, 4628.

(17) Koutsoukos, P.; Amjad, Z.; Tomson, M. B.; Nancollas, G. H., Crystallization of Calcium Phosphates - Constant Composition Study, *J. Am. Chem. Soc.* **1980**, *102*, 1553.

(18) Wang, L. J.; Guan, X. Y.; Yin, H. Y.; Moradian-Oldak, J.; Nancollas, G. H., Mimicking the Self-Organized Microstructure of Tooth Enamel, *J. Phys. Chem. C* **2008**, *112*, 5892.

(19) Nancollas, G. H.; Henneman, Z. J., Calcium Oxalate: Calcium Phosphate Transformations, *Urol. Res.* **2010**, *38*, 277.

(20) Wang, L. J.; Guan, X. Y.; Tang, R. K.; Hoyer, J. R.; Wierzbicki, A.; De Yoreo, J. J.; Nancollas, G. H., Phosphorylation of Osteopontin Is Required for Inhibition of Calcium Oxalate Crystallization, *J. Phys. Chem. B* **2008**, *112*, 9151.

(21) Kazmierczak, T. F.; Tomson, M. B.; Nancollas, G. H., Crystal-Growth of Calcium-Carbonate - a Controlled Composition Kinetic-Study, *J. Phys. Chem.* **1982**, *86*, 103.

(22) Boukherroub, R.; Wayner, D. D. M.; Lockwood, D. J.; Canham, L. T., Passivated Luminescent Porous Silicon, *J. Electrochem. Soc.* **2001**, *148*, H91.

(23) Linford, M. R.; Fenter, P.; Eisenberger, P. M.; Chidsey, C. E. D., Alkyl Monolayers on Silicon Prepared from 1-Alkenes and Hydrogen-Terminated Silicon, *J. Am. Chem. Soc.* **1995**, *117*, 3145.

(24) Parikh, A. N.; Allara, D. L.; Azouz, I. B.; Rondelez, F., An Intrinsic Relationship between Molecular-Structure in Self-Assembled N-Alkylsiloxane Monolayers and Deposition Temperature, *J. Phys. Chem.* **1994**, *98*, 7577.

(25) Lahiri, J.; Isaacs, L.; Tien, J.; Whitesides, G. M., A Strategy for the Generation of Surfaces Presenting Ligands for Studies of Binding Based on an Active Ester as a Common Reactive Intermediate: A Surface Plasmon Resonance Study, *Anal. Chem.* **1999**, *71*, 777.

(26) Sam, S.; Touahir, L.; Andresa, J. S.; Allongue, P.; Chazalviel, J. N.; Gouget-Laemmel, A. C.; de Villeneuve, C. H.; Moraillon, A.; Ozanam, F.; Gabouze, N.; Djebbar, S., Semiquantitative Study of the Edc/Nhs Activation of Acid Terminal Groups at Modified Porous Silicon Surfaces, *Langmuir* **2010**, *26*, 809.

(27) Voicu, R.; Boukherroub, R.; Bartzoka, V.; Ward, T.; Wojtyk, J. T. C.; Wayner, D. D. M., Formation, Characterization, and Chemistry of Undecanoic Acid-Terminated Silicon Surfaces: Patterning and Immobilization of DNA, *Langmuir* **2004**, *20*, 11713.

(28) Torres, A. J.; Holowaka, D.; Baird, B. A. In *Methods Mol. Biol.*; Rast, J. P., Booth, J. W. D., Eds.; Springer Science and Business Media: 2011.

(29) Miyazawa, T.; Blout, E. R., Infrared Spectra of Polypeptides in Various Conformations - Amide I and Ii Bands, *J. Am. Chem. Soc.* **1961**, *83*, 712.

(30) Cerda-Costa, N.; De la Arada, I.; Aviles, F. X.; Arrondo, J. L. R.; Villegas, S., Influence of Aggregation Propensity and Stability on Amyloid Fibril Formation as Studied by Fourier Transform Infrared Spectroscopy and Two-Dimensional Cos Analysis, *Biochemistry* **2009**, *48*, 10582.

(31) Adsorbed protein results on carboxylate terminated gold surfaces from Chapter 4.

(32) Mielczarski, J. A.; Dong, J.; Mielczarski, E., Real Time Evaluation of Composition and Structure of Concanavalin a Adsorbed on a Polystyrene Surface, *J. Phys. Chem. B* **2008**, *112*, 5228.

(33) Sieval, A. B.; Demirel, A. L.; Nissink, J. W. M.; Linford, M. R.; van der Maas, J. H.; de Jeu, W. H.; Zuilhof, H.; Sudholter, E. J. R., Highly Stable Si-C Linked Functionalized Monolayers on the Silicon (100) Surface, *Langmuir* **1998**, *14*, 1759.

(34) Durst, R. A.; Staples, B. R., Tris/Tris.Hcl - Standard Buffer for Use in Physiologic Ph Range, *Clin. Chem.* **1972**, *18*, 206.

(35) Craggs, A.; Moody, G. J.; Thomas, J. D. R., Evaluation of Calcium Ion-Selective Electrodes Based on Di(N-Alkylphenyl)Phosphate Sensors and Their Calibration with Ion Buffers, *Analyst* **1979**, *104*, 412.

(36) Aizenberg, J.; Black, A. J.; Whitesides, G. H., Oriented Growth of Calcite Controlled by Self-Assembled Monolayers of Functionalized Alkanethiols Supported on Gold and Silver, *J. Am. Chem. Soc.* **1999**, *121*, 4500.

(37) Meldrum, F. C.; Colfen, H., Controlling Mineral Morphologies and Structures in Biological and Synthetic Systems, *Chem. Rev.* **2008**, *108*, 4332.

(38) Cusack, M.; Freer, A., Biomineralization: Elemental and Organic Influence in Carbonate Systems, *Chem. Rev.* **2008**, *108*, 4433.

(39) Sommerdijk, N.; de With, G., Biomimetic Caco3 Mineralization Using Designer Molecules and Interfaces, *Chem. Rev.* **2008**, *108*, 4499.

(40) Omelon, S. J.; Grynpas, M. D., Relationships between Polyphosphate Chemistry, Biochemistry and Apatite Biomineralization, *Chem. Rev.* **2008**, *108*, 4694.

(41) Boskey, A. L.; Christensen, B.; Taleb, H.; Sorensen, E. S., Post-Translational Modification of Osteopontin: Effects on in Vitro Hydroxyapatite Formation and Growth, *Biochem. Biophys. Res. Commun.* **2012**, *419*, 333.

(42) Figure website reference http://sailorgroup.ucsd.edu/research/porous_Si_intro.html

(43) Kumar, A.; Malhotra, S., A Simple Method for Introducing - Sh-Group at 5'-Oh Terminus of Oligonucleotide, *Nucleosides Nucleotides* **1992**, *11*, 1003.

(44) Set up located in Adele Boskey's laboratory at the Hospital for Special Surgery with assistance from Lance Silverman.

(45) Lahti, R.; Heinonen, J., Reversible Changes in the Activity of Inorganic Pyrophosphatase of Streptococcus-Faecalis - the Effect of Compounds Containing Sh-Groups, *Acta Chemica Scandinavica Series B-Organic Chemistry and Biochemistry* **1981**, *35*, 33.

(46) Willis, J. B., The Determination of Metals in Blood Serum by Atomic Absorption Spectroscopy .1. Calcium, *Spectrochim. Acta* **1960**, *16*, 259.
(47) Set up located in Lara Estroff's laboratory at Cornell University.

APPENDIX 2

LPVKPTS*S*GS*S*EEKQLNNKYPDAVAIWLKPDPSQKQTFLAPQNS*VS*S*EET 50

DDNKQNTLPS*KS*NES*PEQTDDLDDDDDNS*QDVNSNDS*DDAETTDDPDHSD 100

ESHHS*DES*DEVDFPTDIPTIAVFTPFIPTESANDGRGDSVAYGLKSR SKK 150

FRRSNVQSPDAT*EEDFTS*HIES*EEMHDAPKKTSQLTDHS*KETNS*SELSKE 200

LTPK AKDKNKHSNLIES*QENSK LSQEFHS*LEDKLDLDHKS*EEDKHLKIRI 250

S*HELDS*AS*SEVN 262

Figure A2.1: Osteopontin peptide sequence.[41] The arrows indicate the separation between the three fragments used in Ref. 41: C-terminal, N-terminal, and SKK.

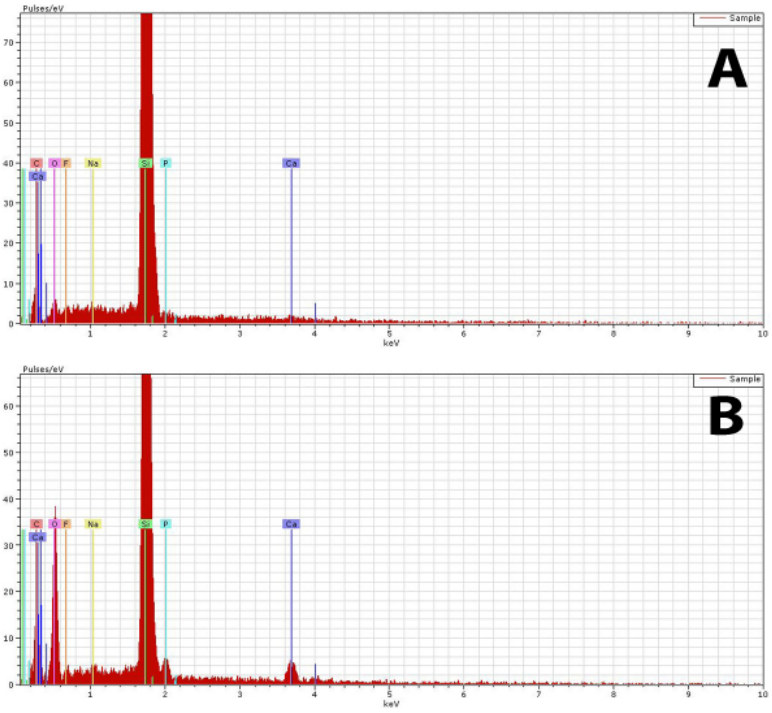

Figure A2.2: Representative EDX data for methyl (A) and carboxylate (B) surfaces that had been coated in ~15 nm of amorphous carbon. The calcium and phosphate peaks were integrated to get a ratio of calcium to phosphate. Silicon and oxygen peaks were from the underlying pSi substrate.

Chapter 3:

MINI-DOUBLE DIFFUSION HYDROGEL-BASED SYSTEM (mDDS) DESIGN AND CHARACTERIZATION FOR HYDROXYAPATITE MINERALIZATION IN AN INCUBATOR

3.1 ABSTRACT

The goal of this study is to design a 3-D environment that can be used to study the effects of hydroxyapatite (HA) mineral formation on cell behavior and vice versa. The design of such system requires a gel, which is solid at 37˚C and cell culture compatible, to mimic the extra-cellular matrix (ECM), as well as a compact design for incubator integration and gas permeability for cell viability. This chapter describes the evolution of two hydrogel-based double diffusion systems aimed at achieving cell integration – a combination system and a rigid polycarbonate system. The rigid polycarbonate mini-double diffusion system (mDDS) incorporating minimal polyethyleneimine (PEI) functionalization for gel adhesion and polydimethylsiloxane (PDMS) membranes for gas permeability was successful in demonstrating hydroxyapatite mineralization in both room temperature and incubator environments under comparable geometries at 46 hrs ± 30 minutes and 35 ± 2 hrs, respectively. Band positions were the same position and width for all three tubes in the system. Ion diffusivities have been calculated for an agarose-based mDDS system at 25˚C to be 9.77 ± 4.63 x 10^{-6} cm^2/sec for calcium and 8.82 ± 0.98 x 10^{-6} cm^2/sec for phosphate. The ion product, calculated using the calculated diffusivities and band appearance

time, was calculated to be 55.6 mM^2. Further characterization and system optimization are necessary for successful cell integration in this mDDS, however, this system shows promise for integration of cells in an agarose-based 3-D mineralization environment.

3.2 INTRODUCTION

Development of biomimetic materials for mineralized tissue and interface applications relies on understanding the carefully controlled interaction of cells, proteins, extracellular matrix, and mineral (hydroxyapatite; HA). In order to understand more about the interfaces within these materials, researchers use *in vitro* models to study cells, extracellular matrix, and mineral formation.[1-4] Traditional *in vitro* studies typically only combine two interactions not all three (i.e. cells and mineral or mineral and matrix or surfaces and mineral).[1-6] The lack of *in vitro* models to simultaneously combine all three components continues to challenge researchers. To understand the carefully orchestrated events of cells, proteins, extracellular matrix, and mineral (hydroxyapatite; HA), a new set of tools that allow for simultaneous study of cells, proteins, extracellular matrix, and HA interactions in a 3-D environment needs to be developed.

Traditional cell culture on flat surfaces, typically culture dishes do not accurately reproduce the *in vivo*, 3-D environments in which cells function. To transition from 2-D to 3-D cell culture models, a substrate with 3-D structure needs

to be used. These systems include porous polymer scaffolds such as PLG scaffolds[6,7] or hydrogels such as agarose, alginate, or collagen.[8-10] For example, Cukierman and co-workers have shown that fibroblastic cells display enhanced cell activity and narrowed integrin usage in 3-D vs. 2-D cell culture environments.[11] Differences in cancer cell signaling have also been observed as a result of 3-D cell culture, as presented by Fischbach and co-workers.[3] Oral squamous cell carcinoma (OSCC-3) cells displayed different regulation of interleukin 8 (IL-8) dependent upon whether the cells were cultured using 2-D or 3-D alginate cell culture systems. These examples demonstrate the need for designing a 3-D system for *in vitro* studies of cell-mineral (hydroxyapatite; HA) interactions.

A 'holy-grail' of calcium phosphate mineralization studies is to integrate cells into a 3-D controlled mineralization environment to study the effects of mineral on cell behavior and vice versa. Calcium phosphate mineralization within the body is affected by a number of small molecules, proteins, and cells within an extra-cellular matrix (ECM).[12-14] Hydrogels, such as alginate, gelatin, and agarose, closely mimic the ECM found in biological systems, and serve as a scaffold for cell culture making them an ideal model for *in vitro* studies of cell-mineral interactions.[15-17] Hydrogels can also be modified both chemically [18-20]and mechanically [5,18,21]to introduce gradients into the system as well as the gradients present via diffusion of ions.[2]

Typically, HA-cell interactions are studied by incorporating pre-synthesized particles[22] into the 3-D scaffold or mineral forming cells.[23] The mineral-ECM

interactions can be studied from room temperature, acellular mineralization experiments within a hydrogel environment.[4,17] However, a 3-D system in which both cellular effects on the mineralization process and mineralization effects on cells in an ECM can be studied, has yet to be realized. Such a system could be used to answer questions about, for example, how articlular chondrocytes, influence mineralization. At the bone-cartilage interface, articular chondrocytes do not directly form mineral but are thought to influence the mineralization process via the production of noncollagenous proteins (NCPs).[18,24] The ability to integrate cells and calcium phosphate mineralization into a hydrogel double diffusion system would provide greater insight into cell-ECM-mineral interactions of articular chondrocytes at the bone – cartilage interface *in vivo*.

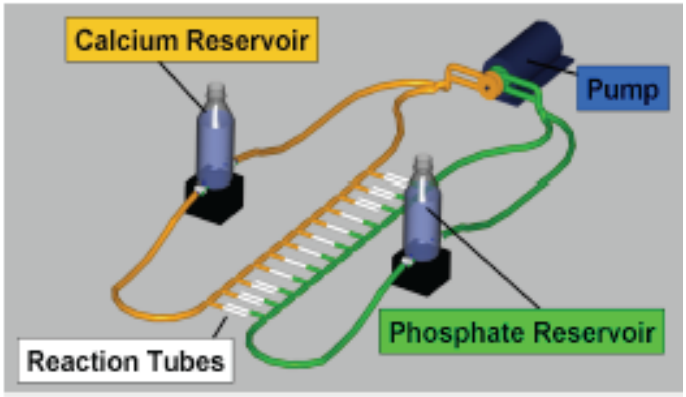

Figure 3.1: Circulating semi-infinite reservoir double diffusion system (DDS). This system uses circulating reservoirs of calcium and phosphate solutions to maintain turbulent mixing and solution concentrations of calcium and phosphate ions at the edge of the hydrogel reaction tubes.[2]

One possible system for cell integration is that of a circulating semi-infinite reservoir double diffusion system (DDS; Figure 3.1). The DDS system uses circulating reservoirs of calcium and phosphate solutions to maintain turbulent mixing and solution concentrations of calcium and phosphate ions at the edge of the hydrogel reaction tubes. The polystyrene hydrogel reaction tubes are filled with 10 w/v % 275 Bloom gelatin. A band of HA forms in the middle of the gel after approximately 3 days. Mineralization and diffusivity of calcium and phosphate ions in this gelatin system have been extensively characterized.[2,4] The DDS occupies a space approximately 3' x 3', uses rigid polystyrene tubes, which do not allow for oxygen and carbon dioxide gas exchange, and uses 10 w/v% gelatin, which flows at 37°C. These design features make it incompatible with an incubator and cell culture conditions.

3.2.1 Experimental Design

The following specifications must be considered in redesigning the DDS system for *in vitro* cellular studies – fit on a 21" x 21" shelf within the incubator, gas permeable (O_2 and CO_2 exchange) around the cells, reservoir tubing fit through a 1" port, all components sterilizable, and a hydrogel that does not flow at 37°C, as well as, being cell culture compatible. For my design, silicone tubing or membranes were used to achieve gas exchange and a cell culture grade agarose was chosen (Agarose BP165, Fisher) that did not flow at 37°C. The size and composition of the manifolds for ion delivery, tubing leading to the reservoirs, and reservoir type varied throughout the system development.

Prior to looking at a more complex system in the incubator, a single tube twin reservoir system (STR) was developed for use in a series of 'proof-of-concept' experiments for cell viability and incubator based mineralization (Figure 3.2). Debra Lin and others in the Estroff lab have done extensive work proving cell viability and mineralization under incubator conditions with the STR system.[25] Lack of mixing of reservoirs in this system relies entirely on diffusive transport, possibly creating concentration gradients at the gel interface. The STR system design uses a high volume of resources and space for a limited number of data points.

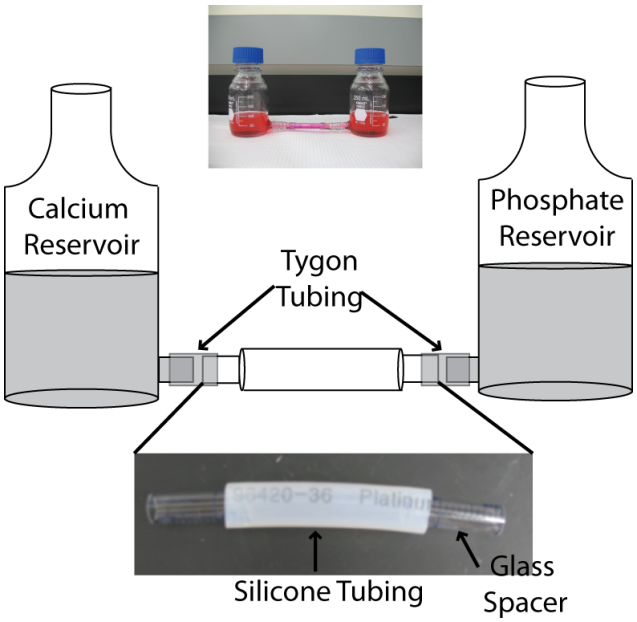

Figure 3.2: Single tube twin reservoir (STR) schematic. Media bottles (250mL) were modified with glass hose connections at a 90° angle to allow for the connection of the silicone tubing via a glass spacer using tygon tubing. The top picture is of an assembled STR system and the bottom is of the silicone tubing construct.

The work presented in this chapter details the evolution of prototypes aimed at

successful integration of cells into a DDS under incubator constraints. Two different DDS systems will be presented – a combination system and a rigid polycarbonate system – as well as design challenges and mineral/ion characterization where pertinent.

3.3 SYSTEM DESIGN

An incubator based double diffusion system appears simple in theory and concept but challenging in implementation. Several iterations of a design fitting the incubator and cell culture constraints were tested prior to the current design.

3.3.1 Initial Designs

3.3.1.1 Combination Double Diffusion System (cDDS)

The initial combination double diffusion system (cDDS; Figure 3.3) design combined the silicone tubing and glass spacers of the STR system (Figure 3.2) with the manifolds and circulating reservoirs of the DDS (Figure 3.1).[2] The cDDS had six manifold ports instead of twelve, a stainless steel tray to contain leaks in the incubator, and quick disconnects for quick assembly within the incubator environment. Quick-disconnect valves were used in the incubator to minimize solution leakage and handling time (Figures A3.1 and A3.2) while the polyethylene quick-disconnects (i.e., the connections used in the DDS) were used outside the incubator. Tubing length leading to the reservoirs and peristaltic pumps was adjusted to accommodate the incubator geometry. Combination heating/stirring plates were

placed under the reservoirs to heat the reservoir solutions to 40˚C when integrated into the incubator. The glass spacers were weakly covalently bonded to the BioPharm® silicone tubing via plasma cleaning. Silicone tubes were functionalized with polyethyleneimine (PEI) with a 1 cm PEI free window in the center, shown to be important for cell viability in STR systems.

Room temperature testing was done using 2 w/v% Agarose BP165 in 0.15 M Tris buffer (pH 7.4), 100 mM calcium and phosphate Tris solutions, and a table to emulate incubator space constraints. HA mineral bands, as confirmed via x-ray diffraction, appeared at 47 hrs ± 1 hr in the center of the gel proving that mineralization occurred at room temperature in this geometry.

Proving the geometry worked at room temperature was an initial step toward incubator integration. The first incubator experiment proved the tubing, reservoirs, and manifolds could be sterilized via ethanol sterilization procedures. Subsequent experiments were conducted with 0.5% w/v azide containing solutions and the system exterior sterilized with ethanol to efficiently use time and resources during prototyping while maintaining incubator sterility. The tubing leading to the reservoirs had to be changed to thinner walled tubing to accommodate a more rigid opening in the incubator than in the room temperature model.

Multiple attempts at HA mineralization in the incubator resulted in significant bypass leaks, rather than a controlled band of mineral near the center of the gel. Bypass leaks are defined as any mineralization that is not occurring in a controlled

fashion along the center of the gel and are typically characterized by long (i.e., ~ 3 cm) streaks of mineral in the gel. These 'leaks' are typically due to a failure of the gel to adhere to the reaction tube and ions flowing around rather than through the gel. The silicone tubing, while sufficient for the STR systems, was not rigid enough for handling with the cDDS manifold geometry resulting in delamination of the gel from the silicone tubing and multiple bypass leaks.

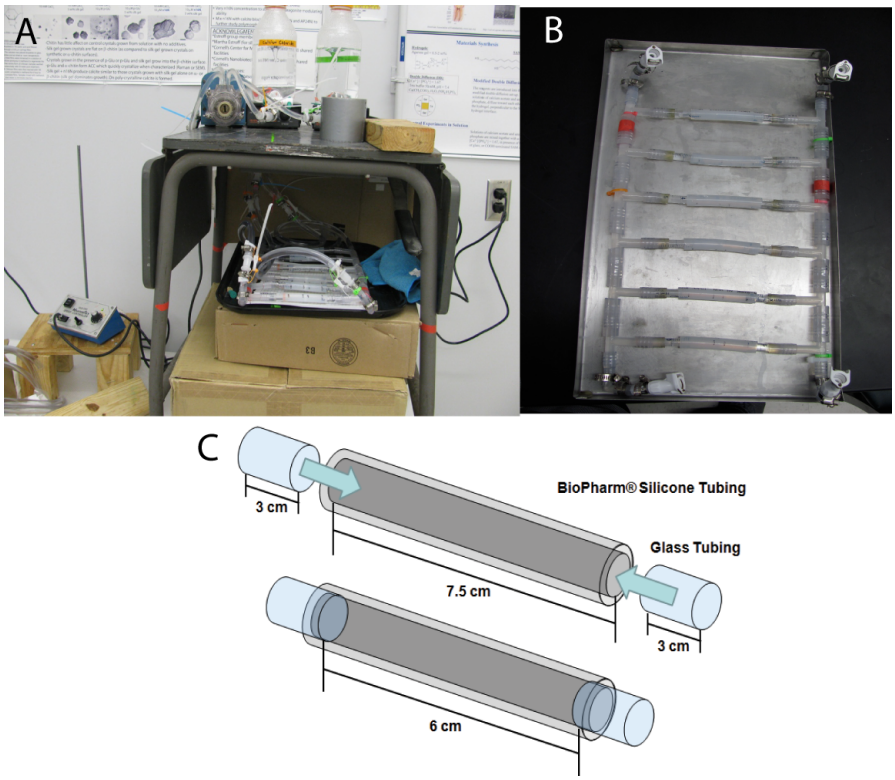

Figure 3.3: Combination double diffusion system (cDDS) using concepts from the STR and double diffusion system. The full set up (A) at room temperature emulates incubator space constraints. Image B demonstrates the manifold and gel-tube constructs from an incubator set up. General tubing specifications are shown in C.

3.3.1.2 Polycarbonate Double Diffusion System (pDDS)

Lessons from both the STR and cDDS were used to prototype a custom-built polycarbonate system (pDDS) – rigid design, compact, gas permeability around the gel, and gel adhesion with minimal chemical methods (Figure 3.4). I prototyped this system with the assistance of Glen Swan, a machinist in the chemical engineering machine shop. Manifolds and gel reaction assembly were constructed of rigid polycarbonate. The gel reaction assembly is defined as the components that contain the hydrogel. The dimensions (gel diameter and length) were kept as close to the DDS as possible to allow for more direct comparison of mineral timing and appearance, as well as diffusivities. Polycarbonate was chosen because it is autoclavable, machineable, and semi-transparent (for observation of mineral bands). To remove the need for functionalizing, a casting system set up was devised where the diameter was slightly larger in the casting frames than in the system frame. Only the top frame of the casting assembly would need to be changed (Figure 3.4) to a smaller frame creating a pressure seal. Polycarbonate washers were put at the intersection of the system frames and manifolds to prevent gel movement while O-rings were used to create a seal between the manifolds and system set up. Tubing was connected to the manifolds via NPT hose connections. To decrease the number of components, we initially tried using machined holes in the polycarbonate to provide gas permeability (Figure 3.4 and 3.5B). Tubing lengths, reservoirs, and connectors were the same as the cDDS while

the tubing diameter was changed to 1/4" I.D. to accommodate available plastic connectors.

The frame seal was tested by casting the gel, replacing the top frame with a system frame (without gas permeability holes), and placing the assembly in phenol red dyed 0.15 M Tris buffer, pH 7.4 (Figure 3.5A). Leaks between gels were not observed indicating a good seal between frame pieces. The system gas permeability holes proved to be too large, allowing for liquid leaking rather than just gas exchange. The polycarbonate washers prevented the movement of gel into the manifold but were challenging to keep track of in assembling and cleaning the system. While diffusion within this system was consistent using a frame without gas permeability holes, there was no gas exchange, a necessary component for cell viability. Commercially available silicone (PDMS) membranes at 0.024 and 0.040" thickness were then integrated into the system (Figure A3.3). The round geometry of the system did not allow for a leak proof integration of the membranes. It was also found that manifold attachment required O-rings and 8 in-line screws to achieve a leak proof seal. All of these considerations were taken into account for further system design modifications.

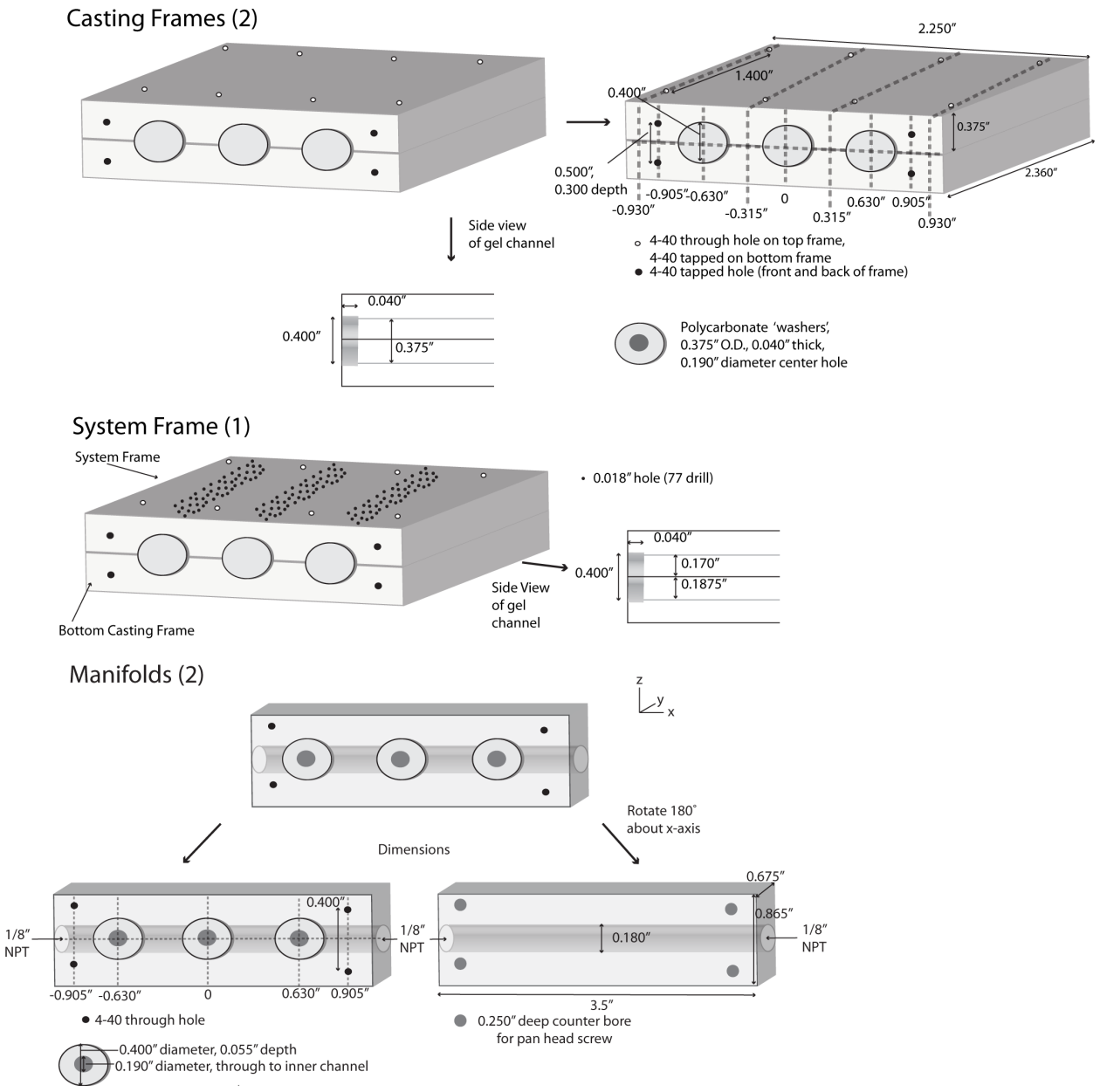

Figure 3.4: Initial polycarbonate double diffusion system design and specifications. All units are in inches with dash lines representing the grid for feature placement and measurements are from center to center. 4-40 screws were used to secure all components together with 012 O-rings between the manifold and system frames.

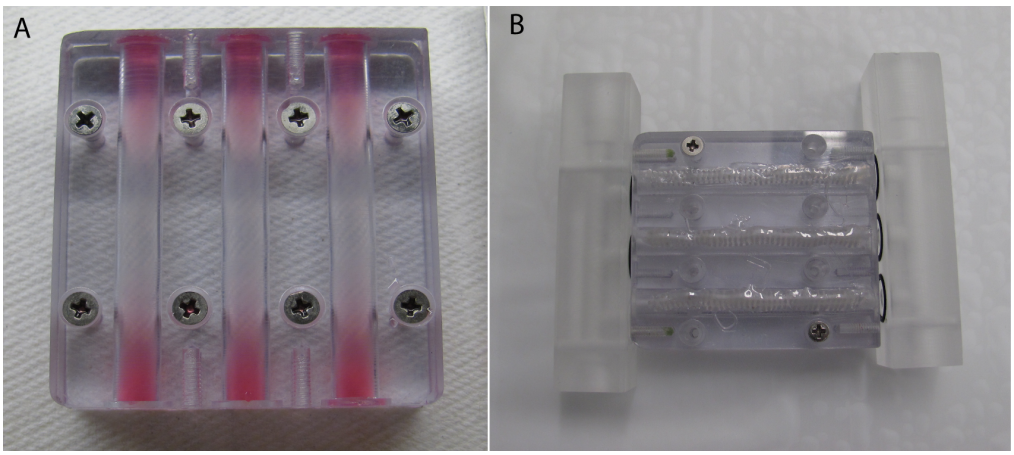

Figure 3.5: Pictures of initial polycarbonate incubator systems showing diffusion through the gel while soaking in Tris buffer dyed with phenol red (A) and the assembled set up (B). The diffusion of dyed liquid proved that there was a good seal between both system frames pieces.

3.3.2 Current Design: mini-Double Diffusion (mDDS) and incubator-Double Diffusion Systems (iDDS)

Based on lessons from the initial polycarbonate design, the following design modifications were made: square vs. circular geometry of the gel channels, modular system assembly, PEI functionalization, PDMS membranes, and slightly larger assembly for ease of handling (Figure 3.6 and 3.7). Square geometry increased the ease of machining allowing for quicker prototyping (i.e., I could machine everything but the manifolds using the Cornell LASSP student machine shop, rather than professional machinists) and allowed for the modular assembly. PEI Functionalization of only the spacers provided enough adhesion within the system for consistent mineral formation (i.e., no bypass leaks) at both room temperature and in the incubator (Figure 3.8). Frames were added to provide a leak-free seal between the

0.024" PDMS membranes and the body portions of the assembly. The PDMS membranes bunched slightly in the channels of the system when completely tightened. The geometry of a port connection at the bottom of the manifold was changed to a right angle to decreasing tubing kinks.

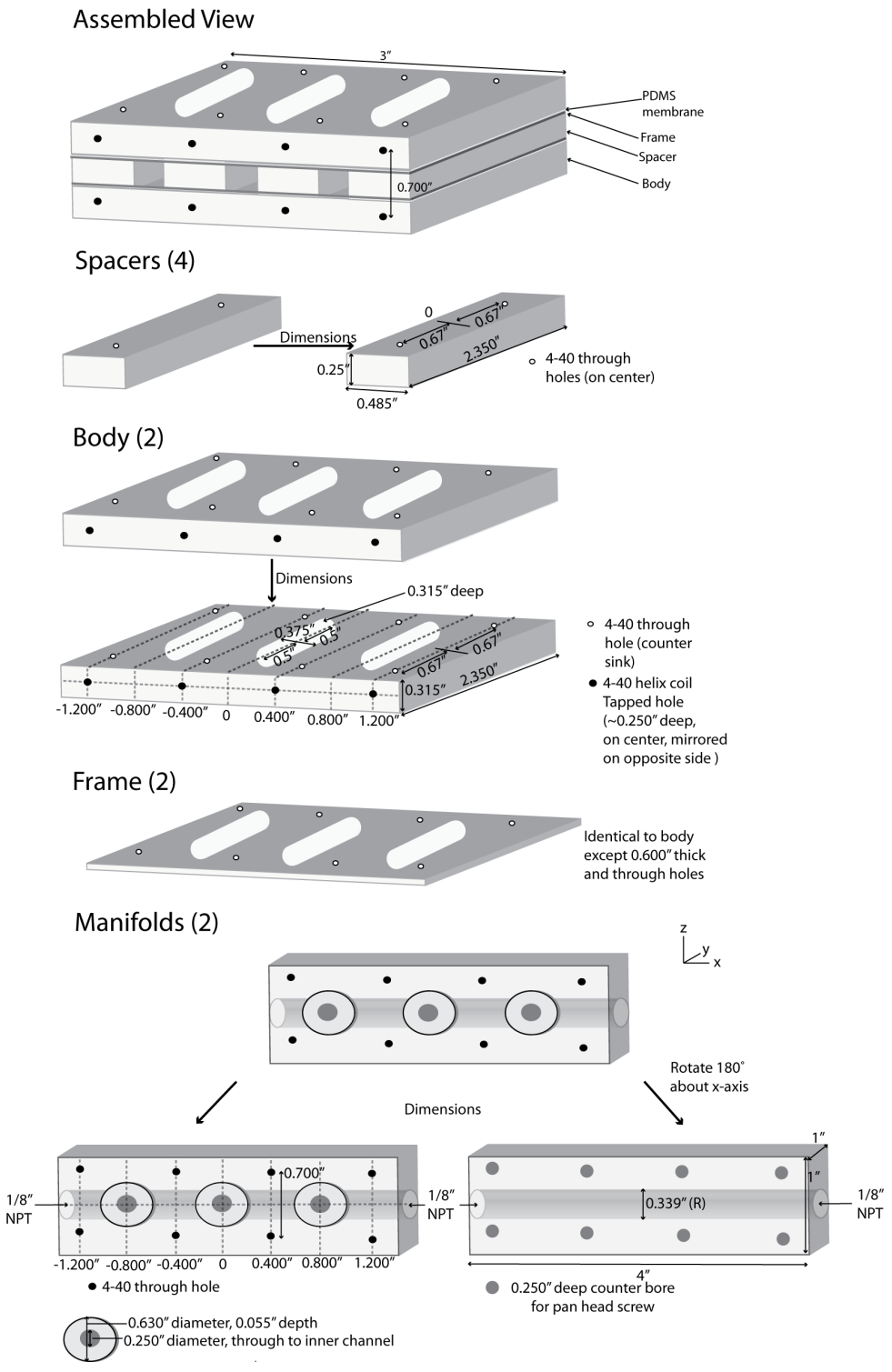

Figure 3.6: Mini-Double Diffusion (mDDS) and incubator-Double Diffusion System (iDDS) design and specifications. All units are in inches with dash lines representing the grid for feature placement and measurements from center to center. Eight 1-1/4" 4-40 flat head screws with nuts were used to assemble the system components. Six 204 O-rings were used between the manifold and system assembly as well as 16 - 1" pan head screws.

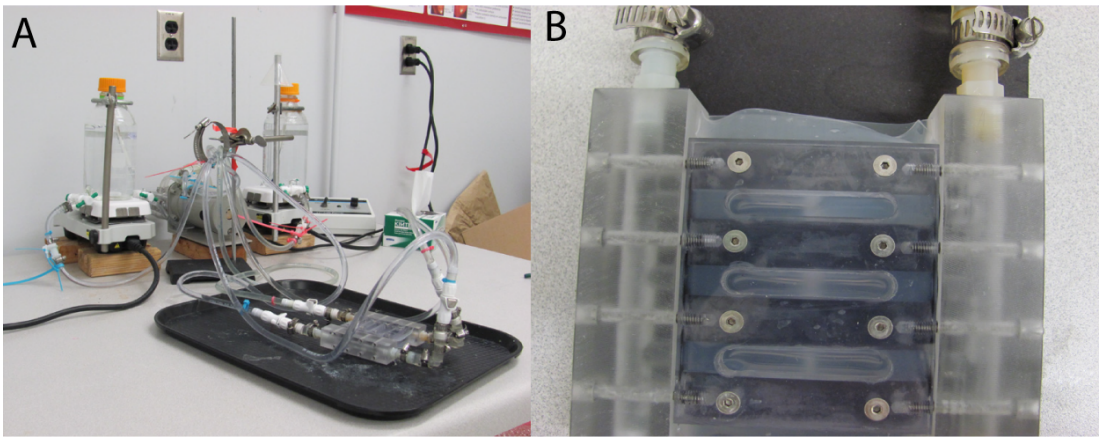

Figure 3.7: Pictures of the assembled mini-Double Diffusion System (mDDS). The full setup (A) emulating the incubator geometry as well as a closer view of the assembled system (B) with mineral bands are shown.

Full characterization (diffusivities, mineral timing, and mineral phase) was completed after proving that mineralization would occur at both room temperature conditions and incubator conditions (Figure 3.8). For notation consistency, the system run at room temperature is noted as the mini-double diffusion system (mDDS) and in the incubator as incubator-double diffusion system (iDDS).

3.4 ROOM TEMPERATURE CHARACTERIZATION (mDDS)

3.4.1 Mineralization

Mineralization experiments were preformed at room temperature to calibrate the system. Mineral phase was confirmed via powder x-ray diffraction. The mineral timing (i.e., the amount of time it takes for a mineral band to appear in the hydrogel) is used in conjunction with calcium and phosphate diffusivities for determining ion

concentrations and thus ion product/super saturation threshold at the point of mineralization. Three separate five-day experiments were analyzed. Reservoirs of 100 mM phosphate and calcium in 0.15 M Tris buffer were used. The system was prepared between runs by cleaning with soap and water, weak acid rinsing, thorough DI water rinsing, and drying. Gels were cast in the assembled system using a polycarbonate piece in place of a manifold and then hydrated for 40-48 hrs in 0.15 M Tris buffer, pH 7.4. Each reservoir was topped off to the same level after removing air bubbles from the tubing. 'Room temperature' varied between 20.3 and 21.8˚C for experiment duration. After five days, mineral phase was confirmed to be hydroxyapatite via powder x-ray diffraction (pXRD; Figure 3.8B). Initial band appearance occurred at 46 hrs ± 30 min.

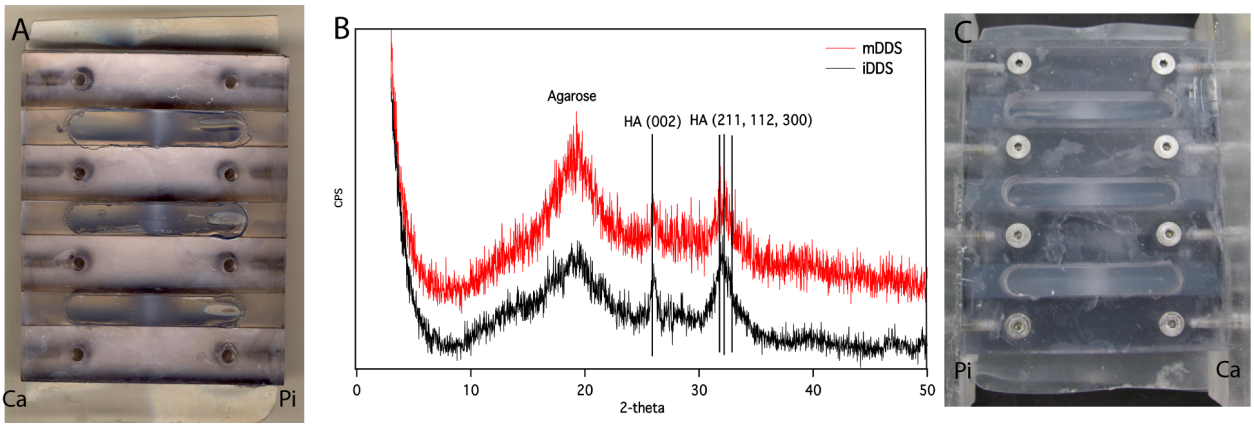

Figure 3.8: Scan of gels run at room temperature (A), picture of incubator bands (C), and pXRD data (B) confirming hydroxyapatite of room temperature (mDDS) and incubator (iDDS) double diffusion system.

3.4.2 Diffusivity

Ion diffusivities of calcium and phosphate ions in this system were calculated using the equation and conditions outlined by Dorvee and co-workers.[2] The mDDS was set up identical to mineralization experiments in 3.4.1 except with one of the reservoir solutions replaced by a 0.15 M Tris buffer, pH 7.4 sink. The sink reservoir is sufficiently large (>25 mL) for the diffusivity approximations and boundary conditions to be satisfied. The system was run for 4 days. Upon completion, the gels were sliced into 9 sections, placed in pre-massed tubes, and remassed (tubes and gel). Gels slices were massed to account for variability in gel dimensions as a result of PDMS membrane bunching. The gel cutter used was most consistent when slicing from the two ends towards the center two razor blades at a time (Figure 3.9). A volume to mass ratio of 0.95 was calculated by using fully hydrated gels cast in glass tubes whose dimensions were accurately measured. Gels were hydrolyzed and diluted for ICP-AES analysis.

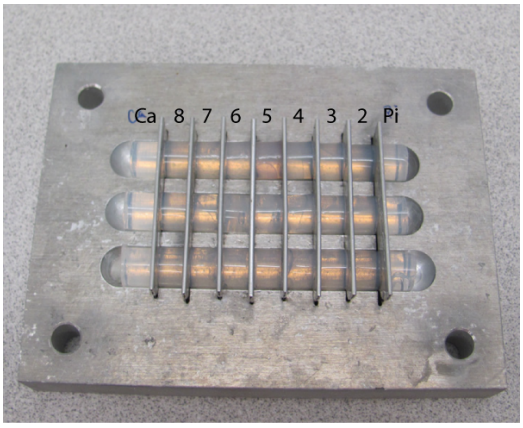

Figure 3.9: Picture of gel cutter with gels. Gel slice numbers are noted with the 'Pi' and 'Ca' orientation, which was maintained between experiments. Slices 2-8 are 0.255" wide, while slices 1 and 9 are 0.285" wide.

Ion diffusivities were calculated using Eqns. 3.1 and 3.2 (Table 3.1).[2,26] Eqn. 3.2 is an approximation used to calculate D at the distance, *x*, from the source where c = $c_0/4$ (c_0 is the source concentration). This approximation is unique to the diffusion equation where the solution of the *erfc(x)* is ¼ when the concentration is 25% c_o. The calcium diffusivity was calculated using five 'tubes' (2 separate runs) and phosphate was calculated using 6 'tubes' (2 separate runs). Each run contained a maximum of 3 'tubes' based on system construction. The concentrations of calcium and phosphate in the gel at mineralization were calculated using D and the mineralization band appearance time, t, (Eqn. 3.1), which were then used to calculate the ion product.

$$c(x,t) = c_0 erfc\frac{x}{2\sqrt{Dt}} \quad \text{(Eqn. 3.1)}$$

$$x = 1.6\sqrt{Dt} \quad \text{(Eqn 3.2)}$$

Table 3.1: Calculated diffusivity, D, values for agarose BP165 2 w/v% values and reported values[2] for Gelatin 225 Bloom 10 w/v%.

Gel Type	Reservoir	Tube Length	Diffusivity ($x10^{-6}$ cm^2/ sec)
Gelatin 225 Bloom 10 w/v%	Calcium	6 cm	5.81 ± 0.17
	Phosphate	6 cm	3.91 ± 0.41
Agarose (BP165) 2 w/v%	Calcium	6 cm	9.77 ± 4.63
	Phosphate	6 cm	8.82 ± 0.98

The concentrations at the point of initial mineralization were used to calculate an ion product of 55.6 mM^2, which compares closely to that reported (56.24 mM^2) in literature for 2 w/v % agarose at 37˚C.[27] The ion product at the time of mineralization represents the supersaturation threshold for the gel. The diffusivities calculate for this system (Table 3.1) are almost two times faster than those observed for 10 w/v % gelatin (Type A, 275 bloom) at 25˚C.[2] Each hydrogel has differing interactions with ions and tubing chemistry (i.e., PEI vs. polystyrene), changing the diffusivity of ions through the system. The difference in diffusivity values between gelatin and agarose demonstrate that diffusivities need to be determined for each gel and gel concentration.

3.5 INCUBATOR CHARACTERIZATION (iDDS)

3.5.1 iDDS Setup

The integration of the mDDS into the incubator presented several challenges - sterility, band appearance observation, and time the incubator doors can be open. This system requires that sterility be maintained as well as having a more confined

space (Figure 3.10). Doors cannot be opened for more than a couple of minutes before the temperature (37˚C) and atmosphere (5% CO_2, 100 % humidity) fluctuations risk affecting other cell culture experiments in the incubator. Air bubbles in the tubing were removed over several door openings rather than immediately to minimize temperature and atmosphere fluctuations. Further details of the incubator set up specifics are found in Section 3.8.1.7. Band appearance was monitored by opening the incubator doors and moving the tray until gel observation was possible.

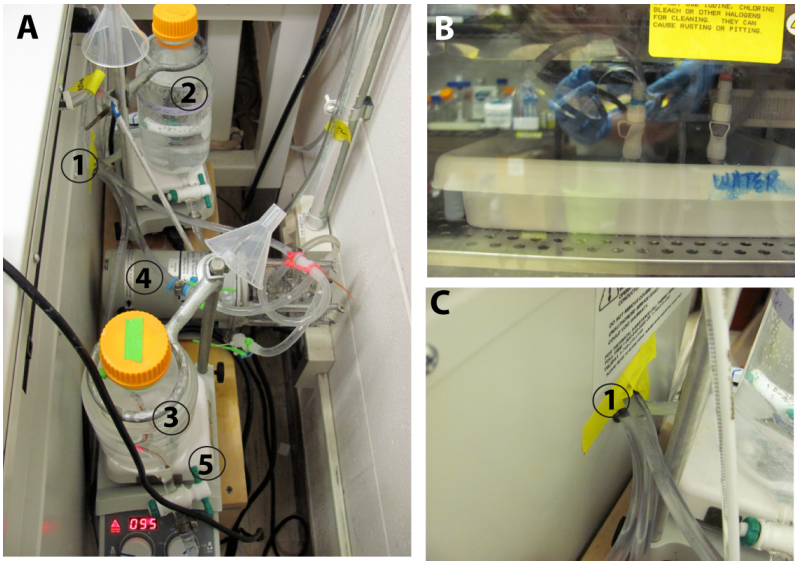

Figure 3.10: Pictures of incubator space constraints showing the shelf set-up for the reservoirs and pump behind the incubator (A), the assembled system through the glass window of the incubator (B), and the 1" port the tubing must pass through (C). The port in the back of the incubator (1), reservoirs (calcium (2) and phosphate (3)), peristaltic pump (4), and stirring/hotplates (5) are shown.

3.5.2 Mineralization

Two successful mineralization runs under the same conditions as outlined in 3.4.1 were carried out with the incubator modifications (heating and space constraints). The mineral band appearance was at 35 ± 2 hr. Mineral was confirmed to be hydroxyapatite via pXRD (Figure 3.8). Handling of this system proved to have the most effect the mineral band consistency and appearance. Minimized handling of the system (i.e. move tray as little as possible, do not remove assembly from incubator until experiment completion, etc.) is necessary for reproducible results. If the assembled system was not laying flat in the tray, pressure differences caused ions from one side to move faster through the system. Additional characterization of mineralization and diffusivity in this system should be carried out prior to further experiments in the incubator (i.e., cell integration, proteins, etc.).

3.6 FUTURE OF THE mDDS/iDDS SYSTEM

3.6.1 Characterization

While the mDDS/iDDS demonstrates a lot of promise, further analysis of the diffusivities should be carried out at both room temperature and in the incubator. The standard deviation of the calcium ion diffusivity at room temperature is much larger than would be ideal for predictive calculations while the phosphate results are within expected error. Likely sources of variablity include interaction with the PEI coating on the spacer and decreased effectiveness of the PEI coating on the spacers over time

(i.e., the spacers need to be replaced on a regular basis or plasma clean spaces prior to PEI functionalization). Additional calcium diffusivity experiments once the effectiveness of the PEI coating is determined would decrease this error. Once diffusivities in the incubator are completed, results between gels at room temperature and in the incubator can be compared. The literature suggests that diffusivities vary 2-3% per ˚C from the value at 25˚C.[28] Having results from both conditions will not only validate this prediction but also allow for more direct comparison of room temperature and incubator condition results.

This system also has the potential for monitoring how cells and proteins are affected by ion and mineral gradients in a 3D gel environment by selective placement of the cells or protein along the gel construct. For example, cells could be placed 1 cm off center towards the calcium side to monitor how the placement affects mineral formation in the center of the gel. Cell integration studies should be carried out to determine if additional modifications need to be made regarding gel adhesion (i.e., a PEI free window for cells due to PEI toxicity[29]) and membrane effectiveness for gas exchange. Functionalization of the PDMS membrane should be avoided to maintain gas permeability.

3.6.2 Design and Integration Considerations

The mDDS/iDDS has a lot of potential, however, there are several design considerations yet to be optimized. The PEI functionalization appears to not be as effective as time progresses based upon the observation that experiments have

become less reproducible with the same protocol. To test this hypothesis, new spacers should be made and tried within the system in addition to trying a plasma 'clean' step prior to NaOH hydrolysis in the PEI protocol determining whether spacers should be changed out periodically or if they can be chemically restored. Should gel adhesion become a problem in the future after the spacer functionality problem has been determined, the mDDS/iDDS frames could also be PEI functionalized to provide an additional gel adhesion surface. Should future experiments show that the PEI functionalized pieces need to be changed out periodically, functionalization of the frames should be avoided as they are a time intensive machining project. The machining time of the system pieces could be significantly decreased by using the water jet available in Cornell's LASSP machining facility.

The quick disconnect valves (Figure A3.1 and A3.2) while convenient in the incubator also proved to be finicky. If they were not seated well within the male-female connections, leaks and pressure differentials became problematic. Small pieces of gel would occasionally become lodged within these valves causing pressure differences between Ca and Pi manifolds resulting in system failures. These valves, even though chemically resistant, also started to show wear after about 3 months due to ionic solution exposure. Should these valves continue to be the best option, they should be thoroughly cleaned between runs and changed out approximately every three months. Ideally, a better quick disconnect valve can be found that will provide the ease of connection, seal when disconnected (i.e., minimize leaks within the

incubator), and open flow design.

A larger number of gel channels or assemblies in the system would assist in experiments analyzing multiple time points. For example, the ability to take one, three, and seven day cell viability time points (three gels for each) in tandem would decrease the amount of resources needed and increase consistency among time points. The geometry constraints of this system would allow for the attachment of an additional system of three gels with an inline (no 90° bend) connection prior to the current system manifold. To decrease the space necessary for each system-manifold set-up, the space between gels could be reduced allowing for the possibly of up to nine gels in parallel, which also requires remachining of the system-manifold set up. Finding quick disconnect valves that take up less space could increase the number of system-manifold set-ups that could be fit in the incubator. The valves would need to be plastic and able to withstand sterilization. Regardless, tubing kinks need to be minimized and only one set of tubing can be fit through the incubator opening. New manifolds and systems could be easily machined so that 3, 6, 9, or 12 gels could be analyzed for a specific time point, but would still require a new set up for each time point. Extensive flow, pressure, and concentration studies would need to be conducted if multiple systems were connected in series, stacked on top of each other. The use of y-tubing connectors may minimize potential flow differences, however, the amount of tubing to achieve this type of set up could become prohibitive within the incubator space constraints.

3.7 CONCLUSIONS

The evolution of a hydrogel-based double diffusion system for cell integration described in this chapter sheds light on many of the design considerations necessary for achieving the 'holy-grail' – a 3-D hydrogel double diffusion system integrating cells and calcium phosphate mineralization. The design constraints include a compact design, incubator geometry constraints (tubing inputs, shelf positions, etc.), gas permeability, gel adhesion, and setup time. A rigid polycarbonate system incorporating minimal PEI functionalization for gel adhesion and PDMS membranes for gas permeability was successful in demonstrating consistent mineralization in both room temperature and incubator environments under similar geometries at 46 hrs ± 30 min and 35 ± 2 hrs, respectively. Diffusivities and the ion product at mineralization have been successfully calculated for an mDDS system at room temperature to be 9.77 ± 4.63 x 10^{-6} cm^2/sec (calcium), 8.82 ± 0.98 x 10^{-6} cm^2/sec (phosphate), and 55.6 mM^2. Further characterization and optimization of the system is necessary for successful cell integration in a gel-based double diffusion system in an incubator environment.

3.8 MATERIALS AND METHODS

3.8.1 Combination Double Diffusion System (cDDS)

Quick-disconnect valves were used in the incubator (Value Plastics, Figures A3.1 and A3.2) while the polyethylene quick-disconnects (Fisher, No. 6150-0010) were used outside the incubator. As in the DDS[2], 3/8" I.D., 7/8" O.D. tygon tubing was used to connect the reservoirs and Saint-Gobain plasticizer free tubing (Fisher, No. AE300007) in peristaltic pump (Figure 3.3). System manifolds were constructed according to Ref. *2* with only 6 ports. Combination heating/stirring plates were placed under the reservoirs to heat the reservoir solutions to 40˚C when integrated into the incubator and maintain stirring at 700 rpm. The tubing leading to the reservoirs had to be changed from 3/8" I.D., 7/8" O.D. to 3/8" I.D, 5/8" O.D to accommodate a more rigid opening in the incubator than in the room temperature model.

Reservoirs of 100 mM phosphate ($(NH_4)_2PO_4$, Sigma Aldrich) and 100 mM Calcium ($CaCl_2.2H_2O$, Sigma Aldrich) in 0.15 M Tris buffer (Trizma® acid and base, Sigma Aldrich), pH 7.4 with 0.5% sodium azide (Fisher) were used. Reservoirs were constructed of 1 L media bottles (Kimax® Kimball 1000mL Media Bottle, No. 14395) with glass hose barbs on each side angled down at ~ 30° (Custom Addition, Cornell Glass Shop). Experimental reservoir volumes were 900 mL in each reservoir with volumes at the same level in each reservoir to prevent pressure differentials in the system. Reservoir solutions were stirred at approximately 700 rpm during the experiment. Room temperature testing was done using 2 w/v% agarose BP165, cell

culture grade (Fisher) in 0.15 M Tris buffer (pH 7.4). The outer surfaces were rinsed with ethanol for sterilization in the incubator system. Room temperature mineralization experiments were run for 5 days, while incubator experiments were run until a failure or bypass leak occurred.

3.8.1 Glass-Silicone Tubing Preparation

The glass spacers, cut using a diamond wire saw (WELL 4020), were weakly covalently bonded to the BioPharm® silicone tubing (3/5" O.D.) by plasma cleaning (Plasma Cleaner PDC-32G, Harrick Plasma) both the glass and silicone pieces for 1 minute and immediately inserting them together. Silicone tubes were functionalized with polyethyleneimine (PEI; 50% w/v, Sigma Aldrich) with a 1 cm PEI free window (marked on the outside with a sharpee marker)[29] in the center by plasma cleaning the tubing constructs for 2 minutes, *filling the tubing to the bottom of the 1 cm window with 0.5% w/v PEI in water, incubating up right for 12 hrs at room temperature, capping the opposing end with parafilm, and drying upright at 70˚C for 4 hrs. This procedure was repeated from * on for the other side without the initial plasma clean.

3.8.3 Sterilization of cDDS

Full sterilization (inner and outer surfaces) of the cDDS was accomplished via ethanol sterilization procedures. The tubing and manifolds were filled with ethanol for an hour, reservoirs were soaked in ethanol for 1 hr, additional parts (valves, silicone tubing, parafilm) were soaked in ethanol, and all parts were dried in the cell culture hood.

3.8.2 Polycarbonate Double-Diffusion System (pDDS)

Manifolds and gel reaction assembly were constructed of rigid polycarbonate (Table A3.1). All parts were machined by Glenn Swan of the Cornell Chemical Engineering Machine Shop. The dimensions (gel diameter and length) were kept as close to the DDS[2] as possible. Full system dimensions are given in Figure 3.4. Polycarbonate washers were put at the intersection of the system frames and manifolds to prevent gel movement while 012 O-rings were used to create a seal between the manifolds and system set up. Tubing was connected to the manifolds via plastic 1/8" NPT hose connections with 1/4" I.D (Table A3.1). Tubing diameter was changed to 1/4" I.D., 1/2" O.D to accommodate available connections and incubator port constraints. Tubing lengths, reservoirs, reservoir parameters, and connectors were the same as the cDDS (Section 3.8.1).

Commercially available silicon membranes at 0.024 and 0.040" thickness were integrated into the system (Figure S3.3) as an alternative to the machined gas permeable holes. The systems round geometry did not allow for a leak proof integration of the membranes. Leak proof manifold attachment required O-rings and 8 in-line screws rather than the 4 shown in Figure 3.4.

3.8.3 Mini-Double Diffusion System (mDDS)

All polycarbonate parts except for the manifolds, were machined by Amy Blakeley using the Cornell LASSP student machine shop (Figure 3.6). Manifolds were machined by Glenn Swan of the Cornell Chemical Engineering Machine Shop. PEI

functionalization of the spacers was achieved by hydrolyzing the spacers in 2 M NaOH for 1 hr, rinsing in DI water, soaking in 0.5% w/v PEI (50% w/v, Sigma Aldrich) in water for 12 hrs, and drying upright for 4 hrs at 70˚C.[30] The spacers were placed upright along the edge of polycarbonate spacers to allow excess liquid to drain without drying in a pool on the one end of the spacer. Holes in the PDMS membranes for the screws to pass through were formed by using a 16-gauge needle to pierce the membrane, using the frame (Figure 3.6) as a template. Tubing diameter was 1/4" I.D., 1/2" O.D, a plastic right angle tubing connector was used for the female quick disconnect angle (bottom of manifold), and plastic 1/8" NPT tubing connectors for tubing to manifold junctions (Table A3.1).

3.8.3.1 mDDS Mineralization Experiments

Reservoirs of 100 mM phosphate ($(NH_4)_2PO_4$, Sigma Aldrich) and 100 mM calcium ($CaCl_2.2H_2O$) in 0.15 M Tris buffer, pH 7.4 with 0.5% w/v sodium azide (Sigma Aldrich) were used. Reservoirs, reservoir parameters, and connectors were the same as the cDDS (Section 3.8.1). The system was prepared between runs by cleaning with soap and water, sonicating in 0.1 M HCl for 20 minutes, sonicating and rinsing with DI water, rinsing with 100% ethanol, and drying in a 70˚C oven for ~2 hrs. Gels (2 w/v% Agarose BP165, cell culture grade in 0.15 M Tris buffer, pH 7.4) were cast in the assembled system using a polycarbonate piece. The polycarbonate piece is a 4" x 2" flat piece with through holes at the same locations as the manifold. This piece is attached to the assembled system using 4-40 screws with 204 O-rings

between the assembled system and polycarbonate piece. After the hydrogels have solidified, the polycarbonate casting piece is removed. The cast hydrogels and assembly were hydrated for 40-48 hrs in 0.15 M Tris buffer, pH 7.4. After removal from the hydration solution, the hydrogels are trimmed to make sure that they are flush with the assembly edges. The polycarbonate manifolds were attached to the assembly using 204 O-rings and 4-40 screws paying attention to gradually tightening the screws in an alternating pattern to prevent thread stripping. Each reservoir was topped off to the same level of ~ 900 mL after removing air bubbles from the tubing. The peristaltic pump was set to the lowest possible setting that maintained circulation in this geometry (setting of 2). 'Room temperature' varied between 20.3 and 21.8°C for experiment duration.

3.8.3.2 mDDS Diffusivity Experimental Details

The experiment solutions and gels were prepared the same as in Section 3.8.3.1. Hydration of the hydrogels for 40-48 hrs in Tris buffer was also maintained. When setting up the experiment, one of the reservoir solutions was replaced with 0.15 M Tris buffer, pH 7.4 sink. For a system aimed at calculating calcium diffusivities, a 100 mM calcium reservoir was paired with a 0.15 M Tris reservoir and vice versa for the phosphate diffusivities. Systems were run for approximately 4 days with exact start and stop times recorded. The total time the system was run was *t* used in Eqn. 3.2.

All nine gel slice concentrations for the three gel channels were analyzed from the first run to determine which slice would be ~25 mM (i.e.; $c_0/4$).[26] In subsequent

experiments, the four slices surrounding the 25 mM slice were sent for ICP-AES analysis (slices 3-6, 'Pi' side labeled as 1) as well as both reservoir concentrations (Figure 3.9).

3.8.4 Incubator-Double Diffusion System (iDDS)

Integrating the mDDS into the incubator required several modifications. Air bubble removal occurred over several door openings rather than immediately to minimized temperature and atmosphere fluctuations. A plastic tray, 19" x 19" x 1" (length x width x height), was sterilized with ethanol and used to contain any condensation or unintentional leaks. The reservoirs and heating/stirring plates were placed on a wooden shelf behind the incubator to decrease the amount of tubing outside the incubator for temperature stability and condensation in the incubator as well as minimize pressure differences (i.e., wooden shelf approximately the same height as incubator shelf). The incubator shelf was placed four notches from the top to keep the tray as close to the opening in the back of the incubator while maintaining enough room to work with the system. Input and return flow tubing for each ion source was feed through a 1" hole in the back of the incubator and the port resealed with tape. Heating/Stirring plates were set to maintain 40˚C solution temperature in the 1 L reservoirs (Section 3.8.1), which decreased the amount of condensation observed in the incubator while maintaining solution temperature. Experimental reservoir volumes were 900 mL in each reservoir with volumes at the same level in each reservoir to prevent pressure differentials in the system. Reservoir solutions

were stirred at approximately 700 rpm during the experiment.

3.8.4.1 iDDS Mineralization Experimental Details

iDDS mineralization experiments were carried out as detailed in Section 3.8.3.1 with the modifications outlined in Section 3.8.4. Band appearance was monitored every 30 minutes for the 2 hrs prior to expected mineral band formation by opening the incubator doors and moving the tray until gel observation was possible.

3.8.5 Instrumental Analysis and Sample Preparation

3.8.5.1 Powder X-ray Diffraction (pXRD) Sample Preparation

Mineral bands were sliced out of the gels and soaked in 2 mL of 0.15 M NH_4OH for 1 hr. Gels were then rinsed with copious amounts of 0.15 M NH_4OH over a Buchner funnel, frozen, and lyophilized for 36-48 hrs. Lyophilized samples were ground in liquid nitrogen using a marble mortar and pestle. The resulting powder was then analyzed via pXRD.

3.8.5.2 pXRD

Powder x-ray diffraction measurements were performed using a Scintag Theta-Theta Diffractometer with CuKα radiation at 45 kV and 40 mA. Each sample was scanned over a 2θ range of 2-50º with a step size of 0.02º and a count time of 0.3 seconds. Samples were placed on quartz zero background holders.

3.8.5.3 Hydrolysis of Gel Slices for Inductively Coupled Plasma – Atomic Emission Spectroscopy (ICP-AES) Analysis

Gels were hydrolyzed in 10 mL of 0.8 M HNO_3 (Fisher) at 70˚C overnight in a 15 mL centrifuge tube. Samples were further diluted in 0.8 M HNO_3 (3 mL of hydrolyzed solution in 10 mL 0.8 M HNO_3) for ICP-AES analysis.

3.8.5.4 ICP-AES Analysis

Samples were run through an ICP trace analyzer emission spectrometer (Model ICAP 61E trace analyzer, Thermo Electron, Waltham Ma). The concentration from each solution was reported in ppm for calcium and phosphate then converted to mM.

REFERENCES

(1) Yang, P. J.; Temenoff, J. S., Engineering Orthopedic Tissue Interfaces, *Tissue Engineering Part B-Reviews* **2009**, *15*, 127.

(2) Dorvee, J. R.; Boskey, A. L.; Estroff, L. A., Rediscovering Hydrogel-Based Double-Diffusion Systems for Studying Biomineralization, *CrystEngComm* **2012**, *14*, 5681.

(3) Fischbach, C.; Kong, H. J.; Hsiong, S. X.; Evangelista, M. B.; Yuen, W.; Mooney, D. J., Cancer Cell Angiogenic Capability Is Regulated by 3d Culture and Integrin Engagement, *P. Natl. Acad. Sci.* **2009**, *106*, 399.

(4) Boskey, A. L., Hydroxyapatite Formation in a Dynamic Collagen Gel System - Effects of Type-I Collagen, Lipids, and Proteoglycans, *J. Phys. Chem.* **1989**, *93*, 1628.

(5) Cheung, Y. K.; Azeloglu, E. U.; Shiovitz, D. A.; Costa, K. D.; Seliktar, D.; Sia, S. K., Microscale Control of Stiffness in a Cell-Adhesive Substrate Using Microfluidics-Based Lithography, *Angewandte Chemie-International Edition* **2009**, *48*, 7188.

(6) Pathi, S. P.; Kowalczewski, C.; Tadipatri, R.; Fischbach, C., A Novel 3-D Mineralized Tumor Model to Study Breast Cancer Bone Metastasis, *Plos One* **2010**, *5*.

(7) Kim, S. S.; Park, M. S.; Jeon, O.; Choi, C. Y.; Kim, B. S., Poly(Lactide-Co-Glycolide)/Hydroxyapatite Composite Scaffolds for Bone Tissue Engineering, *Biomaterials* **2006**, *27*, 1399.

(8) Rowley, J. A.; Madlambayan, G.; Mooney, D. J., Alginate Hydrogels as Synthetic Extracellular Matrix Materials, *Biomaterials* **1999**, *20*, 45.

(9) Ratner, B. D.; Bryant, S. J., Biomaterials: Where We Have Been and Where We Are Going, *Annu. Rev. Biomed. Eng.* **2004**, *6*, 41.

(10) Lee, K. Y.; Mooney, D. J., Hydrogels for Tissue Engineering, *Chem. Rev.* **2001**, *101*, 1869.

(11) Cukierman, E.; Pankov, R.; Stevens, D. R.; Yamada, K. M., Taking Cell-Matrix Adhesions to the Third Dimension, *Science* **2001**, *294*, 1708.

(12) Boyan, B. D.; Hummert, T. W.; Dean, D. D.; Schwartz, Z., Role of Material Surfaces in Regulating Bone and Cartilage Cell Response, *Biomaterials* **1996**, *17*, 137.

(13) Weiner, S.; Wagner, H. D., The Material Bone: Structure Mechanical Function Relations, *Annu. Rev. Mater. Sci.* **1998**, *28*, 271.

(14) Olszta, M. J.; Cheng, X. G.; Jee, S. S.; Kumar, R.; Kim, Y. Y.; Kaufman, M. J.; Douglas, E. P.; Gower, L. B., Bone Structure and Formation: A New Perspective, *Materials Science & Engineering R-Reports* **2007**, *58*, 77.

(15) Baht, G. S.; Hunter, G. K.; Goldberg, H. A., Bone Sialoprotein-Collagen Interaction Promotes Hydroxyapatite Nucleation, *Matrix Biol.* **2008**, *27*, 600.

(16) Iijima, M.; Moriwaki, Y.; Wen, H. B.; Fincham, A. G.; Moradian-Oldak, J., Elongated Growth of Octacalcium Phosphate Crystals in Recombinant Amelogenin Gels under Controlled Ionic Flow, *J. Dent. Res.* **2002**, *81*, 69.

(17) Boskey, A. L.; Maresca, M.; Ullrich, W.; Doty, S. B.; Butler, W. T.; Prince, C. W., Osteopontin-Hydroxyapatite Interactions in-Vitro - Inhibition of Hydroxyapatite Formation and Growth in a Gelatin-Gel, *Bone Miner.* **1993**, *22*, 147.

(18) Jiang, J.; Nicoll, S. B.; Lu, H. H., Co-Culture of Osteoblasts and Chondrocytes Modulates Cellular Differentiation in Vitro, *Biochem. Biophys. Res. Commun.* **2005**, *338*, 762.

(19) Sant, S.; Hancock, M. J.; Donnelly, J. P.; Iyer, D.; Khademhosseini, A., Biomimetic Gradient Hydrogels for Tissue Engineering, *Can. J. Chem. Eng.* **2010**, *88*, 899.

(20) Liu, Z. B.; Xiao, L. D.; Xu, B. J.; Zhang, Y.; Mak, A. F. T.; Li, Y.; Man, W. Y.; Yang, M., Covalently Immobilized Biomolecule Gradient on Hydrogel Surface Using a Gradient Generating Microfluidic Device for a Quantitative Mesenchymal Stem Cell Study, *Biomicrofluidics* **2012**, *6*.

(21) Chatterjee, K.; Lin-Gibson, S.; Wallace, W. E.; Parekh, S. H.; Lee, Y. J.; Cicerone, M. T.; Young, M. F.; Simon, C. G., The Effect of 3d Hydrogel Scaffold Modulus on Osteoblast Differentiation and Mineralization Revealed by Combinatorial Screening, *Biomaterials* **2010**, *31*, 5051.

(22) Pathi, S. P.; Lin, D. D. W.; Dorvee, J. R.; Estroff, L. A.; Fischbach, C., Hydroxyapatite Nanoparticle-Containing Scaffolds for the Study of Breast Cancer Bone Metastasis, *Biomaterials* **2011**, *32*, 5112.

(23) Boskey, A. L.; Roy, R., Cell Culture Systems for Studies of Bone and Tooth Mineralization, *Chem. Rev.* **2008**, *108*, 4716.

(24) Tortelli, F.; Cancedda, R., Three-Dimensional Cultures of Osteogenic and Chondrogenic Cells: A Tissue Engineering Approach to Mimic Bone and Cartilage in Vitro, *European Cells & Materials* **2009**, *17*, 1.

(25) Lin, D. D. W., Cornell University 2013.

(26) Balluffi, R. W.; Allen, S. M.; Carter, W. C. *Kinetics of Materials*; Wiley-Interscience, 2005.

(27) Hunter, G. K.; Nyburg, S. C.; Pritzker, K. P. H., Hydroxyapatite Formation in Collagen, Gelatin, and Agarose Gels, *Coll. Relat. Res.* **1986**, *6*, 229.

(28) Lide, D. R. *Crc Handbook of Chemistry and Physics, 90th Edition*; CRC Press, 2009.

(29) Brunot, C.; Ponsonnet, L.; Lagneau, C.; Farge, P.; Picart, C.; Grosgogeat, B., Cytotoxicity of Polyethyleneimine (Pei), Precursor Base Layer of Polyelectrolyte Multilayer Films, *Biomaterials* **2007**, *28*, 632.

(30) Dauginet, L.; Duwez, A. S.; Legras, R.; Demoustier-Champagne, S., Surface Modification of Polycarbonate and Poly(Ethylene Terephthalate) Films and Membranes by Polyelectrolyte Deposition, *Langmuir* **2001**, *17*, 3952.

APPENDIX 3

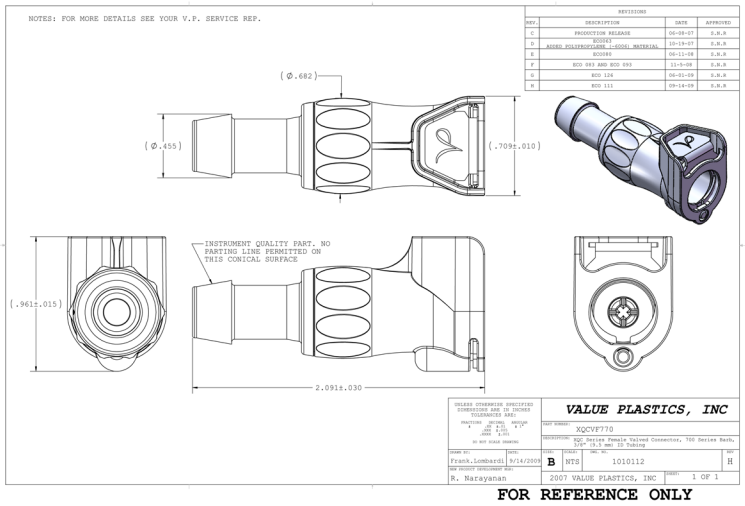

Figure A3.1: Specification sheet for the female quick disconnect used in the STR +DDS and mDDS/iDDS double diffusion systems.

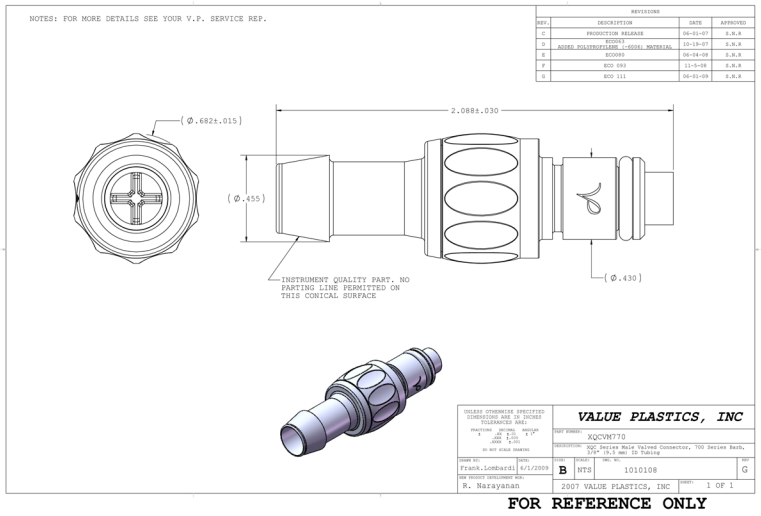

Figure A3.2: Specification sheet for the male quick disconnect used in the STR +DDS and mDDS/iDDS double diffusion systems.

SSP-M823

Polydimethyl Silicone Membrane

Product Description

SSP-M823 is our most permeable membrane. For many common gases, SSP-M823 is 30 times more permeable than non-silicone stable polymers. This polydimethylsiloxane (PDMS) membrane is supplied as a sheet or continuous roll with a thin release layer. SSP-M823 is available from .003"to .040" thick. We can assist customers to produce and manufacture custom thin film parts that meet your specific requirements. SSP-M823 can be combined with many other materials resulting in a composite appropriate for your specific application.

DATA	TYPICAL VALUES
Shore A	50
Tensile Elongation	1300 psi
Elongation (400 min)	570%
Specific Gravity	1.12 – 1.16
Tear B	200 ppi
Appearance	Translucent

Gas Permeability Rates*		APPLICATIONS	Membrane Thicknesses	
Oxygen	50	Gas Analysis	0.003"	0.004"
Carbon Dioxide	270	Gas Detection	0.006"	0.008"
Nitrogen	25	Gas Enrichment	0.010"	0.012"
Hydrogen	55	Gas Separation	0.014"	0.017"
		Cell Growth Support	0.024"	0.040"

*In barrers 10^{-9}(cc gas(RTP)cm)/(sec cm^2cmHg ΔP)

Custom thicknesses are available upon request. Minimum order may apply.

HANDLING & SAFETY

MSDS information is available on request.

For more information visit www.sspinc.com. To order call **(518) 885-8826/** or Fax **(518) 885-4682.**

Specialty Silicone Products, Inc.
Corporate Technology Park * 3 McCrea Hill Road * Ballston Spa, NY 12020

Specialty Silicone Products, Inc is an ISO 9001:2008 registered company.

SSPM823 Rev. 2 02/02/2010

Figure A3.3: Specification sheet from Specialty Silicone Products, Inc. for the 0.024" silicone membranes used for gas permeability.

Table A3.1: Parts list for mDDS/iDDS system assembly shown in Figure 3.6.

Part	Specs	Quantity	Source	Part Number (2012)
Polycarbonate sheet	3/8" thick	2 - 3" x 2.35" rectangles[a]	McMaster-Carr	8574K31
	1/4" thick	4 - 0.485" x 2.35" rectangles	McMaster-Carr	8574K19
	0.060" thick	2 - 3" x 2.35" rectangles	McMaster-Carr	8574K24
	1" thick	2 - 1" x 4"	McMaster-Carr	8574K791
Viton(R) O-rings	204	6	McMaster-Carr	9464K65
	005	8	McMaster-Carr	9464K105
Screws	4-40 flat head (socket), 316 Stainless	8	McMaster-Carr	90585A209
	4-40 Pan Head, 316 Stainless	16	McMaster-Carr	91735A117
Nuts	4-40 Hex Nut, 316 Stainless	8	McMaster-Carr	90257A005
Screw Driver	Philips head size 1	1		
Silicone Membranes	0.024" thick	2 - ~3" x 2.35" rectangles	Specialty Silicone Products, Inc.	Figure A3.3
	[a] Machined to 0.315" thickness			

Chapter 4:

CHARACTERIZATION OF SILK FIBROIN ADSORPTION ON FUNCTIONALIZED SURFACES AND INTERFACIAL CONTROL OF CALCIUM CARBONATE MINERALIZATION*

4.1 ABSTRACT

The assembly of organic matrices, and the formation of interfaces among the various matrix components, are essential to many biological processes, including biomineralization. This study investigates the organic-organic and organic-inorganic interfaces that form in an *in vitro* model of the organic matrix of nacre. To model the organic-organic interface, silk fibroin hydrogels were combined with self-assembled monolayers (SAMs) of alkanethiols on gold. This organic matrix was then used as a substrate for calcium carbonate mineralization. In the presence of silk fibroin, there was a loss of calcite orientation on the SAMs as well as a change in crystal nucleation density as compared to controls. To gain insight into the structure of the organic-organic interface, as well as to further understand the mineralization results, we carried out protein adsorption studies on SAMs. The adsorption of silk fibroin (β-sheet, hydrogel and random coil, aqueous) and BSA (α-helix, aqueous) was examined on four different surfaces (methyl-, carboxylate-, poly-ethylene glycol-terminated SAMs, and bare gold). Grazing angle Fourier transform infrared spectroscopy (GAFTIR) allowed us to non-invasively verify surface functionality, determine protein

*Amy Richter Blakeley, Ellen C. Keene, Vijay Ravichandran, Lara A. Estroff, in preparation

secondary structure on the surface, and determine relative amounts of surface adsorbed proteins by monitoring both amide I (1600-1700 cm^{-1}) and amide II (1500-1600 cm^{-1}) peak areas and positions. Random coil, aqueous silk fibroin adsorbed the most to all surfaces, while β-sheet silk fibroin hydrogel adsorbed the least. Across surfaces, the unfunctionalized, bare gold substrate adsorbed the most protein compared to the SAM surfaces. Regardless of the initial protein conformation, the proteins became more disordered upon surface adsorption. The adsorbed proteins mask the underlying SAM functionality, resulting in the loss of calcite orientation on these surfaces. Our results demonstrate the importance of characterizing, and ultimately controlling, organic-organic and organic-inorganic interfaces when modeling biomineralization.

4.2 INTRODUCTION

Nacre, or mother-of-pearl (the inner layer of some mollusk shells), is a composite biomineral composed of aragonite (calcium carbonate) tablets connected by a sheet-like organic matrix. It is extensively researched due to its appearance, bioactivity, mechanical properties, and polymorph selectivity.[1-4] The organic matrix associated with mollusk nacre is composed of three major components: β-chitin, a silk fibroin-like protein hydrogel, and acidic, water-soluble proteins.[1,2] *In vitro* experiments have demonstrated that the complete organic matrix assembly is necessary to control

polymorph (aragonite over calcite).[2,3] The organic-organic (e.g., silk fibroin with β-chitin) and the organic-inorganic interactions (e.g., β-chitin and silk fibroin with mineral) that result in oriented aragonite tablets in nacre, however, are still poorly understood. The role of such interfaces in biomineralization has implications for the synthesis of new materials based upon the interactions among functionalized surfaces, biomacromolecules, and mineral. Here, we present a synthetic system to probe such interactions and their implications for controlling mineral nucleation (e.g., density and crystallographic orientation) (Figure 4.1).

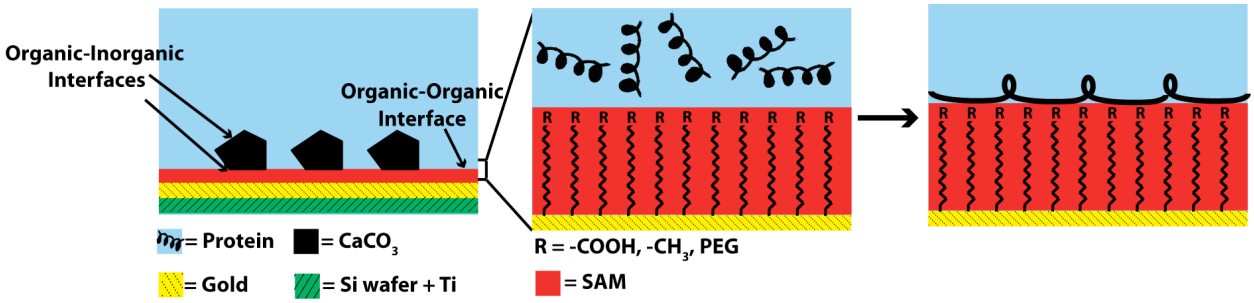

Figure 4.1: Experimental design schematic. The growth interface (mineral-protein) and the nucleating interface (mineral-SAM) are both referred to as the organic-inorganic interfaces. The interface between the SAM and the protein (Silk fibroin hydrogel or BSA) is referred to as the organic-organic interface. Solution or hydrogel protein (black helix within bulk protein) physisorbs on the SAM, possibly changing conformation upon adsorption.

Histochemical studies of decalcified nacre have shown that carboxylate and sulfate groups are localized on an organic substrate (interlamellar chitin sheets between nacre tablets) to form possible nucleation sites for calcium carbonate.[4,5] A

recent *in vitro* study has shown that a nacre specific peptide, n16N, specifically binds to β-chitin.[6] This interaction creates a new organic matrix interface (β-chitin + n16N) that selectively nucleates aragonite over calcite. In another study, Weiss et al. proposed that in the insoluble organic matrix of the bivalve *Mytilus galloprovincialis*, there is an "intimate link" between β-chitin and silk fibroin-like proteins.[7] The data demonstrated a significant change in the surface activity of the chitin-protein complex as compared to pure chitin. They also suggested that the chitin-silk fibroin complex is crucial for mollusk shell biomineralization, as the complex is present in both adult and larval development stages. While in both of these studies, the conformation and distribution of the peptides on the β-chitin substrate is unknown, the results suggest that the interface between the insoluble organic matrix (β-chitin) with the other organic matrix components is a complex molecular assembly worthy of further study.[6-8] In this chapter, we focus on the interaction of silk fibroin with functionalized surfaces and the effects adsorbed protein have on calcium carbonate mineralization (Figure 4.1).

Self-assembled monolayers (SAMs), of ω-functionalized alkanethiols on coinage metals (typically gold), have become a universal model surface to study the structures and properties of organic surfaces and their influence on protein adsorption,[9] as well as on crystal growth.[10,11] SAMs on gold are well-characterized and form stable organic layers on metal surfaces with various terminal functional groups.[12]

Extensive work by Aizenberg and others, have shown that surface chemistry and orientation of the terminal functional group determines the crystallographic orientation of calcite crystals nucleated on SAMs.[9,11,13-17] To further extend the SAM model to biomineralization, proteins, such as silk fibroin, can also be introduced into the SAM-mineralization assay.[18,19] The chemical composition of the surface and its properties (charge, hydrophobicity, etc.) may affect protein adsorption,[20-28] as well as the conformation of the adsorbed protein layer.[24,26,27,29-31] Therefore, the presence of protein may affect the ability of the surface to template the nucleation of calcium carbonate crystals.

To characterize the protein-SAM system, we chose Fourier transform infrared spectroscopy (FTIR) as a widely available, well-established tool for the characterization of protein secondary structure[32] (including both silk fibroin[33-35] and BSA[24,36,37]). Unlike x-ray photoelectron spectroscopy (XPS) or atomic force microscopy (AFM), grazing angle FTIR (GAFTIR) is a surface sensitive technique that can non-destructively look at monolayer functionalities on reflective surfaces (i.e., gold), such that after analysis, the surface can then be used for other experiments (i.e., crystal growth). While many techniques have been utilized to measure protein adsorption on SAMs (FTIR,[24,29,33,36-39] surface plasmon resonance (SPR),[21,23,25,40] quartz crystal microbalance (QCM),[24,41] ellipsometry,[20,21,42] contact angle,[21,39] AFM,[30,43] and XPS[20,23,42]), only FTIR is sensitive to protein secondary structure. Sample characterization by FTIR is both a qualitative and quantitative technique. It can verify

surface chemical functionalities (qualitative),[44-47] while based on peak positions it can determine protein secondary structure (qualitative),[32,33] as well as relative amounts of protein adsorbed based on peak areas (semi-quantitative).[48]

4.3 RESULTS AND DISCUSSION

4.3.1 Protein-SAM Characterization

We examined three different starting protein conformations (random coil and β-sheet silk fibroin; α-helix bovine serum albumin (BSA)[49]). The random coil silk was an aqueous solution, whereas the β-sheet silk formed a hydrogel.[50] Proteins were adsorbed onto SAMs (methyl, carboxylate, and ethylene glycol functionalities) and bare gold surfaces.[44-47,1] Before protein adsorption, the SAM functionalities were confirmed by GAFTIR (Figure 4.2). Each SAM was then incubated with protein, rinsed, and subsequently characterized by GAFTIR to quantify protein adsorption on the SAMs, as well as, any change in protein conformation due to surface adsorption.

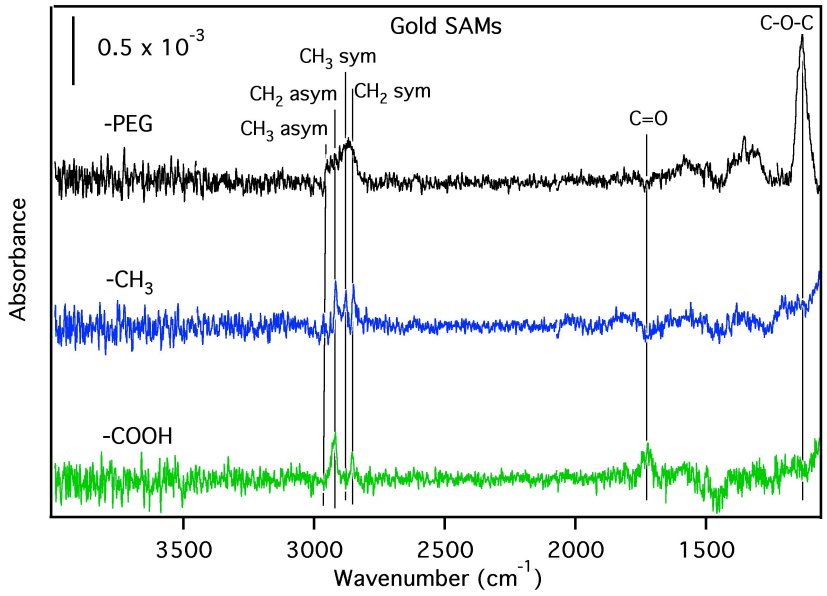

Figure 4.2: GAFTIR spectra of SAMs on gold surfaces (-PEG, -CH_3, -COOH) before protein adsorption. Expected peaks for each surface are observed and consistent with literature spectra.[44-47]

4.3.1.1 Bulk Protein Conformation

The secondary structure of all three protein preparations were confirmed prior to protein adsorption studies. The solutions and gels were analyzed by circular dichroism (CD) spectroscopy (Figure 4.3). Based upon their spectra, aqueous BSA is primarily α-helical, aqueous silk fibroin is random coil, and hydrogel silk fibroin are β-sheet. Further characterization of silk fibroin films, which were prepared by evaporation of an aqueous solution or a hydrogel, was performed using GAFTIR (Table 4.1 and Figure 4.4). Based on literature values for amide I IR peak positions (random coil: 1648-1644 cm^{-1}, β-sheet: 1632-1621 cm^{-1}, α-helical: 1655-1650 cm^{-1}),[33] it

was determined that upon film formation, the secondary structure of both aqueous and hydrogel silk fibroin remained random coil and β-sheet, respectively.

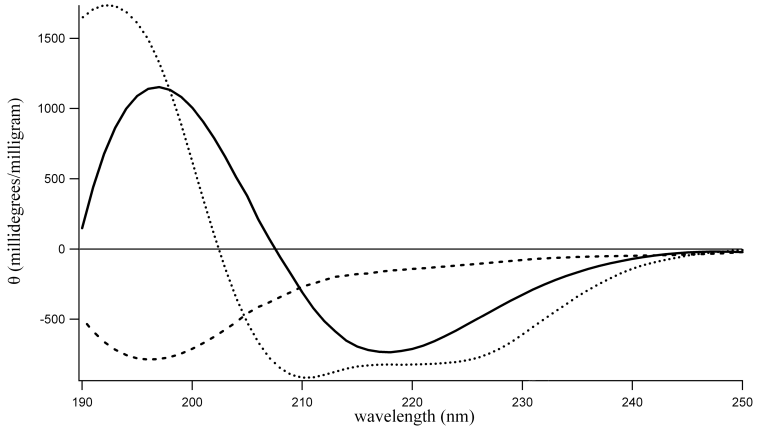

Figure 4.3: Representative CD spectra of aqueous silk fibroin (dashed line, random coil), gelled silk fibroin (solid line, β-sheet), and BSA (dotted line, α-helix) used for SAM incubation experiments. Spectra were taken of 20 mg/mL protein solutions.

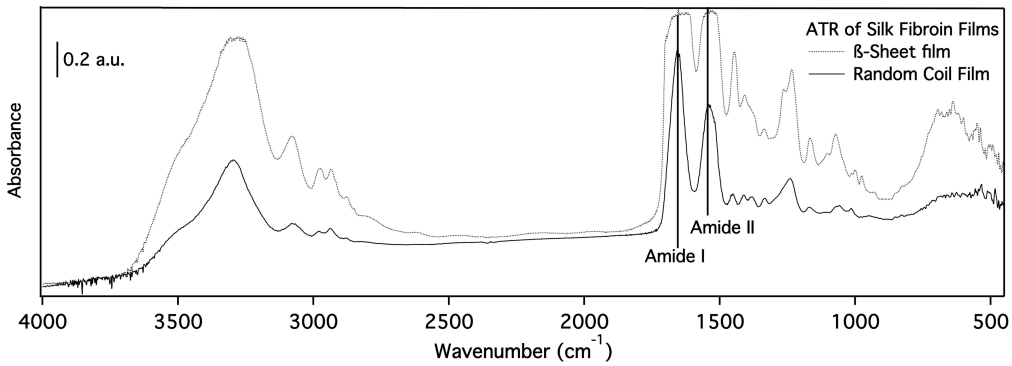

Figure 4.4: Diamond ATR spectra of silk fibroin films prepared via evaporation.

Table 4.1: Amide IR peak positions (cm^{-1}) and area ratios from GAFTIR spectra of adsorbed proteins on functionalized gold surfaces.

Random Coil (Silk)	Amide I position (cm^{-1})[c]	Amide I Area ratios[d]	Amide II position (cm^{-1})[c]	Amide II Area ratios[d,c]
Gold	1676 ± 0.7	1.00	1543 ± 2.3	1.00
-CH_3	1670 ± 1.3	0.85	1544 ± 1.1	0.96
-COOH	1673 ± 0.4	0.78	1544 ± 3.2	0.75
-PEG	-	-	-	-
Film[a]	1644		1520	
β-Sheet (Silk)				
Gold	1673 ± 2.1	0.17	1542 ± 1.7	0.32
-CH_3	1668 ± 2.3	0.21	1543 ± 0.8	0.38
-COOH	1667 ± 4.9	0.10	1542 ± 0.4	0.16
-PEG	-	-	-	-
Film[a]	1620		1520	
α-helix (BSA)				
Gold	1671 ± 0.6	0.41	1541 ± 1.7	0.47
-CH_3	1669 ± 1.0	0.20	1544 ± 0.6	0.33
-COOH	1670 ± 1.1	0.40	1543 ± 2.6	0.41
-PEG	-	-	-	-
Film[b]	1653		1538	

[a]Determined from diamond ATR spectra of silk fibroin films prepared by evaporation.
[b]Mielczarski et al., *J. Phys. Chem. B* **2008,** 112, 5228-5237.
[c]± standard deviation over a minimum of three measurements
[d]Peak areas normalized to random coil silk - gold surface for each peak.

4.3.1.2 Protein Coverage

GAFTIR showed that protein adsorbs on all SAMs except the PEG functionality, a known non-fouling surface (Figure 4.5).[42,51] The underlying SAM functionality remains after incubation with all three proteins (Figure 4.5). From our results, the protein arrangement (i.e., packing density or orientation) on the surface is not known but relative amounts of protein adsorbed can be compared (semi-quantitatively) based on peak areas.[48] Peak areas were analyzed to account for all protein conformations which may contribute to the Amide I band. Since the amount of protein adsorbed on each surface could be related to the chemistry at the protein-

SAM interface, peak areas for amide I and II were monitored for each protein conformation and surface chemistry. Amide peak areas are represented as ratios normalized to the random coil, aqueous silk fibroin on bare gold substrates for amide I and amide II (Table 4.1). All surfaces incubated with the random coil, aqueous silk fibroin had the most amount of adsorbed protein, while those surfaces incubated with the β-sheet, silk fibroin hydrogel had the least. The unfunctionalized, bare gold substrate adsorbed the most protein compared to the SAM surfaces. Among the SAMs, silk fibroin (both random coil and β-sheet) absorbed the most to methyl-terminated SAMs, while BSA absorbed the most to carboxylate-terminated SAMs.

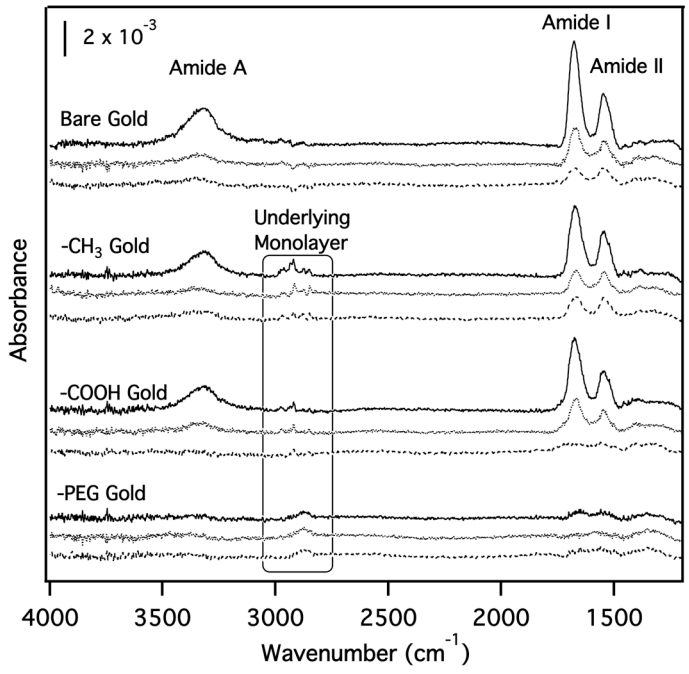

Figure 4.5: GAFTIR spectra of silk fibroin (random coil and β-sheet), and BSA (α-helix), represented by solid, dotted, and dashed lines respectively, adsorbed on functionalized gold surfaces.

4.3.1.3 Protein Conformation on SAMs

Protein-surface interactions play an important role in determining the conformation of the adsorbed proteins. The amide I region (1600-1700 cm^{-1}) is widely used for IR protein conformation studies due to differences in the amide bond orientations within a protein backbone structure that give rise to different vibrational frequencies.[32,36,37,52,53] As the angle and/or length of the amide hydrogen bond changes, the peak position changes. The amide II region (1500-1600 cm^{-1}) contains information about the in-plane N-H bend and C-N stretch of the amide bond but is less sensitive to protein conformation.[24,33,54] The amide III band (1200-1350 cm^{-1}) is also sensitive to conformation,[48] but was not analyzed in this work due to its weak intensity.

Characteristic amide I peak positions for random coil, β-sheet, and α-helix protein conformations are 1648-1644 cm^{-1}, 1632-1621 cm^{-1}, and 1655-1650 cm^{-1}, respectively.[33] Independent of the starting protein secondary structure and surface functionality, all amide I peak positions shift to higher wavenumber upon protein adsorption, while amide II peak position values are similar for all surfaces and protein conformations (Table 4.1). The adsorbed protein amide I peak positions were the highest wavenumber for random coil, aqueous silk fibroin and the lowest for β-sheet, hydrogel silk fibroin. Gold surfaces had the highest peak positions for all three initial protein conformations. Based on literature values, the amide I shift to higher

wavenumbers may suggest that the proteins are denaturing (irregular secondary structure, ~1671 cm^{-1})[55] or changing to a non-native, aggregated, intramolecular β-sheet or β-turn structure (1685-1663 cm^{-1})[24,32,52,56] upon adsorption to the substrate. Without additional information, it is difficult to distinguish between these two possibilities. Regardless of identifying a specific protein conformation, the shift in Amide I peak position demonstrates that the hydrogen-bonding pattern of the amide groups in the protein backbone have changed after physisorbing on the SAM.

The change in the protein amide hydrogen-bonding as indicated by the increase in frequency of the Amide I peak position could be due to the introduction of a functionalized substrate causing a change in protein stability and structure.[26,37,57-59] The degree of conformational change of a protein adsorbed on a surface will be dependent on the protein-surface interactions and the strength of the internal bonds (i.e., H-bonding) holding the protein in its particular conformation.[24] The β-sheet silk fibroin had the greatest amide I peak shift on all surfaces, with the largest change on gold (53 cm^{-1}), indicating the greatest change in conformation upon adsorption. Interestingly, the already disordered random coil silk fibroin had a greater shift in peak position than the α-helical BSA. The smaller peak shift suggests that BSA has a high surface affinity for each surface functionality based on its inherent secondary structure, whereas the already disordered random coil silk fibroin shows a larger amount of conformational change on adsorption. Our results suggest that adsorbed proteins

rearrange to reach a minimum surface energy regardless of starting conformation.[36,60,61]

Examination of literature reports regarding the peak positions of protein peptides provides further information on the potential protein conformation. Work by Tokmakoff[52] and co-workers utilizes 2D infrared spectroscopy and computational studies to probe the β-hairpin turn peak positions based on peptide structure. This work suggests that characteristic Amide I peptide peaks at 1670 cm^{-1} and 1640 cm^{-1} are indicative of the parallel and perpendicular band of an antiparallel β-sheet structure. The high population of amides at the kink of the β-turn gives rise to the vibration observed at 1670 cm^{-1}. However, the change from an α-helix structure in the BSA to an antiparallel β-sheet structure does not physically make sense due to the amount of conformation change required to go from a rigid helical structure to β-sheet. An increase in the number of disordered turns or kinks within the protein structure upon adsorption to the surfaces could be a more plausible explanation for the observed large shift to higher wavenumbers of the amide I peak.

Studies quantifying the peak positions of specific protein structures have been predominately carried out on dried films or in solution.[24,32,33,36,37,54-56] The peak position variations from literature in samples after physisorption could be due to the presence or lack of water in the protein structure. The presence of water could have an effect on the hydrogen bonding of the amide bond in the protein backbone, affecting the

Amide I and II peak positions. The IR data presented in this chapter was collected under vacuum, which likely results in the loss of water in the protein during analysis. Recent work by Takmakoff examined the affect that hydrogen bonds from other amide moieties and water have on the position of the proline amide I vibration in the GVGXPGVG (X = Gly, Ala, Val) peptide.[53] While this work predominately quantified the structural effect X has on the peptide structure, an interesting trend also became evident as a result of amide and water based hydrogen bonding. The greater number of hydrogen bonds with the proline structure resulted in a decrease in wavenumber of the Amide I peak position of the proline. The type of hydrogen bonding also affected the type of β-turns present in the peptide structure. Dehydration of the adsorbed protein as well as fewer amide-based hydrogen bonding contributes to the increase in amide I peak position observed in this work, which is indicative of a compact disordered protein state. A similar type of structural change may be occuring upon adsorption to the SAM functionalized surfaces, followed by dehydration.

Deconvolution of the Amide I and II peaks via second derivative analysis was attempted to gain further insight into protein conformation after adsorption on the surface.[24,62,63] We hoped to see what individual peaks make up the original data via peak fitting or second derivative analysis. The peak fitting of possible shoulders and components of the Amide I and II peaks was not possible due to the noise in the data (i.e., shoulders vs. noise were not distinguishable). In second derivative analysis, the

points where the second derivative of the spectra cross the x-axis (i.e., change sign) are the position of individual peaks that comprise the gaussian in the original spectra. Figure 4.6 shows a representative second derivative spectra of random-coil silk fibroin adsorbed on a methyl monolayer as well as that of β-chitin from a squid pen (see Figures 4.5 and 4.7 for original spectra). As can be seen by this data, the second derivative of protein adsorbed on gold monolayers proved to be too noisy to determine the inflection points for the peaks comprising Amide I and II. The chitin spectrum is shown to demonstrate what the second derivative data looks like with data of sufficient signal to noise. The inflection point data is necessary for completing the deconvolution of the original IR spectra.

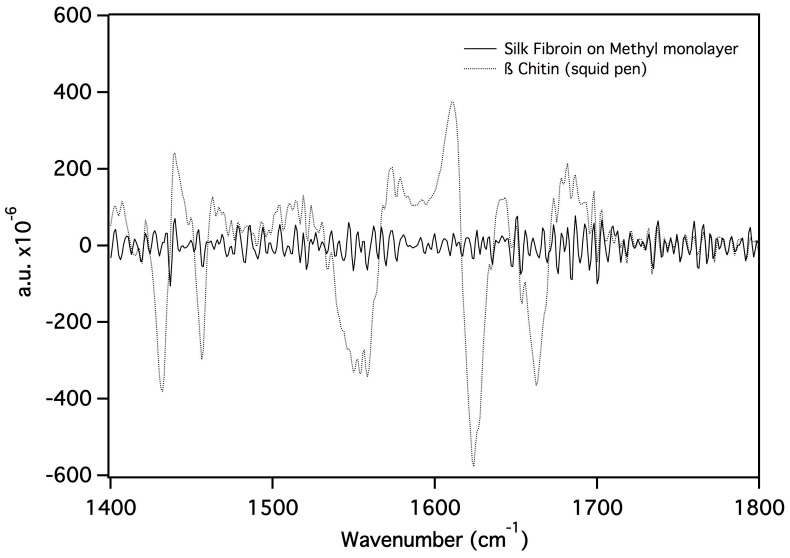

Figure 4.6: Representative second derivative of GAFTIR spectra of silk fibroin protein adsorbed on gold monolayers and β-chitin (squid pen). The points where the second derivative of the spectra cross the x-axis (i.e. change sign) are the position of individual peaks that comprise the gaussian in the original spectra.

Differences in protein adsorption, as a function of starting conformation, may be explained by looking at the inherent structure and stability of the protein. The random coil protein is a labile structure and can quickly change its structure to effectively lower its surface energy at the protein-SAM interface. In contrast, the β-sheet structure is a folded, stable structure whose conformation is more difficult to change for interaction with a surface.[64] Therefore, the amount of folded protein (β-sheet and α-helix), as compared to random coil, adsorbing onto the various SAM surfaces correlates to the stability of the protein. Several studies within the literature have made similar correlations: less stable proteins attach to surfaces quicker and stronger (i.e., irreversible protein adsorption) than stable, folded structures.[28,57,58] Another possible difference between the adsorption of the two silk fibroin protein conformations is that the random coil is in solution while the β-sheet forms a hydrogel. In viscoelastic hydrogels, diffusion of large proteins and/or protein aggregates is reduced as compared to solution,[65] possibly limiting the interaction of the proteins with the underlying substrate.

Based upon literature trends, the interaction of proteins with hydrophobic surfaces is expected to be greater than with hydrophilic surfaces.[64] Hydrophobic surfaces tend to denature adsorbed proteins by forcing proteins to expose internal, hydrophobic residues.[24,25] Our results, however, do not show a clear trend with surface hydropathy and protein denaturation. All samples have the greatest shift in

peak position (i.e., denaturation/rearrangement) on bare gold surfaces, as opposed to methyl terminated SAMs. In addition, proteins adsorbed to all surfaces shift peak positions to higher values as compared to bulk, film values. This result suggests that the presence of a surface alone, regardless of the hydropathy, can cause a protein to change its conformation.

Similar to our results, there are exceptions in literature to the generalization that proteins have a greater interaction with hydrophobic surfaces. For example, a recent study by Jeyachandran and co-workers found that BSA had 95% coverage on hydrophilic surfaces compared to 53% on hydrophobic polystyrene coated surfaces.[37] Other exceptions within the literature,[64,66,67] present similar results for α-chymotrypsin,[66] albumin,[67] fibrinogen,[64] and kininogen.[64] The examples presented, coupled with our results, indicate that each protein-surface pair needs to be studied individually rather than making broad assumptions regarding general protein interfacial behavior.

4.3.1.4 Protein Adsorption on β-chitin Substrates

Investigation of the organic-organic interface of the silk fibroin - β-chitin interface for nacre was attempted by adsorption of random coil silk fibroin on β-chitin substrates. The distinct amide peaks of the β-chitin (1654, 1630, and 1550 cm^{-1}) mask the Amide I and II of the adsorbed random coil silk fibroin (Figure 4.7).

Previous studies have unsuccessfully tried to quantify the amount of adsorbed protein on β-chitin.[68]

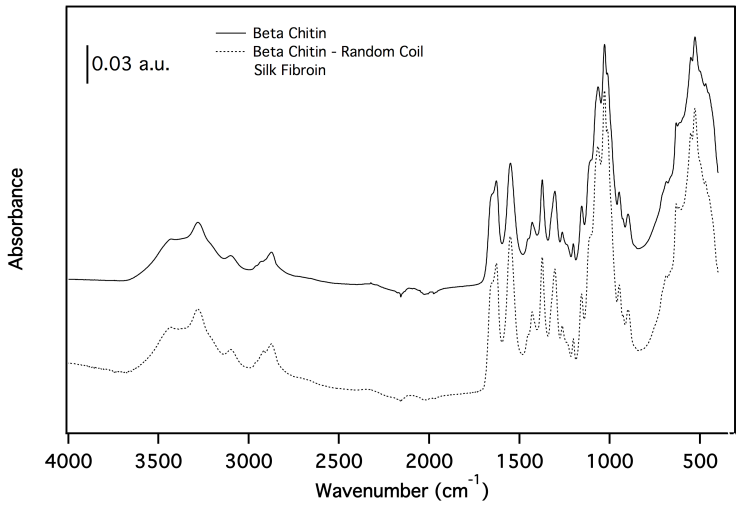

Figure 4.7: Diamond ATR spectra of β-chitin (squid pen) and β-chitin with adsorbed random coil silk fibroin.

4.3.2 Crystallization of Calcium Carbonate on SAMs with Silk Fibroin

To further our understanding of how protein affects the inorganic interface, calcium carbonate mineralization on the SAMs with and without adsorbed protein was investigated. We examined calcium carbonate growth on four surfaces (bare gold, methyl,[44] carboxylate,[45] and ethylene glycol[46,47] terminated SAMs) in the presence and absence of silk fibroin gels (Figure 4.8). On all surfaces, calcite crystals form. Calcite orientation and nucleation density on SAMs were determined. A more detailed analysis than that presented in this chapter can be found in Keene 2010.[69]

4.3.2.1 Crystal Orientation

In agreement with literature,[11,70,71] calcite crystals grown on carboxylate terminated SAMs show preferred (012) orientation, as confirmed by SEM and x-ray diffraction (Figure 4.8). Experiments using carboxylate SAMs with adsorbed protein (β-sheet silk fibroin, random coil silk fibroin, and α-helical BSA) were performed to further investigate the nature of the protein-SAM interface. Surfaces were first incubated with the respective protein preparation and then rinsed before immersion into the crystallization solution. Randomly oriented crystals grew on all surfaces with adsorbed protein. Interestingly, previous results have shown that carboxylate-terminated SAMs retain their orientation control in the presence of an agarose hydrogel.[72] The difference in calcite orientation among these systems suggests that proteins, such as silk fibroin and BSA, but not the polysaccharide agarose, bind to the surfaces and mask the carboxylate functionality, or otherwise disrupt the structure of the carboxylate SAM.

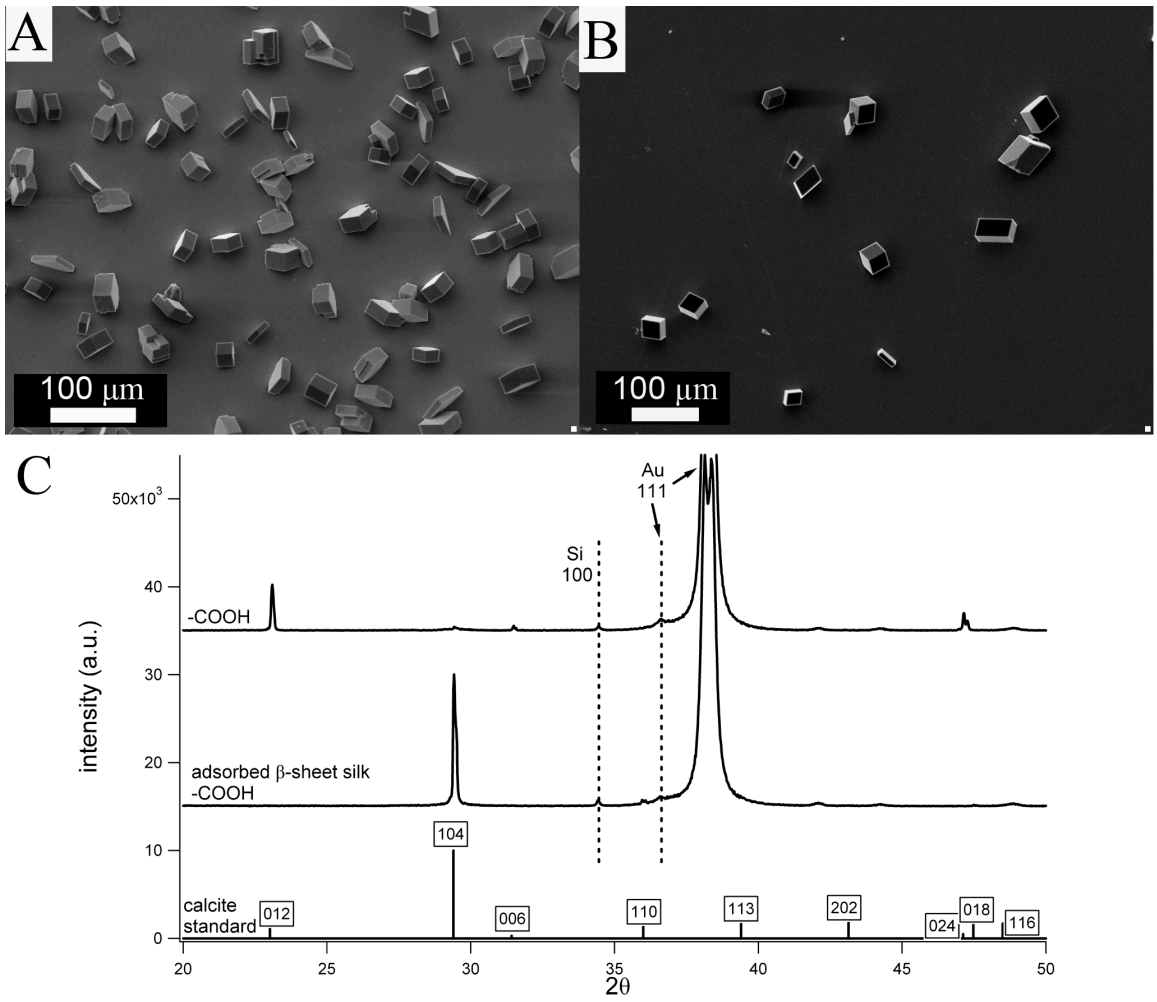

Figure 4.8: Calcite crystallization studies on carboxylate SAMs. SEM images of (A) control crystallization in the absence of protein, and (B) crystallization after incubation with β-sheet silk hydrogel. (C) XRD patterns of samples shown in (A) and (B).

4.3.2.2 Nucleation Density

The presence of silk fibroin during the crystallization assay also affects the nucleation density of calcite on SAMs. Methyl and carboxylate SAMs were compared for nucleation density (Table 4.2). In agreement with previous studies,[11] carboxylate SAMs without protein promote nucleation of calcite while methyl SAMs inhibit

nucleation. With the addition of silk fibroin to the crystallization assay, however, the nucleation density on methyl SAMs surpasses the density on carboxylate SAMs (Table 4.2). This result suggests that the organic-inorganic interface has changed with the addition of protein. The higher amount of silk fibroin adsorbed on the methyl SAMs (as compared to the carboxylate SAMs) may explain the observed increase in crystal nucleation density in the presence of silk fibroin gels. Silk fibroin adsorbed on a functionalized surface, may expose additional functional groups to promote crystal nucleation, as compared to control surfaces. Evidence of adsorbed silk fibroin on all surfaces, including carboxylate, can explain the loss of crystal orientation on the carboxylate SAM. Even though the β-sheet silk fibroin adsorbed the least on all surfaces, there is still enough protein on the surface to affect calcite orientation. The presence of silk fibroin, even in small amounts, may shield the carboxylate group or disrupt the packing of alkanethiols such that the carboxylate groups are no longer properly structured to orient the calcite crystals.[11] The inversion in nucleation density on the two different SAMs upon introduction of silk fibroin to the crystallization assay highlights the complexities in combining functionalized surfaces with protein solutions and/or gels for mineralization studies.

Table 4.2: Crystal nucleation density on methyl and carboxylate SAMs.

SAM Functionality	Silk fibroin Present?	Silk fibroin conformation	Nucleation density (crystals/mm^2)[a,c]	Area fraction (%)[a,b,c]
-CH_3	No	---	143 ± 72	3 ± 2
	Yes	Random coil	4291 ± 1568	23 ± 6
	Yes	β-sheet	138 ± 48	10 ± 1
-COOH	No	---	1923 ± 192	16 ± 7
	Yes	Random coil	2556 ± 2475	16 ± 5
	Yes	β-sheet	105 ± 21	6 ± 1

[a]± standard deviation over a minimum of six low magnification images across three samples

[b]Area fraction accounts for total area covered by crystals (i.e., crystal sizes) over the entire sample area.

[c]Representative low magnification SEM images are in Figure 4.3.

4.4 SUMMARY

While it is known that there is a periodic layering of β-chitin and silk-like proteins within nacre,[73] the relationship between the different macromolecules is poorly understood. Early studies of nacre by Weiner and Traub proposed that silk fibroin has a β -sheet conformation and is oriented with respect to the β-chitin fibrils.[74] More recent x-ray and electron diffraction studies, however, have not detected any β-sheet silk fibroin structure.[1,75] Our GAFTIR results indicate that regardless of initial protein conformation, a disordered silk-layer forms upon adsorption to several synthetic surfaces. Attempts to analyze silk fibroin conformation on β-chitin substrates, however, were unsuccessful due to the overlap of the amide peaks from the protein and the polysaccharide (Figure 4.7). On the SAMs, the

adsorbed protein creates a new organic-organic interface, which directly affects calcite crystal orientation and nucleation density on these surfaces. This study suggests that understanding individual interfaces *in vitro* can provide clues to macromolecular interactions that may contribute to the assembly of the framework responsible for control over mineralization *in vivo*.

4.5 MATERIALS AND METHODS

4.5.1 Self-Assembled Monolayer Formation

Gold coated silicon (100) wafers (50 Å titanium adhesion layer then 1000 Å gold) were purchased from Platypus Technologies. The wafer was cut into 1 cm^2 pieces and plasma cleaned immediately before SAM preparation. Methyl ($-CH_3$), carboxyl (-COOH), or poly-ethylene glycol (PEG) terminated SAMs were formed on gold substrates by exposing the surfaces to 10 mM solution of the thiol (1-hexadecanethiol, 16-mercaptohexadecanoic acid, or (1-mercapto-11-undecyl)tetra(ethylene glycol), Sigma) in absolute ethanol[76] for 24 hours, followed by washing with ethanol, then DI water.[11,72,77] After rinsing, slides were transferred to petri dishes and immediately used for adsorption GAFTIR and/or crystallization studies.

4.5.2 Silk Fibroin Purification

Bombyx mori cocoons were purified according to the procedure outline in Ref. [78]. Fresh aqueous silk fibroin solutions were either used immediately for random coil silk fibroin experiments or capped in glass test tubes (3 mL of solution) followed by incubation in a hot water bath at 60° C to induce β-sheet formation (resulting in silk fibroin gelation).[79]

Silk fibroin films were made by drying silk solutions at room temperature. Films were either characterized after drying (for random coil conformation) or treated

the films with methanol to induce β-sheet transformation. Dried films were also made from silk fibroin gels, but were more brittle and harder to handle. Any mention of 'silk', 'silk solutions', and 'silk hydrogels' refer to the purified silk fibroin protein.

4.5.3 Circular Dichroism (CD)

The secondary structures of silk fibroin and BSA were verified via CD spectroscopy before use for adsorption studies. Spectra were recorded using a Model 400 Aviv spectrometer with a Peltier thermocouple temperature control. The spectra were recorded from 190 to 250 nm with a 1 nm step. A quartz cuvette (Helma Worldwide) with a 1 cm path length was used for measurements, and was capped to prevent evaporation. All samples were diluted with DI water to a concentration of ~20 mg/mL for the best signal to noise ratio. Background spectra (DI water) were recorded and subtracted from each sample. Background subtracting and spectra smoothing were all done within the CD software. All theta values are reported as millidegree per milligram (mdeg/mg).

4.5.4 Protein Adsorption

SAM coated or plasma cleaned bare gold slides were incubated in 5 mg/mL protein solutions (silk fibroin or bovine serum albumin (BSA, Fisherbrand, used without any further purification)) for 24 hours. To avoid variability among protein batches, four SAMs (one of each surface chemistry) were placed in a single petri dish and incubated with the same protein solution. After incubation, slides were removed,

rinsed with deionized water, dried under nitrogen, and immediately characterized with GAFTIR.

4.5.5 Grazing Angle Fourier Transform Infrared Spectroscopy (GAFTIR)

Infrared analysis of SAM functionality and surface adsorbed protein was conducted using a Bruker Vertex 80v FTIR with a VeeMax II grazing angle accessory and a MCTA detector. The grazing angle was set to 75º and p-polarized light was used to obtain the best spectra for gold coated monolayers. A freshly plasma cleaned bare gold surface was used as the background for all spectra. A Pike Technologies Miracle Diamond ATR was used for control silk film characterization.

The FTIR was vacuum purged for 15 minutes prior to spectra acquisition to ensure elimination of CO_2 and water vapor. Spectra were recorded at 2 cm^{-1} resolution and 256 scans. Spectra were analyzed (peak fitting, position, area, and baseline subtracted) using Igor analysis software. Second derivative analysis of the GAFTIR spectra was performed as outlined in Elagovean et. al. using Igor analysis software.[75]

4.5.6 Calcium Carbonate Crystallization

Crystal growth experiments were carried out according to the procedure outlined in Keene 2010. Crystal nucleation densities were tabulated with the use of ImageJ, a freeware program available at http://rsbweb.nih.gov/ij. Grayscale images were thresholded and analyzed. The following data was recorded for each image: number of crystals, crystal areas, and area fraction (crystal coverage per sample area).

4.5.7 Powder X-Ray Diffraction (pXRD)

X-ray diffraction measurements were performed using a Scintag Theta-Theta Diffractometer with CuKα radiation at 45 kV and 40 mA. Each sample was scanned over a 2θ range of 20-50º with a step size of 0.02º and a count time of 0.3 seconds.

REFERENCES

(1) Levi-Kalisman, Y.; Falini, G.; Addadi, L.; Weiner, S., Structure of the Nacreous Organic Matrix of a Bivalve Mollusk Shell Examined in the Hydrated State Using Cryo-Tem, *J. Struct. Biol.* **2001**, *135*, 8.

(2) Falini, G.; Albeck, S.; Weiner, S.; Addadi, L., Control of Aragonite or Calcite Polymorphism by Mollusk Shell Macromolecules, *Science* **1996**, *271*, 67.

(3) Belcher, A. M.; Wu, X. H.; Christensen, R. J.; Hansma, P. K.; Stucky, G. D.; Morse, D. E., Control of Crystal Phase Switching and Orientation by Soluble Mollusc-Shell Proteins, *Nature* **1996**, *381*, 56.

(4) Addadi, L.; Moradian, J.; Shay, E.; Maroudas, N. G.; Weiner, S., A Chemical-Model for the Cooperation of Sulfates and Carboxylates in Calcite Crystal Nucleation - Relevance to Biomineralization, *P. Natl. Acad. Sci.* **1987**, *84*, 2732.

(5) Nudelman, F.; Gotliv, B. A.; Addadi, L.; Weiner, S., Mollusk Shell Formation: Mapping the Distribution of Organic Matrix Components Underlying a Single Aragonitic Tablet in Nacre, *J. Struct. Biol.* **2006**, *153*, 176.

(6) Keene, E. C.; Evans, J. S.; Estroff, L. A., Matrix Interactions in Biomineralization: Aragonite Nucleation by an Intrinsically Disordered Nacre Polypeptide, N16n, Associated with a B-Chitin Substrate, *Cryst. Growth Des.* **2010**, *10*, 1383.

(7) Weiss, I. M.; Kaufmann, S.; Heiland, B.; Tanaka, M., Covalent Modification of Chitin with Silk-Derivatives Acts as an Amphiphilic Self-Organizing Template in Nacre Biomineralisation, *J. Struct. Biol.* **2009**, *167*, 68.

(8) Suzuki, M.; Saruwatari, K.; Kogure, T.; Yamamoto, Y.; Nishimura, T.; Kato, T.; Nagasawa, H., An Acidic Matrix Protein, Pif, Is a Key Macromolecule for Nacre Formation, *Science* **2009**, *325*, 1388.

(9) Aizenberg, J.; Black, A. J.; Whitesides, G. M., Control of Crystal Nucleation by Patterned Self-Assembled Monolayers, *Nature* **1999**, *398*, 495.

(10) Mrksich, M.; Whitesides, G. M., Using Self-Assembled Monolayers to Understand the Interactions of Man-Made Surfaces with Proteins and Cells, *Annu. Rev. Biophys. Biomol. Struct.* **1996**, *25*, 55.

(11) Aizenberg, J.; Black, A. J.; Whitesides, G. H., Oriented Growth of Calcite Controlled by Self-Assembled Monolayers of Functionalized Alkanethiols Supported on Gold and Silver, *J. Am. Chem. Soc.* **1999**, *121*, 4500.

(12) Love, J. C.; Estroff, L. A.; Kriebel, J. K.; Nuzzo, R. G.; Whitesides, G. M., Self-Assembled Monolayers of Thiolates on Metals as a Form of Nanotechnology, *Chem. Rev.* **2005**, *105*, 1103.

(13) Travaille, A. M.; Kaptijn, L.; Verwer, P.; Hulsken, B.; Elemans, J.; Nolte, R. J. M.; van Kempen, H., Highly Oriented Self-Assembled Monolayers as Templates for Epitaxial Calcite Growth, *J. Am. Chem. Soc.* **2003**, *125*, 11571.

(14) Aizenberg, J., Crystallization in Patterns: A Bio-Inspired Approach, *Adv. Mater.* **2004**, *16*, 1295.

(15) Travaille, A. M.; Steijven, E. G. A.; Meekes, H.; van Kempen, H., Thermodynamics of Epitaxial Calcite Nucleation on Self-Assembled Monolayers, *J. Phys. Chem. B* **2005**, *109*, 5618.

(16) Lee, J. R. I.; Han, T. Y. J.; Willey, T. M.; Wang, D.; Meulenberg, R. W.; Nilsson, J.; Dove, P. M.; Terminello, L. J.; van Buuren, T.; De Yoreo, J. J., Structural Development of Mercaptophenol Self-Assembled Monolayers and the Overlying Mineral Phase During Templated $Caco_3$ Crystallization from a Transient Amorphous Film, *J. Am. Chem. Soc.* **2007**, *129*, 10370.

(17) Kuther, J.; Seshadri, R.; Nelles, G.; Butt, H. J.; Knoll, W.; Tremel, W., Rough Surfaces by Design: Gold Colloids Tethered to Gold Surfaces as Substrates for Caco3 Crystallization, *Adv. Mater.* **1998**, *10*, 401.

(18) Cao, C.; An, X., Biomineralization of Caco3 through the Cooperative Interactions between Multiple Additives and Self-Assembled Monolayers, *J. Phys. Chem. C* **2008**, *112*, 6526.

(19) Cao, C.; An, X., Coeffect of Silk Fibroin and Self-Assembly Monolayers on the Biomineralization of Calcium Carbonate, *J. Phys. Chem. C* **2008**, *112*, 15844.

(20) Prime, K. L.; Whitesides, G. M., Self-Assembled Organic Monolayers - Model Systems for Studying Adsorption of Proteins at Surfaces, *Science* **1991**, *252*, 1164.

(21) Ostuni, E.; Grzybowski, B. A.; Mrksich, M.; Roberts, C. S.; Whitesides, G. M., Adsorption of Proteins to Hydrophobic Sites on Mixed Self-Assembled Monolayers, *Langmuir* **2003**, *19*, 1861.

(22) Arima, Y.; Iwata, H., Effect of Wettability and Surface Functional Groups on Protein Adsorption and Cell Adhesion Using Well-Defined Mixed Self-Assembled Monolayers, *Biomaterials* **2007**, *28*, 3074.

(23) Chapman, R. G.; Ostuni, E.; Yan, L.; Whitesides, G. M., Preparation of Mixed Self-Assembled Monolayers (Sams) That Resist Adsorption of Proteins Using the Reaction of Amines with a Sam That Presents Interchain Carboxylic Anhydride Groups, *Langmuir* **2000**, *16*, 6927.

(24) Roach, P.; Farrar, D.; Perry, C. C., Interpretation of Protein Adsorption: Surface-Induced Conformational Changes, *J. Am. Chem. Soc.* **2005**, *127*, 8168.

(25) Sigal, G. B.; Mrksich, M.; Whitesides, G. M., Effect of Surface Wettability on the Adsorption of Proteins and Detergents, *J. Am. Chem. Soc.* **1998**, *120*, 3464.

(26) Servagent-Noinville, S.; Revault, M.; Quiquampoix, H.; Baron, M. H., Conformational Changes of Bovine Serum Albumin Induced by Adsorption on Different Clay Surfaces: Ftir Analysis, *J. Colloid Interf. Sci.* **2000**, *221*, 273.

(27) Ishiguro, R.; Yokoyama, Y.; Maeda, H.; Shimamura, A.; Kameyama, K.; Hiramatsu, K., Modes of Conformational Changes of Proteins Adsorbed on a Planar Hydrophobic Polymer Surface Reflecting Their Adsorption Behaviors, *J. Colloid Interf. Sci.* **2005**, *290*, 91.

(28) Roach, P.; Farrar, D.; Perry, C. C., Surface Tailoring for Controlled Protein Adsorption: Effect of Topography at the Nanometer Scale and Chemistry, *J. Am. Chem. Soc.* **2006**, *128*, 3939.

(29) Green, R. J.; Hopkinson, I.; Jones, R. A. L., Unfolding and Intermolecular Association in Globular Proteins Adsorbed at Interfaces, *Langmuir* **1999**, *15*, 5102.

(30) Taborelli, M.; Eng, L.; Descouts, P.; Ranieri, J. P.; Bellamkonda, R.; Aebischer, P., Bovine Serum-Albumin Conformation on Methyl and Amine Functionalized Surfaces Compared by Scanning Force Microscopy, *J. Biomed. Mater. Res.* **1995**, *29*, 707.

(31) Lenk, T. J.; Horbett, T. A.; Ratner, B. D.; Chittur, K. K., Infrared Spectroscopic Studies of Time-Dependent Changes in Fibrinogen Adsorbed to Polyurethanes, *Langmuir* **1991**, *7*, 1755.

(32) Byler, D. M.; Susi, H., Examination of the Secondary Structure of Proteins by Deconvolved Ftir Spectra, *Biopolymers* **1986**, *25*, 469.

(33) Miyazawa, T.; Blout, E. R., Infrared Spectra of Polypeptides in Various Conformations - Amide I and Ii Bands, *J. Am. Chem. Soc.* **1961**, *83*, 712.

(34) Muller, W. S.; Samuelson, L. A.; Fossey, S. A.; Kaplan, D. L., Formation and Characterization of Langmuir Silk Films, *Langmuir* **1993**, *9*, 1857.

(35) Ha, S. W.; Tonelli, A. E.; Hudson, S. M., Structural Studies of Bombyx Mori Silk Fibroin During Regeneration from Solutions and Wet Fiber Spinning, *Biomacromolecules* **2005**, *6*, 1722.

(36) Mielczarski, J. A.; Dong, J.; Mielczarski, E., Real Time Evaluation of Composition and Structure of Concanavalin a Adsorbed on a Polystyrene Surface, *J. Phys. Chem. B* **2008**, *112*, 5228.

(37) Jeyachandran, Y. L.; Mielczarski, E.; Rai, B.; Mielczarski, J. A., Quantitative and Qualitative Evaluation of Adsorption/Desorption of Bovine Serum Albumin on Hydrophilic and Hydrophobic Surfaces, *Langmuir* **2009**, *25*, 11614.

(38) Kim, H. S.; Hartgerink, J. D.; Ghadiri, M. R., Oriented Self-Assembly of Cyclic Peptide Nanotubes in Lipid Membranes, *J. Am. Chem. Soc.* **1998**, *120*, 4417.

(39) Sethuraman, A.; Vedantham, G.; Imoto, T.; Przybycien, T.; Belfort, G., Protein Unfolding at Interfaces: Slow Dynamics of Alpha-Helix to Beta-Sheet Transition, *Proteins* **2004**, *56*, 669.

(40) Furuya, M.; Haramura, M.; Tanaka, A., Reduction of Nonspecific Binding Proteins to Self-Assembled Monolayer on Gold Surface, *Biorg. Med. Chem.* **2006**, *14*, 537.

(41) Caruso, F.; Furlong, D. N.; Kingshott, P., Characterization of Ferritin Adsorption onto Gold, *J. Colloid Interf. Sci.* **1997**, *186*, 129.

(42) Prime, K. L.; Whitesides, G. M., Adsorption of Proteins onto Surfaces Containing End-Attached Oligo(Ethylene Oxide) - a Model System Using Self-Assembled Monolayers, *J. Am. Chem. Soc.* **1993**, *115*, 10714.

(43) Ta, T. C.; McDermott, M. T., Mapping Interfacial Chemistry Induced Variations in Protein Adsorption with Scanning Force Microscopy, *Anal. Chem.* **2000**, *72*, 2627.

(44) Laibinis, P. E.; Nuzzo, R. G.; Whitesides, G. M., Structure of Monolayers Formed by Coadsorption of 2 Normal-Alkanethiols of Different Chain Lengths on Gold and Its Relation to Wetting, *J. Phys. Chem.* **1992**, *96*, 5097.

(45) Nuzzo, R. G.; Dubois, L. H.; Allara, D. L., Fundamental-Studies of Microscopic Wetting on Organic-Surfaces .1. Formation and Structural Characterization of a Self-Consistent Series of Polyfunctional Organic Monolayers, *J. Am. Chem. Soc.* **1990**, *112*, 558.

(46) Harder, P.; Grunze, M.; Dahint, R.; Whitesides, G. M.; Laibinis, P. E., Molecular Conformation in Oligo(Ethylene Glycol)-Terminated Self-Assembled Monolayers on Gold and Silver Surfaces Determines Their Ability to Resist Protein Adsorption, *J. Phys. Chem. B* **1998**, *102*, 426.

(47) Herrwerth, S.; Eck, W.; Reinhardt, S.; Grunze, M., Factors That Determine the Protein Resistance of Oligoether Self-Assembled Monolayers - Internal Hydrophilicity, Terminal Hydrophilicity, and Lateral Packing Density, *J. Am. Chem. Soc.* **2003**, *125*, 9359.

(48) Surewicz, W. K.; Mantsch, H. H., New Insight into Protein Secondary Structure from Resolution-Enhanced Infrared-Spectra, *Biochim. Biophys. Acta* **1988**, *952*, 115.

(49) BSA is a commonly used control protein for many adsorption assays as it is the "standard" for non-specific protein adsorption on both hydrophobic and hydrophilic surfaces.

(50) At the concentrations used, β-sheet solutions are unstable and transform into gels. Random coil solutions are stable and do not form gels unless conformation changes to β-sheet .

(51) Zhang, M. Q.; Desai, T.; Ferrari, M., Proteins and Cells on Peg Immobilized Silicon Surfaces, *Biomaterials* **1998**, *19*, 953.

(52) Smith, A. W.; Tokmakoff, A., Amide I Two-Dimensional Infrared Spectroscopy of Beta-Hairpin Peptides, *J. Chem. Phys.* **2007**, *126*.

(53) Lessing, J.; Roy, S.; Reppert, M.; Baer, M.; Marx, D.; Jansen, T. L.; Knoester, J.; Tokmakoff, A., Identifying Residual Structure in Intrinsically Disordered Systems: A 2d Ir Spectroscopic Study of the Gvgxpgvg Peptide, *J. Am. Chem. Soc.* **2012**, *134*, 5032.

(54) Wu, Y. Q.; Murayama, K.; Czarnik-Matusewicz, B.; Ozaki, Y., Two-Dimensional Attenuated Total Reflection/Infrared Correlation Spectroscopy Studies on Concentration and Heat-Induced Structural Changes of Human Serum Albumin in Aqueous Solutions, *Appl. Spectrosc.* **2002**, *56*, 1186.

(55) Cerda-Costa, N.; De la Arada, I.; Aviles, F. X.; Arrondo, J. L. R.; Villegas, S., Influence of Aggregation Propensity and Stability on Amyloid Fibril

Formation as Studied by Fourier Transform Infrared Spectroscopy and Two-Dimensional Cos Analysis, *Biochemistry* **2009**, *48*, 10582.

(56) Cordeiro, Y.; Kraineva, J.; Suarez, M. C.; Tempesta, A. G.; Kelly, J. W.; Silva, J. L.; Winter, R.; Foguel, D., Fourier Transform Infrared Spectroscopy Provides a Fingerprint for the Tetramer and for the Aggregates of Transthyretin, *Biophys. J.* **2006**, *91*, 957.

(57) Karlsson, M.; Ekeroth, J.; Elwing, H.; Carlsson, U., Reduction of Irreversible Protein Adsorption on Solid Surfaces by Protein Engineering for Increased Stability, *J. Biol. Chem.* **2005**, *280*, 25558.

(58) McGuire, J.; Wahlgren, M. C.; Arnebrant, T., Structural Stability Effects on the Adsorption and Dodecyltrimethylammonium Bromide-Mediated Elutability of Bacteriophage-T4 Lysozyme at Silica Surfaces, *J. Colloid Interf. Sci.* **1995**, *170*, 182.

(59) Zeng, H. T.; Chittur, K. K.; Lacefield, W. R., Analysis of Bovine Serum Albumin Adsorption on Calcium Phosphate and Titanium Surfaces, *Biomaterials* **1999**, *20*, 377.

(60) Mbamala, E. C.; Ben-Shaul, A.; May, S., Domain Formation Induced by the Adsorption of Charged Proteins on Mixed Lipid Membranes, *Biophys. J.* **2005**, *88*, 1702.

(61) Halter, M.; Antia, M.; Vogel, V., Fibronectin Conformational Changes Induced by Adsorption to Liposomes, *J. Controlled Release* **2005**, *101*, 209.

(62) Elangovan, S.; Margolis, H. C.; Oppenheim, F. G.; Beniash, E., Conformational Changes in Salivary Proline-Rich Protein 1 Upon Adsorption to Calcium Phosphate Crystalsle, *Langmuir* **2007**, *23*, 11200.

(63) Ruegg, M.; Metzger, V.; Susi, H., Computer Analyses of Characteristic Infrared Bands of Globular Proteins, *Biopolymers* **1975**, *14*, 1465.

(64) *Proteins at Interfaces Ii: Fundamentals and Applications*; American Chemical Soceity: Washington, D.c., 1995.

(65) Boskey, A. L.; Maresca, M.; Ullrich, W.; Doty, S. B.; Butler, W. T.; Prince, C. W., Osteopontin-Hydroxyapatite Interactions in-Vitro - Inhibition of Hydroxyapatite Formation and Growth in a Gelatin-Gel, *Bone Miner.* **1993**, *22*, 147.

(66) You, C. C.; De, M.; Han, G.; Rotello, V. M., Tunable Inhibition and Denaturation of Alpha-Chymotrypsin with Amino Acid-Functionalized Gold Nanoparticles, *J. Am. Chem. Soc.* **2005**, *127*, 12873.

(67) Lin, Y. S.; Hlady, V.; Janatova, J., Adsorption of Complement Proteins on Surfaces with a Hydrophobicity Gradient, *Biomaterials* **1992**, *13*, 497.

(68) Keene, E. C, Ph.D. Thesis, Cornell University, 2010.

(69) Keene, E. C, Ph.D. Thesis, Cornell University, 2010.

(70) Masuda, Y.; Sugiyama, T.; Seo, W. S.; Koumoto, K., Deposition Mechanism of Anatase Tio2 on Self-Assembled Monolayers from an Aqueous Solution, *Chem. Mater.* **2003**, *15*, 2469.

(71) Singh, A.; Lee, I. S.; Myerson, A. S., Concomitant Crystallization of Roy on Patterned Substrates: Using a High Throughput Method to Improve the Chances of Crystallization of Different Polymorphs, *Cryst. Growth Des.* **2009**, *9*, 1182.

(72) Li, H. Y.; Estroff, L. A., Hydrogels Coupled with Self-Assembled Monolayers: An in Vitro Matrix to Study Calcite Biomineralization, *J. Am. Chem. Soc.* **2007**, *129*, 5480.

(73) Nudelman, F.; Shimoni, E.; Klein, E.; Rousseau, M.; Bourrat, X.; Lopez, E.; Addadi, L.; Weiner, S., Forming Nacreous Layer of the Shells of the Bivalves Atrina Rigida and Pinctada Margaritifera: An Environmental- and Cryo-Scanning Electron Microscopy Study, *J. Struct. Biol.* **2008**, *162*, 290.

(74) Weiner, S.; Traub, W., X-Ray-Diffraction Study of the Insoluble Organic Matrix of Mollusk Shells, *FEBS Lett.* **1980**, *111*, 311.

(75) Falini, G.; Weiner, S.; Addadi, L., Chitin-Silk Fibroin Interactions: Relevance to Calcium Carbonate Formation in Invertebrates, *Calcified Tissue International* **2003**, *72*, 548.

(76) The carboxylate SAM was formed using acidic ethanol (~pH 2) to increase ordering of the SAM surface by assuring that the carboxyl terminus is protonated during SAM formation, reducing multilayer formation.

(77) Larsen, N. B.; Biebuyck, H.; Delamarche, E.; Michel, B., Order in Microcontact Printed Self-Assembled Monolayers, *J. Am. Chem. Soc.* **1997**, *119*, 3017.

(78) Keene, E. C, Ph.D. Thesis, Cornell University, 2010.

(79) Kim, U. J.; Park, J. Y.; Li, C. M.; Jin, H. J.; Valluzzi, R.; Kaplan, D. L., Structure and Properties of Silk Hydrogels, *Biomacromolecules* **2004**, *5*, 786.

Chapter 5

CONCLUSIONS AND FUTURE DIRECTIONS

This thesis presented a series of studies aimed at developing *in vitro* models to help understand the role of interfaces in calcium phosphate mineralization. The studies presented explored covalently functionalized surfaces and their effect on solution-based mineralization, a double diffusion system for simultaneous study of cells, mineral, and organic matrix, and the effect of self-assembled monolayers on physisorbed proteins as well as mineralization. The results not only demonstrated that a complex set of tools and controlled experimental setups are necessary for studying the interfaces (cell-mineral-matrix) in biomineralization but also established new platforms for future studies.

In Chapter 2, functionalized porous silicon (pSi) surfaces provide a platform for studying the effect of chemistry on calcium phosphate mineralization in a suspended geometry. Three solution based mineralization environments (buffered, unbuffered-titration controlled, and unbuffered-static pH) were used to investigate the effects of six covalently bound chemistries on calcium phosphate mineralization. Porous silicon surfaces were successfully functionalized with methyl, carboxylate, and oxide chemistries, as well as attachment of additional molecules such as 2-aminoethyl dihydrogen phosphate (ADP) and 1-(3-aminopropyl)imidazole via N-hydroxysuccinimide/1-ethyl-3-

[3-dimethylaminopropyl]carbodiimide hydrochloride (NHS/EDC) coupling chemistry. NHS/EDC chemistry was also used to covalently-link the proteins osteopontin (OPN) and bovine serum albumin (BSA) to the pSi surface. The mineralization results demonstrate that surface chemistry plays an important role in directing calcium phosphate nucleation, morphology, and growth at the surface in a suspended geometry. Solution composition and length of experiment proved to be crucial to increasing experimental reproducibility as well as quantifying the effect of substrate chemistry on initial calcium phosphate surface nucleation and growth.

Covalent binding proteins to surfaces more closely mimicks the conformation constraints at the interfaces of biological systems. Porous silicon substrates in a controlled solution mineralization environment have the potential for examining the effects of protein conformations as well as protein segments that have been covalently bound to the surface. For example, different protein fragments of OPN have been shown to either inhibit or promote HA mineralization. These protein fragments could be attached to the pSi surface via coupling chemistry to study the affect of specific protein fragments and structures affect on mineralization. The pSi substrates could also be introduced as porous silicon disks (lift-off films of 200μm thick pSi) in which the porous structure allows for diffusion of ions while also introducing covalently bound interface chemistry. These types of studies would allow

researchers to understand more about the localized protein structural affects on mineralization at interfaces in biological systems.

Developing an *in vitro* model for mineralization requires development of tools to study not just individual processes within mineralization but also the combination of cell, mineral, and matrix interactions. Chapter 3 describes the development of an incubator-based, hydrogel double diffusion system (iDDS) for studying cell-mineral-matrix interactions in a 3-D environment. Successful hydroxyapatite mineralization was demonstrated at both room temperature and in the incubator using a custom-built polycarbonate double diffusion system with polydimethylsiloxane (PDMS) membranes for gas permeability, minimal polyethyleneimine (PEI) coating for gel adhesion, and cell culture compatible agarose. Ion diffusivities and ion product (i.e. supersaturation threshold) values for agarose when compared to those of gelatin under similar conditions demonstrate the need to calculate diffusivities for each specific gel-ion combination.

The iDDS system provides researchers with a new tool for combing cell, mineral, and matrix in a 3-D environment, opening new avenues of potential experiments for understanding the complexity of cell-mineral-matrix interactions. Further characterization of this custom-built system is necessary for achieving successful cell integration. Cell viability and activity (i.e., the ability of cells to thrive) will need be quantified to ensure that the cells can

thrive in the system for the length of a mineralization or gradient experiment, typically on the order of 3 to 14 days. Parameters such as a PEI window in the polycarbonate spacers, addition of ascorbic acid to the reservoirs, changing or refreshing of reservoir media, and length of PDMS exposed to the gel may need to be modified for adhesion and optimal cell viability. Characterization of the calcium and phosphate diffusivities at 37°C will be important for determining concentrations of ions and gradients of calcium and phosphate ions. More detailed information regarding the ion diffusivities in specific gels could allow researchers to understand more about how gradients of calcium and phosphate affect cell viability and behavior in biological systems. This double diffusion system could also be combined with the pSi disks to selectively introduce covalently bound proteins to quantify the effect on cells, mineralization, and the combined system. pSi disks can be created to allow for the introduction of covalently bound proteins to gel or solution based experiments while also maintaining transport of ions via porous structure of the silicon. This system provides a multitude of opportunities for further exploration of biological interfaces.

Determining the structure and amount of protein at mineralization interfaces is important for further understanding the complex processes of biomineralization. Towards this understanding, a series of grazing angle Fourier transform infrared spectroscopy (GAFTIR) and calcite ($CaCO_3$) mineralization

studies of physisorbed silk fibroin and BSA protein on gold self-assembled monolayers (SAMs) are presented in Chapter 4. Crystallization of calcium carbonate in the presence of silk fibroin varies from the solution controls on the SAMs. GAFTIR studies and analysis of the SAM-protein interface demonstrated that the protein conformation increases in disorder upon adsorption to the SAM based on Amide I and II peak positions. Amounts of adsorbed protein varied as a function of SAM chemistry. Peak positions for a physisorbed protein (BSA) indicated a structure farther from the native conformation than the covalently bound peak positions presented in Chapter 2. This work demonstrates the need for characterizing surface protein conformation as well as considering the effect of adsorbed vs. covalently bound proteins on conformation at interfaces. Infrared spectroscopy should be considered an initial analysis when working with interface protein chemistry to better quantify the protein structure and/or exposed chemistry affecting mineralization.

Combined, the studies presented in this thesis, demonstrate the continued need for development of experimental setups for elucidating the effects of interfaces in biomineralization. Control of the chemistry, solution composition, and mineralization environment are necessary. Covalently bound surface chemistry was shown to have a distinct affect on surface mineral nucleation and morphology at pre-solution nucleation time periods (Chapter 2).

Suspending the substrates provided distinctly different morphology and coverage than those reported in literature (Chapter 1, Section 1.4). The solutions used in this study also minimized counter ion interactions by using unbuffered solutions rather than simulated body fluid compositions.

A 'holy-grail' of calcium phosphate mineralization studies is to integrate cells into a 3-D controlled mineralization environment to study the cell-mineral-matrix interactions. Hydrogel-based double diffusion has potential to allow this simultaneous study. However, development of such a system requires understanding system design/construction, surface chemistry, and cell culture parameters (Chapter 3). Finally, proteins play an important role in guiding biomineralization. Understanding how proteins interact with surface chemistry as well as their structural changes and coverage, provides important clues towards biology's ability to exert control over biomineralization (Chap. 4).

Replicating the complex hierarchical structures observed in biology systems continues to challenge and intrigue researchers. The interplay between cells, mineral, and organic matrix directs the formation of composite structures with structural and chemical properties not found in synthetic systems. Continued research towards developing synthetic systems that elucidate the interactions in calcium phosphate systems will assist in development of *in vitro* models for calcium phosphate mineralization. *In vitro* models that more accurately model mineralization systems *in vivo* will assist in understanding

medical conditions such as osteoporosis and bone cancer as well as inform biomimetic materials development.